



POLITECNICO DI TORINO

Master's Degree in Aerospace Engineering

**Optimal Minimum-Propellant  
Trajectories for De-Orbiting  
Satellites into a Northern Lunar  
Polar Graveyard Region**

---

**Supervisor:**

Prof. Manuela Battipede

**Author:**

Alessandro Nitti

**Co-Supervisor:**

Dr. Luigi Mascolo

Academic Year 2023/24

## Abstract

Recent developments in the global space exploration have put a spotlight on the Moon, attracting the attention of major space agencies and private companies. NASA's ambitious plans for sustained human presence in cislunar space, e.g. the Lunar Orbital Platform-Gateway program, has raised interest in cislunar orbits, looking for some desirable properties such as relatively low transfer costs from Earth, low orbit maintenance costs, and favourable communications opportunities with both Earth and the lunar south pole. Among libration-point orbits, Halo Orbit families, and particularly Near-Rectilinear Halo Orbits, are of special interest due to their appealing characteristics from multiple perspectives. Perfectly periodic in the Circular Restricted Three-Body Problem model, NRHOs comprise a subset of the halo orbit families in the Earth-Moon system, characterized by close lunar passages and nearly-stable behaviour, thus requiring low-cost maintenance.

As the cislunar region is anticipated to become increasingly populated with spacecraft, including potential debris, it is important to highlight the necessity of strategic deorbiting planning and compliance with international laws governing space debris. This study focuses on optimizing lunar de-orbiting trajectories that use electric propulsion and depart from a NRHO, with a particular emphasis on minimizing propellant usage. The chosen reference orbit is the Gateway's southern L2 NRHO, with perilune and apolune radii of 3,300 km and 70,000 km and 9:2 synodic resonance with respect to the Moon's orbit around Earth. Its exact periodic motion is computed by single-shooting method via Differential Correction.

The main objective of the proposed research is to optimize low-thrust lunar de-orbiting trajectories by employing an indirect method based on the Optimal Control Theory that transforms the propellant minimization problem into a Two-Point Boundary Value Problem. The single-shooting method shows bang-bang control derived from the Pontryagin's Maximum Principle to optimize the trajectories,

ensuring that a specific region in the lunar north pole is targeted. The dynamic model considers 3-body gravitation (spacecraft subject to Earth and Moon gravity) within the Circular Restricted Three-Body Problem.

Results identify a specific orbital arc in the NRHO, post-apolune, which is deemed ideal for de-orbiting the satellite via a two-burn trajectory that enables direct disposal towards the lunar north pole, significantly reducing propellant consumption. This reduction in propellant required for de-orbiting allows the mission to allocate more fuel for earlier operational phases, effectively extending the mission's operational lifespan.

# Contents

<b>List of Figures</b>	<b>vii</b>
<b>List of Tables</b>	<b>ix</b>
<b>Acronyms</b>	<b>x</b>
<b>1 Introduction</b>	<b>1</b>
1.1 Motivation and objectives . . . . .	1
1.2 Thesis Overview . . . . .	5
<b>2 Dynamic models</b>	<b>7</b>
2.1 Two-Body Problem . . . . .	8
2.1.1 Reference Systems . . . . .	8
2.1.2 Equations of motion . . . . .	9
2.2 Three-Body Problem . . . . .	12
2.2.1 Synodic Reference System . . . . .	13
2.2.2 Nondimensionalization . . . . .	14
2.2.3 Equations of Motion . . . . .	15
2.2.4 Jacobi Integral . . . . .	18
2.2.5 Lagrangian Points . . . . .	20
2.2.6 Zero Velocity Surfaces . . . . .	21

2.3	N-body Problem . . . . .	23
<b>3</b>	<b>Periodic Orbits</b>	<b>26</b>
3.1	An analytical approximation . . . . .	27
3.2	Differential Correction . . . . .	29
3.3	Single-Shooting Method . . . . .	32
3.4	Lyapunov Orbits Computation . . . . .	36
3.5	Near-Rectilinear Halo Orbits Computation . . . . .	38
<b>4</b>	<b>Optimal Control Theory</b>	<b>43</b>
4.1	Numerical Methods for OCPs . . . . .	44
4.2	General Statement . . . . .	46
4.3	Implementing the Indirect Method . . . . .	47
4.3.1	Boundary Conditions for Optimality . . . . .	49
4.3.2	Euler-Lagrange and Control Variables Equations . . . . .	50
4.4	Multi-Point Optimal Control Problem . . . . .	51
4.5	Boundary Value Problem Implementation . . . . .	53
4.6	OCT in CR3BP Trajectory Optimization . . . . .	57
<b>5</b>	<b>Computation of Optimal De-Orbiting Trajectories</b>	<b>63</b>
5.1	Boundary Conditions . . . . .	65
5.1.1	Terminal Conditions . . . . .	65
5.1.2	Initial Conditions . . . . .	66
5.2	Results . . . . .	67
<b>6</b>	<b>Conclusion</b>	<b>77</b>
6.1	Future Research . . . . .	78
	<b>References</b>	<b>80</b>

<b>Appendix A</b>	<b>Jacobian Matrix in the CR3BP</b>	<b>86</b>
<b>Appendix B</b>	<b>Euler-Lagrange Equations</b>	<b>88</b>

# List of Figures

2.1	EME2000 $\{\hat{\mathbf{I}}, \hat{\mathbf{J}}, \hat{\mathbf{K}}\}$ , perifocal $\{\hat{\mathbf{p}}_{SC}, \hat{\mathbf{q}}_{SC}, \hat{\mathbf{w}}_{SC}\}$ and ZEN $\{\hat{\mathbf{u}}, \hat{\mathbf{v}}, \hat{\mathbf{w}}\}$ RFs . . . . .	8
2.2	Synodic reference system . . . . .	13
2.3	LPs in a generic synodic RS with $\mu = 0.1$ . . . . .	21
2.4	Earth-Moon ZVSs . . . . .	22
2.5	N-Body Problem representation in EME2000 RF . . . . .	24
3.1	Lyapunov Orbits family around EML2 . . . . .	37
3.2	Halo Orbits family around EML2 . . . . .	40
3.3	Southern 9:2 synodic resonant EML2 NRHO . . . . .	42
4.1	Thrust angles and components in the synodic RS . . . . .	61
5.1	Equal time distribution of starting point near apolune . . . . .	66
5.2	$\tau_f$ influence on $\mathcal{S}_{\mathcal{F}}$ . . . . .	68
5.3	Optimal de-orbiting trajectories . . . . .	69
5.4	Optimal de-orbiting trajectories - Injection points . . . . .	69
5.5	$t_f$ - Injection point position . . . . .	70
5.6	Propellant consumption and required $\Delta V$ - Injection point position . . . . .	71
5.7	Minimum-propellant optimal de-orbiting trajectory . . . . .	72
5.8	Evolution in time of synodic positions and velocities . . . . .	73

5.9	Evolution in time of switching function and mass . . . . .	74
5.10	Evolution in time of thrust angles . . . . .	75
5.11	Behavior of $\mathcal{S}_{\mathcal{F}}$ under different analysis conditions . . . . .	76

# List of Tables

2.1	EM LPs coordinates and Jacobi constants . . . . .	23
5.1	SC characteristic values . . . . .	64
5.2	Non-dimensionalizing values . . . . .	64
5.3	Initial state and costate for the minimum-propellant solution . . . . .	72

# Acronyms

2BP	Two-Body Problem
3BP	Three-Body Problem
BC	Boundary Condition
BVP	Boundary Value Problem
CoV	Calculus of Variations
CR3BP	Circular Restricted Three-Body Problem
DC	Differential Correction
DRO	Distant Retrograde Orbit
EM	Earth-Moon
EML1	Earth-Moon Lagrangian Point $L_1$
EML2	Earth-Moon Lagrangian Point $L_2$
EOL	End-of-Life
FTDC	Fixed-Time Differential Correction
GEO	Geostationary Orbit
HO	Halo Orbit
ICRF	International Celestial Reference Frame
IM	Indirect Method

LLO	Low Lunar Orbit
LO	Lyapunov Orbit
LOP-G	Lunar Orbital Platform-Gateway
LP	Lagrangian Point
MPBVP	Multi-Point Boundary Value Problem
NBP	N-Body Problem
NRHO	Near-Rectilinear Halo Orbit
OCP	Optimal Control Problem
OCT	Optimal Control Theory
ODE	Ordinary Differential Equation
PMP	Pontryagin's Maximum Principle
PmP	Pontryagin's minimum Principle
PO	Periodic Orbit
QPO	Quasi-Periodic Orbit
R3BP	Restricted Three-Body Problem
RF	Reference Frame
RS	Reference System
SC	Spacecraft
SE	Sun-Earth
STM	State Transition Matrix
TPBVP	Two-Point Boundary Value Problem
VTDC	Variable-Time Differential Correction
ZEN	Zenith-East-North
ZVS	Zero Velocity Surface

# Chapter 1

## Introduction

### 1.1 Motivation and objectives

In the evolving panorama of global space exploration, the Moon and *cis-lunar* space is increasingly capturing the interest of major space agencies and private companies worldwide. The cis-lunar domain, identified as that area of deep space under the gravitational influence of the Earth-Moon (EM) system, offers affordable near-term opportunities to help pave the way for future global human exploration acting as a crucial link between current missions and future deep space endeavors. The upcoming direction is to exploit Earth's orbital environment, the surface of the Moon, and cislunar space to foster the critical technologies, operational capabilities, and commercial space economy with a view to sustainable human presence on the Moon, Mars, and beyond.

In this complex environment, there are five special points, called Lagrangian Points, where the gravitational forces of two large bodies, in this case the Earth and the Moon, balance the centripetal force felt by a smaller object, e.g. a Spacecraft (SC). This equilibrium allows the smaller object to maintain a stable position relative to the two larger bodies. This mathematical problem, known as the "General Three-Body Problem", was considered by Italian-French mathematician Joseph-Louis Lagrange in his prize-winning paper [1].

In recent years, space mission design has focused on three-dimensional periodic and quasi-periodic orbits near the libration points in the EM three-body problem. This shift aligns with predictions made in the Vision for Space Exploration plan, outlined

in early 2004, which emphasized the importance of easily accessible cislunar space for future space exploration objectives [2]. Consequently, over the past two decades, there has been a growing interest in the concept of establishing a manned facility in a long-term relatively stable orbit in lunar vicinity. Missions may be established in EM libration orbits as a part of communication or navigation architecture, like in the ESA's Moonlight initiative [3], or to deploy and service spacecraft either in transit from the Moon or stationed at other Sun-Earth (SE) or EM libration regions. Moreover, these particular orbits may well become a prime staging area in the effort to colonize space near Earth or to colonize the Moon. [4].

The first mission to orbit the EM Lagrange points was the ARTEMIS (EML<sub>1</sub> and EML<sub>2</sub> Lissajous orbits, on either side of the Moon), part of the THEMIS extended mission of NASA with the aim of studying a type of magnetic phenomena called substorms in Earth's magnetosphere that tend to intensify auroras near Earth's poles [5, 6]. Then, the CNSA with its Chinese Lunar Exploration Program launched and will launch spacecraft towards libration point orbits like Chang'e 5-T1 and Queqiao relay satellite of Chang'e 4 mission respectively on a EML<sub>2</sub> Lissajous orbit and a EML<sub>2</sub> Halo orbit [7]. JAXA's EQUULEUS cubesat was launched in 2022 to reach a quasi-periodic Halo orbit around EML<sub>2</sub> using lunar flybys and solar perturbation in order to study the Earth's plasmasphere and demonstrate trajectory control techniques exploiting Sun-Earth-Moon dynamics [8].

Among other initiatives and space programs, the Artemis one is the most groundbreaking. The main objective of NASA's missions, in collaboration with ESA, JAXA, DLR, ASI, ISA and CSA, is to land the first woman and first person of color on the Moon, explore the lunar surface more than ever before, and lay the groundwork for sending astronauts to Mars [9]. The first one, Artemis 1, took place in late 2022 and was a successful unmanned lunar flight test for Space Launch System (SLS) rocket and Orion Spacecraft to prepare subsequent missions with astronauts, as planned for Artemis 2 and then for Artemis 3 that will mark humanity's first return to the lunar surface in more than 50 years. To achieve this goal, the crew will travel toward the Moon and Orion will perform a series of two engine burns to place the spacecraft in a EML<sub>2</sub> NRHO, selected to achieve long-term Artemis goals.

On future missions, NASA and its partners will assemble the Lunar Orbital Platform-Gateway (LOP-G) in a designated NRHO, a lunar space station much smaller and more focused platform than the International Space Station, to serve as

a hub for next Artemis missions. Gateway is a vital component of the NASA-led program to return to the Moon and pave the way for future Mars exploration. For long-term operations, the LOP-G acts as a staging area for both human and robotic lunar expeditions, extending the duration of stays on the Moon and potentially accommodating multiple surface visits within a single mission [10]. In the realm of numerous possibilities, the Gateway Program opted for a NRHO of the EML<sub>2</sub> southern family as its operational orbit with a 9:2 lunar synodic resonance. A CubeSat, launched in June 2022, is the first spacecraft to test such unique elliptical lunar orbit as part of the Cislunar Autonomous Positioning System Technology Operations and Navigation Experiment (CAPSTONE). Acting as a pathfinder for Gateway, CAPSTONE aims to reduce risk for future spacecraft by validating new navigation technologies and verifying the dynamics of this halo-shaped orbit [11].

In general, NRHOs combine the benefits of Low Lunar Orbit (LLO), which provides easy access to the Moon's surface, with those of a Distant Retrograde Orbit (DRO), known for its stability and thus fuel efficiency. In fact, these orbits exhibit neutral stability features, leading to minimal requirements for orbit maintenance and hence lower costs. Additionally, NRHOs enable spacecraft to reach the lunar surface in about half a day. Specifically, orbits that belong to the southern family offer exceptional communication coverage for areas near the Moon's south pole, area of particular interest for astronauts in order to test living conditions on extraterrestrial bodies. A key characteristic of the selected 9:2 lunar synodic resonance NRHO is its capability to sustain nearly perpetual line-of-sight with Earth. This ensures continuous communication between Earth and the Moon, a critical factor for lunar missions [12–14].

This ambitious program will bring together a growing presence of commercial, civil, and military stakeholders in the cis-lunar space, with the potential to navigate to different orbits around the Moon with both human and robotic exploration missions. This will entail a carefully orchestrated sequence of multiple launches in lunar orbit and spacecraft dockings with the forthcoming LOP-G. However, alongside the promise of these advancements lies a considerable challenge that must be addressed: the potential creation of significant amounts of space debris. The increase in spacecraft, satellite launches, and orbital activities raises concerns about the environmental impact on the space surrounding Earth and the Moon. Space debris, consisting of defunct satellites, discarded rocket stages and fragments from erosion and collisions, poses a serious threat to operational spacecraft, including crewed missions and

essential satellite infrastructure, limiting the ability to launch new spacecraft and eventually making entire orbits unusable. Another consequence is an increase of costs for space operations by requiring efforts to shield against or maneuver around it. The proliferation of space debris in lunar orbit could complicate navigation, increase the risk of collisions, and potentially hinder nations' ambitions, creating a situation comparable to the highly populated near-Earth region. This is why it necessitates the implementation of comprehensive Cis-lunar Space Traffic Management (CSTM) strategies, debris monitoring systems, and the development of debris mitigation and removal technologies to achieve Cis-lunar Space Situational Awareness (CSSA) and Cis-lunar Domain Awareness (CDA) allowing for the sustainable long term usability of the region [15].

To comply with current and future regulations and prevent the contamination of cislunar space, upcoming missions must minimize their debris production and carefully orchestrate the disposal of involved spacecraft. Given the intricate dynamic environment, the challenge of End-of-Life (EOL) disposal becomes notable for cislunar missions. Drawing from existing research [16, 17] and the historical record of previous missions, a cislunar spacecraft at EOL has three primary disposal strategies: executing an Earth atmospheric re-entry [18], moving to a stable graveyard orbit (cislunar or heliocentric) or de-orbiting onto the lunar surface [19]. Each presents specific constraints, advantages and drawbacks. Earth re-entry is a well-established practice in Space Debris Mitigation (SDM) for Earth-orbiting missions but is less common for lunar mission disposal due to the high transfer costs back to Earth and operational complexity. More cost-effective alternatives leverage the dynamics of the Sun-Earth-Moon system, harnessing the concept of graveyard orbit (often used for satellites on GEOs) but with many factors to deal with, given the complex dynamics. On the other hand, several missions have opted for lunar impact as a method of disposal [20, 21]. In this case impacts must be strategically managed to minimize risk to human assets and historical landmarks on the Moon taking into account the possibility of targeting a specific location used as graveyard in which the remnants of spacecraft intentionally deorbited on the surface could provide a rich source of raw materials more accessible and practical for future utilization.

The core of this thesis is the optimization of electric propulsion de-orbiting trajectories with a view towards utilizing lunar impact in a northern polar graveyard region as a disposal strategy, with a particular emphasis on minimizing propellant usage. This strategy is evaluated not just for its potential to mitigate space debris, but

also for its prospective contribution to the lunar economy by recycling the materials from the impacted spacecraft. The orbit chosen as the departure orbit is the LOP-G's Southern EML<sub>2</sub> NRHO, anticipated to be the primary destination for spacecraft in the coming years and potentially the main source of artificial debris in cislunar space. Within the Circular Restricted Three-Body Problem (CR3BP), the selected orbit presents a perfectly periodic motion that will be computed in Chapter 3.

From the perspective of propellant consumption, optimizing the trajectory for EOL operations implies minimizing the required propellant for de-orbiting, thus reducing costs and extending the operational lifespan of the satellite considering that satellites are launched with a finite amount of propellant intended for station keeping, orbit adjustments, and eventually, de-orbit maneuvers.

As will be described in Chapter 4, there are two main categories of numerical methods to solve such infinite-dimension time-continuous problem: Direct Methods and Indirect Methods. Both show advantages and drawbacks in terms of computational cost, implementation complexity, accuracy and sensitivity to the initial guess. For the purpose of this thesis, an indirect method is preferred due to the method's ability to deliver precise and potentially optimal solutions efficiently. Despite the presence of convergence challenges, the strategic value of indirect methods lies in their capacity to provide detailed insights into the problem's formulation and guide iterative enhancements towards the optimal solution.

Therefore the optimization is carried out with an indirect method based on the Optimal Control Theory (OCT), which transforms the propellant minimization problem into a Two-Point Boundary Value Problem (TPBVP). Pontryagin's Maximum Principle (PMP) allows the definition of a bang-bang control to optimize the trajectories starting from various points on the NRHO, ensuring that a specific region at the lunar north pole is targeted maximizing the final mass and, equivalently, minimizing the propellant consumption.

## 1.2 Thesis Overview

In Chapter 2, following a brief overview of the basic principles of orbital mechanics and Two-Body Problem, the discussion shifts to spacecraft motion influenced by Earth and Moon, dealing with the Three-Body Problem (3BP) and its simplification

in the Circular Restricted Three-Body Problem (CR3BP), actually employed as dynamic model in this thesis. The equations of motion for CR3BP are derived, from which the concepts of Lagrangian Points and Zero-Velocity Surfaces are explored.

Chapter 3 deals with Periodic Orbits (POs) construction, introducing the single shooting and differential correction strategies, used for identify and compute exact periodic motions across specific families of orbits in the CR3BP framework.

Chapter 4 introduces the Optimal Control Theory (OCT) and the necessary concepts for transforming a dynamic problem into an Optimal Control Problem (OCP), focusing on an indirect approach. It transforms a general optimization problem into a Two-Point Boundary Value Problem (TPBVP) outlining key optimization results and effectively applying OCT to spacecraft trajectory optimization domain, the core focus of this thesis.

Chapter 5 analyzes the solutions for optimal de-orbiting trajectories into a northern lunar polar graveyard region, obtained varying the injection point on the NRHO. Boundary conditions, both initial and terminal, are presented to fully define the problem. Results are illustrated and analyzed in order to identify the optimal minimum-propellant solution.

Finally, Chapter 6 summarizes the findings, highlighting the main results and suggesting possible research directions.

# Chapter 2

## Dynamic models

Chapter 2 presents the dynamic model implemented in this thesis, following a brief overview of the basic principles of orbital mechanics and related concepts. The goal is to establish a comprehensive understanding of the mathematical and physical frameworks that underpin the study of trajectory optimization. After a quick look on the classic but timeless Two-Body Problem (2BP), the discussion extends to the transition to the Three-Body Problem (3BP) and its simplification in the Circular Restricted Three-Body Problem (CR3BP), employed as dynamic model for the indirect optimization process. Key concepts such as the Jacobi Integral, Lagrangian Points (LPs) and Zero-Velocity Surface (ZVS) are introduced, which are essential for understanding the dynamics within this framework.

The notations adopted henceforth will follow that of Mascolo's PhD dissertation [22], used as guiding reference of this work. Written in list form, they are as follows:

- column vectors are written in lowercase bold fonts ( $\mathbf{x}$ ), except for known quantities (such as velocity  $\mathbf{V}$ );
- unit vectors are presented in lowercase bold fonts with a hat ( $\hat{\mathbf{x}}$ );
- matrices are denoted by bold uppercase letters ( $\mathbf{X}$ );
- quantities that are time derivatives are marked with one or more dots, applicable to both scalars and vectors ( $\dot{x}$ ,  $\dot{\mathbf{x}}$ );
- Greek letters, different fonts or tilde superscripts indicate quantities that have undergone some mathematical manipulations (e.g. non-dimensionalization).

## 2.1 Two-Body Problem

Before introducing the dynamic model adopted in this thesis, it is worthwhile to provide a recap of the fundamental principles of orbital mechanics, including an overview of orbital parameters and their significance in the so-called Two-Body Problem (2BP). Further in-depth analysis can be found to well-known textbooks on orbital mechanics [23–25] and are beyond the scope of this work.

### 2.1.1 Reference Systems

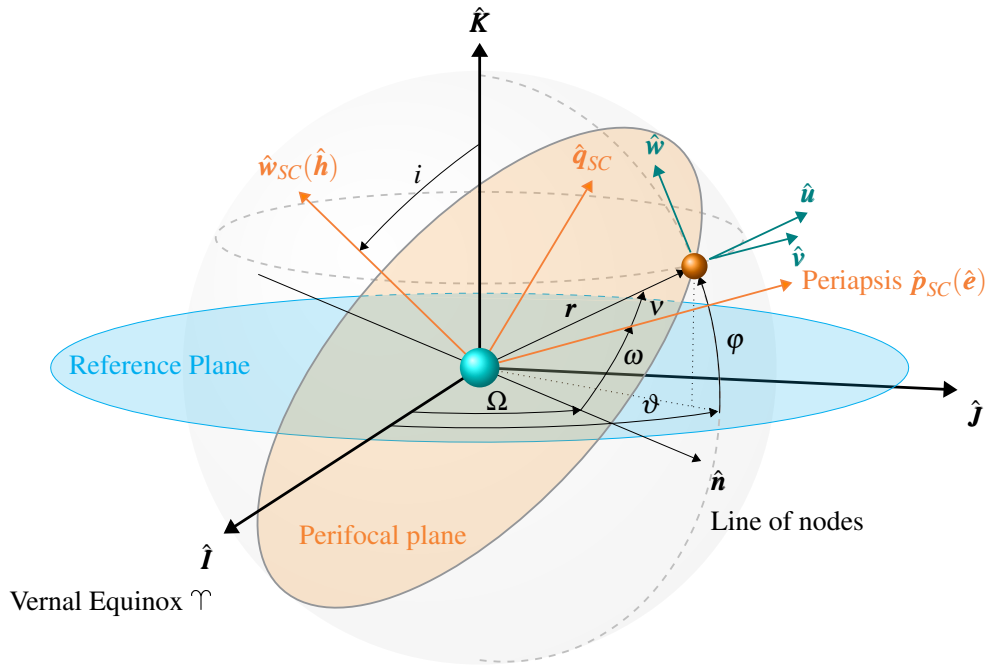


Fig. 2.1 EME2000  $\{\hat{\mathbf{I}}, \hat{\mathbf{J}}, \hat{\mathbf{K}}\}$ , perifocal  $\{\hat{\mathbf{p}}_{SC}, \hat{\mathbf{q}}_{SC}, \hat{\mathbf{w}}_{SC}\}$  and ZEN  $\{\hat{\mathbf{u}}, \hat{\mathbf{v}}, \hat{\mathbf{w}}\}$  RFs

A Reference Frame (RF) is specified by an ordered set of three mutually orthogonal, possibly time dependent, unit-length direction vectors necessary to describe the position, velocity, and acceleration of a spacecraft. Instead, the term "system" includes the description of the physical environment as well as the theories used in the definition of the coordinates [26]. Hence, a generic Reference System (RS) is uniquely defined by its origin, a fundamental plane, and the RF itself. The choice between using an inertial or non-inertial RS depends on the specific requirements

of the analysis being conducted. The primary distinction between these two types of systems lies in whether pseudo-accelerations, like the Coriolis effect observed in rotating RFs, are considered. In a nutshell: in an inertial RS Newton's first law, the law of inertia, holds true; in a non-inertial RS rotations and accelerations induce the presence of apparent forces.

A widely used reference frame in celestial mechanics and astrodynamics is the so-called Earth Mean Equator and Equinox of Epoch J2000 (EME2000), represented in Figure 2.1. Its origin coincides with the Earth's center, the reference plane is the equatorial plane, and its unit vectors  $\{\hat{\mathbf{I}}, \hat{\mathbf{J}}, \hat{\mathbf{K}}\}$  are defined as:

- $\hat{\mathbf{I}}$  aligned towards the direction of the Vernal equinox;
- $\hat{\mathbf{K}}$  normal to the reference plane;
- $\hat{\mathbf{J}}$  completing the triad.

Unlike the International Celestial Reference Frame (ICRF)<sup>1</sup>, which is the reference for ephemerides provided by the JPL [28], the EME2000 doesn't include nutations and librations, thus assuming the "quasi-inertial" status. However, given the difference between the dynamical EME2000 reference frame and the ICRF at a level of 0.01 arc second determined with an accuracy of 0.003 arc second [29], then the EME2000 RF is considered inertial.

Functional for tracing the motion of satellites are the perifocal RS and the non-inertial topocentric Zenith-East-North (ZEN), depicted in Figure 2.1. Their definition is not particularly relevant to this thesis work and are therefore mentioned only for completeness.

### 2.1.2 Equations of motion

The basis of the analytical description of the motion of bodies in space is a combination of two of Newton's laws: the second law of motion and the law of gravitation [23]. Actually, Johannes Kepler provided the first quantitative statements about

<sup>1</sup>The International Celestial Reference Frame (ICRF) was made to coincide almost exactly with the J2000 frame and is a catalog of adopted positions of 608 extragalactic radio sources, 212 of which are *defining sources* that establish the orientation of the International Celestial Reference System (ICRS) axes, with origin at the solar system barycenter [27].

orbital mechanics with the well-known first, second and third laws based entirely on empirical data, missing the concept of gravitational force. Some decades later, Isaac Newton developed the fundamental theory which explained why planetary motion satisfied these three laws.

According to the Kepler's first law, in the absence of external perturbations, the geometrical shape of the orbit of a planet is an ellipse with the Sun at one focus, whose equation in polar form is the conic equation:

$$r = \frac{a(1 - e^2)}{1 + e \cos \nu} = \frac{p}{1 + e \cos \nu}, \quad (2.1)$$

where  $a$ ,  $e$  and  $\nu$  are respectively the semi-major axis, the eccentricity and the true anomaly (three of six orbital parameters described later), and  $p$  is the *semilatus rectum*.

By combining Newton's second law of motion and law of gravitation and making some simplifying assumptions, one can demonstrate why and how the shapes and speeds of the orbits behave. Assuming to adopt an inertial reference system and the presence of only two spherically symmetric bodies, one of mass  $m$  and its primary of mass  $M$  such that  $M \gg m$  with constant values, one obtains the so-called Two-Body Problem (2BP) with its equation of motion

$$\ddot{\mathbf{r}} = -\frac{\mu}{r^2} \frac{\mathbf{r}}{r}, \quad (2.2)$$

where  $\mu = GM$ . From the non-linear equation (2.2), with some manipulations [23, 24, 30], it is possible to retrieve two constants of the motion, very useful in providing information about its solution  $\mathbf{r}(t)$  without actually obtaining it. The first one constant of motion is the *specific mechanical energy*

$$\mathcal{E} = \frac{V^2}{2} - \frac{\mu}{r}, \quad (2.3)$$

consisting of two terms, respectively the specific kinetic energy and potential energy, capable of providing important information about the shape of the orbit. The second useful result is the conservation of the *specific angular momentum*

$$\mathbf{h} = \mathbf{r} \times \mathbf{V}, \quad (2.4)$$

therefore the vector  $\mathbf{r}$  is normal to the constant vector  $\mathbf{h}$ . This suggests that the relative motion occurs within a fixed plane in space, i.e. the orbit plane, with  $\mathbf{h}$  as its normal vector. What Kepler's second law states, i.e. a line segment joining a planet and the Sun sweeps out equal areas during equal intervals of time, is a consequence of the principle of conservation of angular momentum.

A further manipulation of the equation of motion (2.2) in the 2BP domain, first performed by Newton, allows its analytical integration leading to an outstanding result:

$$r = \frac{h^2/\mu}{1 + (B/\mu) \cos v}, \quad (2.5)$$

where  $\mathbf{B}$  is a vector constant of integration and turns out to be an additional constant of the motion, and  $v$  is the angle between vectors  $\mathbf{B}$  and  $\mathbf{r}$ . As is immediately apparent, the equation (2.5) resembles the (2.1). Identifying  $p = h^2/\mu$ ,  $e = (B/\mu)$  and  $v$  as the true anomaly, it is evident that also equation (2.5) is the conic equation: ellipses match the mathematical form of gravitational orbits, confirming what Kepler stated. Note that, in general, gravitational orbits are conic sections, which include circles, ellipses, parabolas, and hyperbolas, based on values assumed by  $a, e$  and so on [30].

Finally, also the proportionality between the square of the orbital period of a planet (or, in general, the secondary body) and the cube of the semi-major axis of its orbit asserted by Kepler's third law is a natural consequence of the inverse-square gravitational force field of the sun (or, in general, the primary body).

To conclude this section, an overview of the six classical orbital elements (also known as *Keplerian elements*) is provided. Five independent quantities are sufficient to describe the size, shape, and orientation of an orbit while the last is needed to locate the orbiting body at a particular place and time. These elements are:

- $a$ , the *semi-major axis*, describing the size of the orbit;
- $e$ , the *eccentricity*, defining the shape of the orbit;
- $i$ , the *inclination*, the angle of the orbital plane wrt a reference plane;
- $\Omega$ , the *longitude of the ascending node*, an angle in the reference plane locating the ascending node in the line of nodes wrt a reference line;

- $\omega$ , the *argument of periapsis*, an angle in the orbital plane that identify the periapsis wrt the ascending node in the direction of motion;
- $v$ , the *true anomaly*, identifying the angular position of the orbiting body in the orbital plane, measured at epoch from the periapsis.

The choice of the more convenient reference plane usually falls on the Earth's equatorial plane in the case of a satellite orbiting the Earth or the ecliptic plane (i.e. the Earth's orbit plane around the Sun) for interplanetary trajectory, while the choice for the reference line is the direction from the Sun to *the first point in Aries*, a fixed point on the celestial sphere [23].

## 2.2 Three-Body Problem

As summarized in Section 2.1, the 2BP laid the foundations of modern astrodynamics, while greatly simplifying the reality. The Three-Body Problem (3BP) introduces a third interacting body to the Newtonian framework, exponentially increasing the complexity of the system. Indeed, unlike the 2BP where an elegant analytical solution exists, the 3BP does not yield to such straightforward closed-form solutions except in special cases. Hence, this escalation from two to three bodies marks a critical transition point in the study of dynamical systems although providing a sufficiently accurate framework for preliminary analysis directly applicable to real-world scenarios, more comprehensively characterized by the N-Body Problem (NBP).

The purpose of this section is to introduce a generic 3BP related to a generic binary system composed of two primary bodies revolving around its barycenter, both modeled as point-masses of value  $m_1$  and  $m_2$  for the bigger and smaller, respectively. The two primary body (which could be Sun and Earth for a SE system or Earth and Moon for a EM system) mutually influence the 3D motion of the third body (which could be the Moon in the first case and a SC in the second one). Under the assumption of negligible mass of the third body, the transition is from 3BP to Restricted Three-Body Problem (R3BP). Essentially, the third body is influenced by both gravitational forces of the two primary bodies without influencing their relative motion. The addition of a further hypothesis allows to shift to the Circular Restricted

Three-Body Problem (CR3BP): the primaries follow circular Keplerian orbits around their common center of mass.

### 2.2.1 Synodic Reference System

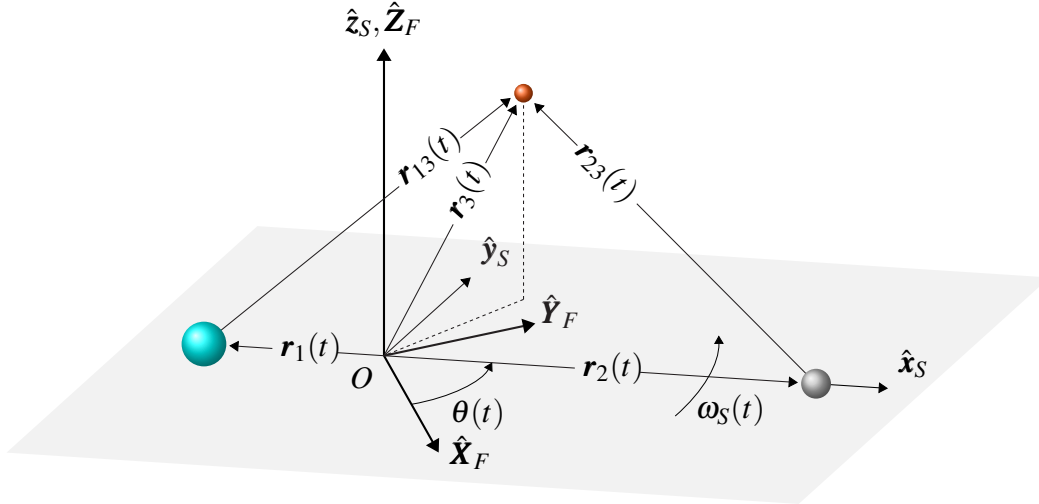


Fig. 2.2 Synodic reference system (not-to-scale)

The non-inertial rotating RF  $\{\hat{x}_S, \hat{y}_S, \hat{z}_S\}$  centered in the barycenter of the system, depicted in Figure 2.2, is called Synodic RF and its axes are defined as follows:

- $\hat{x}_S$  axis is aligned with the line connecting the two primaries;
- $\hat{z}_S$  axis is normal to the plane containing the orbits of the primaries;
- $\hat{y}_S$  axis completes the right hand triad.

Its angular velocity follows that of the two primaries wrt the inertial RF  $\{\hat{X}_F, \hat{Y}_F, \hat{Z}_F\}$  shown in Figure 2.2, namely  $\omega_S(t)$ .

Let  $\mathbf{r}_{ij}$  be defined as the position vector from the  $i$ -th to the  $j$ -th body:

$$\mathbf{r}_{ij}(t) = \mathbf{r}_{O_i}(t) - \mathbf{r}_{O_j}(t), \quad (2.6)$$

where the subscript  $O$  means wrt the origin. Then, The dimensional mean motion for the binary system can be expressed as

$$n(t) = \sqrt{\frac{\mu_1 + \mu_2}{r_{12}^3(t)}} = \sqrt{\frac{\mu^*}{r_{12}^3(t)}}, \quad (2.7)$$

with  $\mu^*$  indicating the sum of the specific gravitational parameters of the primaries. The angle between the inertial and the synodic RFs at epoch can be computed as

$$\theta(t) = n(t)t, \quad (2.8)$$

where  $t$  is the dimensional elapsed time in seconds. It is evident that if the distance  $r_{12}$  is not constant (e.g. with the use of planetary ephemerides), then  $\theta$  and  $n$  typically lead to roto-pulsating dynamics. In the CR3BP domain, the assumption of considering the orbits of the primaries as circular (meaning  $r_1$  and  $r_2$  have constant magnitudes) leads to a constant relative distance  $r_{12}$  as well as a constant mean motion  $n$  over time. Specifically, the prograde angle  $\theta$  that is swept out maintains a constant angular velocity  $\omega_S$ .

## 2.2.2 Nondimensionalization

As is commonly done in the literature [22, 24, 31–33], the next step involves nondimensionalizing the characteristic quantities of the CR3BP, namely length, mass and time. The constant distance of the two primaries is chosen to be the length unit, as mass unit is considered the sum of the two primaries masses and the time unit is then selected to make the orbital period of the two primaries about the system barycenter ( $\mathcal{T}_{sid}$ ) equal to  $2\pi$  time units [32]:

$$\ell^* = r_{12} = r_1 + r_2 \quad (2.9a)$$

$$m^* = m_1 + m_2 \quad (2.9b)$$

$$\mathcal{T}^* \triangleq \sqrt{\frac{(\ell^*)^3}{Gm^*}}. \quad (2.9c)$$

Hence, the non-dimensional quantities in the CR3BP result

$$\rho_{12} = \frac{r_{12}}{\ell^*} = 1, \quad (2.10a)$$

$$\mu \triangleq \frac{m_2}{m^*}, \quad (2.10b)$$

$$\tau_{sid} = \frac{\mathcal{T}_{sid}}{\mathcal{T}^*} = 2\pi. \quad (2.10c)$$

From equation (2.10b) one can express the two non-dimensional mass ratios as

$$\frac{\mu_2}{\mu^*} = \mu, \quad \frac{\mu_1}{\mu^*} = 1 - \mu, \quad (2.11)$$

and as of consequence, the barycenter wrt the bigger primary results

$$\rho_{CG} = \frac{\sum \rho_i \mu_i}{\sum \mu_i} = \mu, \quad (2.12)$$

resulting in the following non-dimensional coordinates of  $m_1$  and  $m_2$ :

$$\rho_1 = \frac{r_1}{\ell^*} = -\mu, \quad (2.13a)$$

$$\rho_2 = \frac{r_2}{\ell^*} = 1 - \mu. \quad (2.13b)$$

### 2.2.3 Equations of Motion

Adding a second primary body at equation (2.2), the compact form of the equations of motion results

$$\ddot{\mathbf{r}} = -\frac{\mu_1}{r_{13}^2} \frac{\mathbf{r}_{13}}{r_{13}} - \frac{\mu_2}{r_{23}^2} \frac{\mathbf{r}_{23}}{r_{23}}. \quad (2.14)$$

In order to lighten the notation, henceforth the subscript 3 is omitted for the SC, expressing its coordinates by  $\{x, y, z\}$  values. By projecting equation 2.14 in the synodic RF directions one has

$$\ddot{\mathbf{x}} = -\frac{\mu_1}{r_{13}^3} (x - x_1) - \frac{\mu_2}{r_{23}^3} (x - x_2) \quad (2.15a)$$

$$\ddot{\mathbf{y}} = -\frac{\mu_1}{r_{13}^3} y - \frac{\mu_2}{r_{23}^3} y \quad (2.15b)$$

$$\ddot{\mathbf{z}} = -\frac{\mu_1}{r_{13}^3} z - \frac{\mu_2}{r_{23}^3} z, \quad (2.15c)$$

where the relative positions are

$$r_{i3} = \sqrt{(x - x_i)^2 + y^2 + z^2}, \quad i = 1, 2, \quad (2.16)$$

being, as the synodic RF is defined,  $y_i$  and  $z_i$  equal to zero.

The next step involves the projection of eqs. (2.15) into the inertial RF, indicated by the prescript  $F$ , standing for "fixed" while the synodic one by  $R$ , standing for "rotating". It is worth recalling the transport theorem for a generic quantity  $\star$ ,

$$\frac{F d\star}{dt} = \frac{R d\star}{dt} + {}^{R/F}\boldsymbol{\omega}_S \times {}^R\star, \quad (2.17)$$

where  $R/F$  indicates a quantity measured in the rotating RF wrt the inertial one. The above theorem allows to write the velocity in the inertial RF as

$${}^F\dot{\mathbf{r}} = \frac{R d\mathbf{r}}{dt} + {}^{R/F}\boldsymbol{\omega}_S \times {}^R\mathbf{r}. \quad (2.18)$$

Analogously, in the inertial acceleration, three corrective terms appears:

$$\begin{aligned} {}^F\ddot{\mathbf{r}} &= \frac{F d\dot{\mathbf{r}}}{dt} = \frac{R d^F\dot{\mathbf{r}}}{dt} + {}^{R/F}\boldsymbol{\omega}_S \times {}^F\dot{\mathbf{r}} \\ &= \frac{R d}{dt} \left( {}^R\dot{\mathbf{r}} + {}^{R/F}\boldsymbol{\omega}_S \times {}^R\mathbf{r} \right) + {}^{R/F}\boldsymbol{\omega}_S \times \left( {}^R\dot{\mathbf{r}} + {}^{R/F}\boldsymbol{\omega}_S \times {}^R\mathbf{r} \right) \\ &= {}^R\ddot{\mathbf{r}} + {}^{R/F}\dot{\boldsymbol{\omega}}_S \times {}^R\mathbf{r} + {}^{R/F}\boldsymbol{\omega}_S \times {}^R\dot{\mathbf{r}} + {}^{R/F}\boldsymbol{\omega}_S \times {}^R\dot{\mathbf{r}} + {}^{R/F}\boldsymbol{\omega}_S \times \left( {}^{R/F}\boldsymbol{\omega}_S \times {}^R\mathbf{r} \right) \\ {}^F\ddot{\mathbf{r}} &= \ddot{\mathbf{r}} + \dot{\boldsymbol{\omega}}_S \times \mathbf{r} + 2\boldsymbol{\omega}_S \times \dot{\mathbf{r}} + \boldsymbol{\omega}_S \times (\boldsymbol{\omega}_S \times \mathbf{r}), \end{aligned} \quad (2.19)$$

in which in the last line, where all the terms are referred to the rotating RF, the prescripts  $R$  and  $R/F$  are omitted. On the right-hand side of eq. (2.19), after the first term representing the acceleration in the synodic RF, the tangential, centrifugal and Coriolis accelerations arise, respectively. Under the CR3BP assumptions, the variation of  $\boldsymbol{\omega}_S$  and  $r$  are null: the tangential and centripetal accelerations are zero, only Coriolis acceleration remains. However, for completeness a general case of 3BP is considered for now. Considering that  $\boldsymbol{\omega}_S = \omega_S \hat{\mathbf{z}}_S$  and expanding quantities in

the inertial velocity in eq. (2.19), its components result

$$\begin{aligned}
 {}^F \dot{\mathbf{r}} &= (\dot{x} \hat{\mathbf{x}}_S + \dot{y} \hat{\mathbf{y}}_S + \dot{z} \hat{\mathbf{z}}_S) + \begin{vmatrix} \hat{\mathbf{x}}_S & \hat{\mathbf{y}}_S & \hat{\mathbf{z}}_S \\ 0 & 0 & \boldsymbol{\omega}_S \\ x & y & z \end{vmatrix} \\
 &= (\dot{x} \hat{\mathbf{x}}_S + \dot{y} \hat{\mathbf{y}}_S + \dot{z} \hat{\mathbf{z}}_S) + [(-y\omega_S) \hat{\mathbf{x}}_S - (-x\omega_S) \hat{\mathbf{y}}_S + (0) \hat{\mathbf{z}}_S], \\
 {}^F \dot{\mathbf{r}} &= (\dot{x} - y\omega_S) \hat{\mathbf{x}}_S + (\dot{y} + x\omega_S) \hat{\mathbf{y}}_S + (\dot{z}) \hat{\mathbf{z}}_S. \tag{2.20}
 \end{aligned}$$

Similarly, the inertial acceleration shows the following components:

$$\begin{aligned}
 {}^F \ddot{\mathbf{r}} &= \ddot{\mathbf{r}} + \begin{vmatrix} \hat{\mathbf{x}}_S & \hat{\mathbf{y}}_S & \hat{\mathbf{z}}_S \\ 0 & 0 & \dot{\boldsymbol{\omega}}_S \\ x & y & z \end{vmatrix} + 2 \begin{vmatrix} \hat{\mathbf{x}}_S & \hat{\mathbf{y}}_S & \hat{\mathbf{z}}_S \\ 0 & 0 & \boldsymbol{\omega}_S \\ \dot{x} & \dot{y} & \dot{z} \end{vmatrix} + \boldsymbol{\omega}_S \times \begin{vmatrix} \hat{\mathbf{x}}_S & \hat{\mathbf{y}}_S & \hat{\mathbf{z}}_S \\ 0 & 0 & \boldsymbol{\omega}_S \\ x & y & z \end{vmatrix} \\
 &= (\ddot{x} - 2\dot{y}\omega_S - y\dot{\omega}_S) \hat{\mathbf{x}}_S + (\ddot{y} + 2\dot{x}\omega_S + x\dot{\omega}_S) \hat{\mathbf{y}}_S + (\ddot{z}) \hat{\mathbf{z}}_S + \begin{vmatrix} \hat{\mathbf{x}}_S & \hat{\mathbf{y}}_S & \hat{\mathbf{z}}_S \\ 0 & 0 & \boldsymbol{\omega}_S \\ -y\omega_S & x\omega_S & 0 \end{vmatrix}, \\
 {}^F \ddot{\mathbf{r}} &= (\ddot{x} - 2\dot{y}\omega_S - y\dot{\omega}_S - x\omega_S^2) \hat{\mathbf{x}}_S + (\ddot{y} + 2\dot{x}\omega_S + x\dot{\omega}_S - y\omega_S^2) \hat{\mathbf{y}}_S + (\ddot{z}) \hat{\mathbf{z}}_S. \tag{2.21}
 \end{aligned}$$

By equating the components of equations (2.15) and (2.21) individually, it is possible to obtain the full set of ODEs for the cartesian components

$$\ddot{x} - 2\dot{y}\omega_S - y\dot{\omega}_S - x\omega_S^2 = -\frac{\mu_1}{r_{13}^3}(x - x_1) - \frac{\mu_2}{r_{23}^3}(x - x_2) \tag{2.22a}$$

$$\ddot{y} + 2\dot{x}\omega_S + x\dot{\omega}_S - y\omega_S^2 = -\frac{\mu_1}{r_{13}^3}y - \frac{\mu_2}{r_{23}^3}y \tag{2.22b}$$

$$\ddot{z} = -\frac{\mu_1}{r_{13}^3}z - \frac{\mu_2}{r_{23}^3}z. \tag{2.22c}$$

Applying the simplifications and nondimensionalization of the CR3BP, namely  $\omega_{nd} = \omega_S/\omega_S^* = 1 \implies \dot{\omega}_{nd} = 0$ , and

$$\xi = \frac{x}{\ell^*} \tag{2.23a}$$

$$\eta = \frac{y}{\ell^*} \tag{2.23b}$$

$$\zeta = \frac{z}{\ell^*}, \tag{2.23c}$$

the full system of non-dimensional equations of motion for the cartesian components in the CR3BP dynamical model has the form

$$\ddot{\xi} - 2\dot{\eta} - \xi = -\frac{1-\mu}{\rho_{13}^3}(\xi + \mu) - \frac{\mu}{\rho_{23}^3}[\xi - (1-\mu)] \quad (2.24a)$$

$$\ddot{\eta} + 2\dot{\xi} - \eta = -\frac{1-\mu}{\rho_{13}^3}\eta - \frac{\mu}{\rho_{23}^3}\eta \quad (2.24b)$$

$$\ddot{\zeta} = -\frac{1-\mu}{\rho_{13}^3}\zeta - \frac{\mu}{\rho_{23}^3}\zeta. \quad (2.24c)$$

## 2.2.4 Jacobi Integral

Note that the equations (2.24) are three second-order, non-linear, coupled differential equations. Despite the simplifications adopted by CR3BP, it remains a system that cannot be solved analytically. However, it is possible to derive a pseudo-integral of motion in the rotating RF used to explore what trajectories the third body can follow given some initial energy state and as a means to verify the accuracy of a numerical integration [24]. The starting point is the definition of a positive potential function  $U$  in an inertial RF as

$${}^F U = \sum_{i=1}^2 \frac{\mu_i}{r_{i3}}, \quad (2.25)$$

where the subscript  $i$  is referred to each  $i$ -th primary body. Taking into account the centrifugal potential in a 3BP rotating RF, the equation above is modified as follows

$${}^R U = \frac{\mu_1}{r_{13}} + \frac{\mu_2}{r_{23}} + \frac{1}{2}\omega_S(x^2 + y^2), \quad (2.26)$$

and with CR3BP hypothesis and nondimensionalization it becomes

$${}^R \mathcal{U} = \frac{1-\mu}{\rho_{13}} + \frac{\mu}{\rho_{23}} + \frac{1}{2}(\xi^2 + \eta^2), \quad (2.27)$$

defined as *pseudopotential*. By taking it and deriving wrt non-dimensional coordinates one has

$$\frac{\partial \mathcal{U}}{\partial \xi} = \xi - \frac{1-\mu}{\rho_{13}^3}(\xi + \mu) - \frac{\mu}{\rho_{23}^3}[\xi - (1-\mu)] \quad (2.28a)$$

$$\frac{\partial \mathcal{U}}{\partial \eta} = \eta - \frac{1-\mu}{\rho_{13}^3}\eta - \frac{\mu}{\rho_{23}^3}\eta \quad (2.28b)$$

$$\frac{\partial \mathcal{U}}{\partial \zeta} = -\frac{1-\mu}{\rho_{13}^3}\zeta - \frac{\mu}{\rho_{23}^3}\zeta, \quad (2.28c)$$

which compared and combined to eqs. (2.24) yield

$$\ddot{\xi} - 2\dot{\eta} = \frac{\partial \mathcal{U}}{\partial \xi} \quad (2.29a)$$

$$\ddot{\eta} + 2\dot{\xi} = \frac{\partial \mathcal{U}}{\partial \eta} \quad (2.29b)$$

$$\ddot{\zeta} = \frac{\partial \mathcal{U}}{\partial \zeta}. \quad (2.29c)$$

Manipulating the dimensional equations (2.22) by multiplying the first with  $2\dot{x}$ , the second with  $2\dot{y}$  and the third with  $2\dot{z}$  and then summing them, one obtains

$$2\dot{x}\ddot{x} + 2\dot{y}\ddot{y} + 2\dot{z}\ddot{z} + 2\omega_S^2(\dot{x}x + \dot{y}y) = 2\dot{x}\frac{\partial U}{\partial x} + 2\dot{y}\frac{\partial U}{\partial y} + 2\dot{z}\frac{\partial U}{\partial z} = 2\frac{dU}{dt}, \quad (2.30)$$

whose integration produces the *Jacobi Integral*

$$\dot{x}^2 + \dot{y}^2 + \dot{z}^2 = V^2 = 2U - J_C, \quad (2.31)$$

which in non-dimensional form results

$$\dot{\xi}^2 + \dot{\eta}^2 + \dot{\zeta}^2 = \mathcal{V}^2 = 2\mathcal{U} - \mathcal{J}_C. \quad (2.32)$$

On the left-hand side there is the velocity squared in the synodic RF, dimensional and non-dimensional respectively. On the right-hand side the two terms are respectively the pseudopotential and the so-called Jacobi constant. The greater  $\mathcal{J}_C$  is, the less energy the SC has in the synodic RF, meaning that it is similar to an inverse energy-like quantity, analogous to the inverse of  $\mathcal{E}$  seen in eq. (2.3).

## 2.2.5 Lagrangian Points

For bodies in circular orbits about the system center of mass, Lagrange in his outstanding work [1] found five distinct three-body formations that are invariant when viewed from the rotating reference frame [24], called in his honor Lagrangian Points (LPs).

The initial step of Lagrange's approach involves setting the gradient vector of the pseudopotential function  $\nabla\mathcal{U}$  to zero. This equates to enforcing conditions of zero velocity and zero acceleration within the rotating reference frame, as can be deduced from eqs. (2.29), resulting

$$\frac{\partial\mathcal{U}}{\partial\xi} = 0 = \xi - \frac{1-\mu}{\rho_{13}^3}(\xi + \mu) - \frac{\mu}{\rho_{23}^3}[\xi - (1-\mu)] \quad (2.33a)$$

$$\frac{\partial\mathcal{U}}{\partial\eta} = 0 = \eta - \frac{1-\mu}{\rho_{13}^3}\eta - \frac{\mu}{\rho_{23}^3}\eta \quad (2.33b)$$

$$\frac{\partial\mathcal{U}}{\partial\zeta} = 0 = -\frac{1-\mu}{\rho_{13}^3}\zeta - \frac{\mu}{\rho_{23}^3}\zeta. \quad (2.33c)$$

From the above system it is possible to determine five set of non-dimensional coordinates  $\{\xi_i, \eta_i, \zeta_i\}$ , one per each LP. Observing the equation (2.33c) is immediately evident that it is satisfied for  $\zeta = 0$ , meaning that all the five LPs lie in the  $\hat{\xi}_S - \hat{\eta}_S$  plane. Then, eqs. (2.33a) and (2.33b) can be solved via substitution. By imposing  $\eta = \zeta = 0$ , one obtains a quintic equation,

$$\xi^5 \mp (3-\mu)\xi^4 + (3-2\mu)\xi^3 - \mu\xi^2 \pm 2\mu\xi - \mu = 0, \quad (2.34)$$

to be solved numerically, which yields three real roots corresponding to the so-called *collinear* libration points  $L_1, L_2$  and  $L_3$ , existing on the  $\hat{\xi}_S$ . The other two roots are named *triangular* collinear points  $L_4$  and  $L_5$ , being positioned at the vertices of the equilateral triangle obtained setting  $\rho_{13} = \rho_{23} = 1$  and having as base the primaries distance. As an example, the positions of LPs of a binary system with mass ratio of  $\mu = 0.1$  (almost ten time greater than EM one) are shown in Figure 2.3.

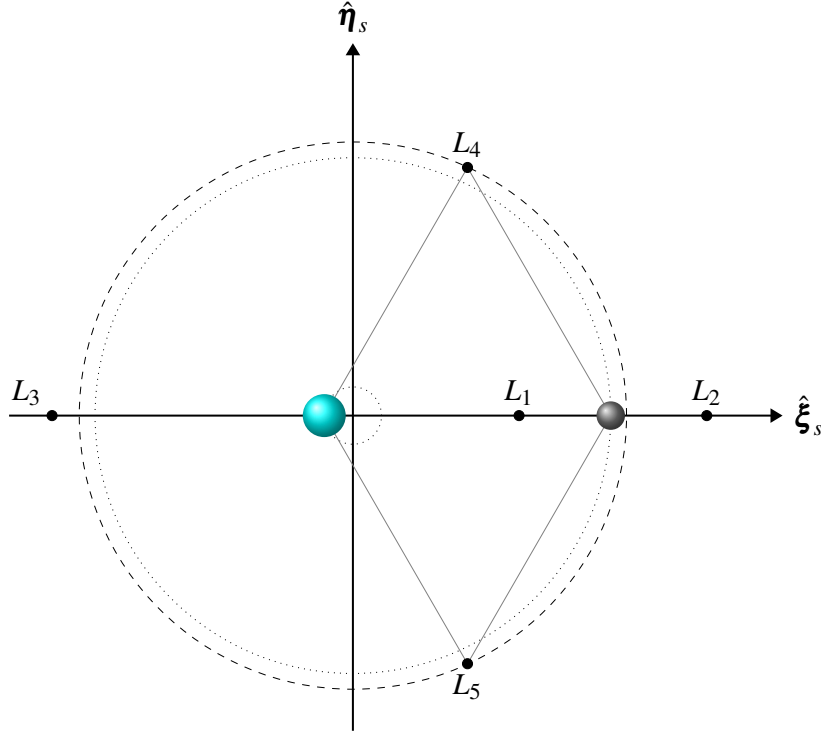


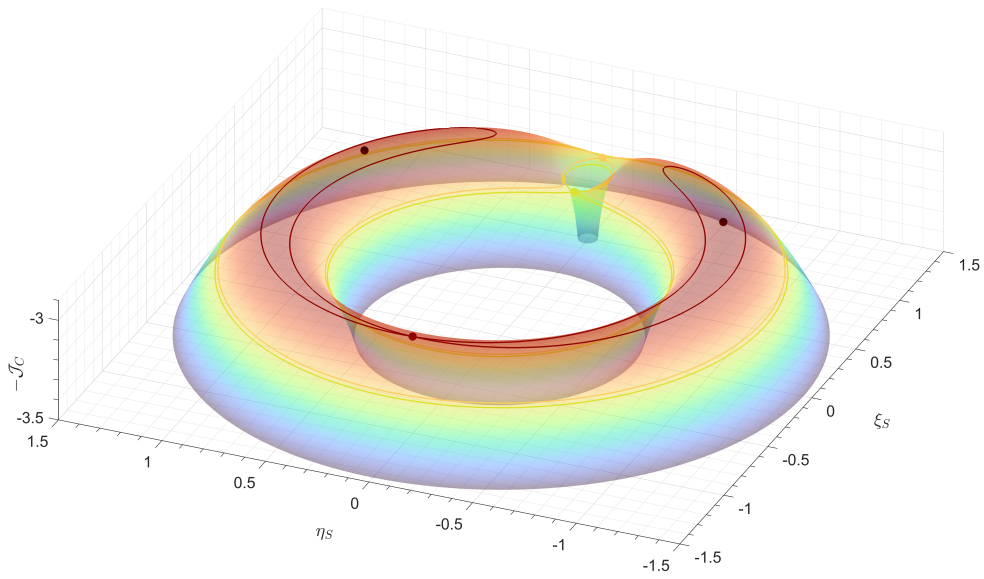
Fig. 2.3 LPs in a generic synodic RS with  $\mu = 0.1$

Note how  $L_3$  is located just outside the radial distance where  $L_4$  and  $L_5$  are found (defined by the outermost circle), while  $L_1$  and  $L_2$  appear to be at the same distance from the smaller primary, with  $L_2$  actually being slightly farther away. The other two circles represent the primaries' circular orbits, observed from an inertial RF, wrt the system barycenter.

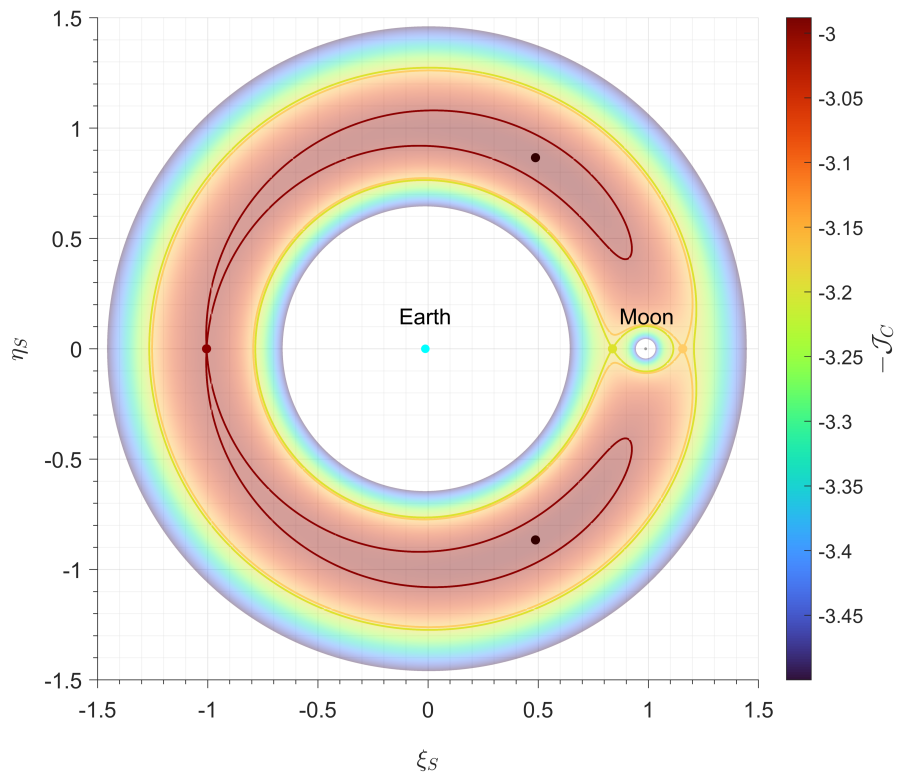
## 2.2.6 Zero Velocity Surfaces

A common application of the Jacobi integral is to define regions around  $m_1$  and  $m_2$  within which the third body (e.g. a SC) can move, based on its initial conditions. Extreme points on a trajectory occur whenever the velocity  $\mathcal{V}$  goes to zero. Therefore, setting  $\mathcal{V} = 0$  in the eq. (2.32) and explicating the pseudopotential  $\mathcal{U}$  as in eq. (2.27), for a specific Jacobi constant  $\mathcal{J}_C$  yields an algebraic expression for all feasible  $\{\xi, \eta, \zeta\}$  "apogee-like" locations, known as *Zero Velocity Surface (ZVS)*:

$$\mathcal{J}_C = 2\mathcal{U} = 2 \left( \frac{1-\mu}{\rho_{13}} + \frac{\mu}{\rho_{23}} \right) + (\xi^2 + \eta^2). \quad (2.35)$$



(a) 3D view



(b)  $\hat{\xi}_S - \hat{\eta}_S$  view

Fig. 2.4 Earth-Moon ZVSs

It should be noted that the null velocity being discussed is relative to the rotating RF, and thus the inertial velocity of the third body is not zero.

The surfaces defined by eq. (2.35) and illustrated for the EM system in Figure 2.4 delineate the geometric limits possible for a specified relative energy state. The more  $\mathcal{J}_C$  decreases, the more the energy increases and consequently the forbidden zones shrink (i.e. the SC widens its accessible regions).

The colored dots indicates the locations of each LP, coinciding with the local maxima of the function  $-\mathcal{J}_C$ , whose coordinates and Jacobi constant values are indicated in the following table.

	$\xi$	$\eta$	$\zeta$	$\mathcal{J}_C$
● $L_1$	0.83740242	0.00000000	0.00000000	3.188326
● $L_2$	1.15618808	0.00000000	0.00000000	3.172147
● $L_3$	-1.0056193	0.00000000	0.00000000	3.012145
● $L_4$	0.48785136	0.86602540	0.00000000	2.987999
● $L_5$	0.48785136	-0.86602540	0.00000000	2.987999

Table 2.1 EM LPs coordinates and Jacobi constants

The naming convention of the Lagrange Points (LPs) is based on the values of the Jacobi Constant in descending order, as shown in Table 2.1. This sequence also coincidentally reflects the order of accessibility of these points, based on their energy requirements. In fact, the LP associated with the highest non-dimensional  $\mathcal{J}_C$  value, which necessitates the lowest energy for access, is designated as the first, i.e.  $L_1$ . Subsequent points follow in order of decreasing JC values, meaning in ascending order of required energy. Notably,  $L_4$  and  $L_5$ , which have identical and the lowest  $\mathcal{J}_C$  values among the LPs, represent thresholds of energy accessibility. If a SC has the energy to reach these points, it can potentially access all regions within the CR3BP framework.

## 2.3 N-body Problem

For the sake of completeness, a brief description of the N-Body Problem (NBP) is provided, a model that more accurately reflect the complexities of the solar

system, incorporating the influences and disturbances caused by other celestial bodies and phenomena within the solar system. While the simplified model, such as CR3BP, serves as a valuable resource for initial analyses and considerations in multi-body dynamics, obtaining high-precision trajectory optimization necessitates employing a more detailed dynamical model, with the employment of JPL's planetary ephemerides.

In contrast to the 3BP, it is more advantageous to use a non-rotating reference system when handling the equations of motion in the NBP, employing the EME2000 RS using Earth as the central body.

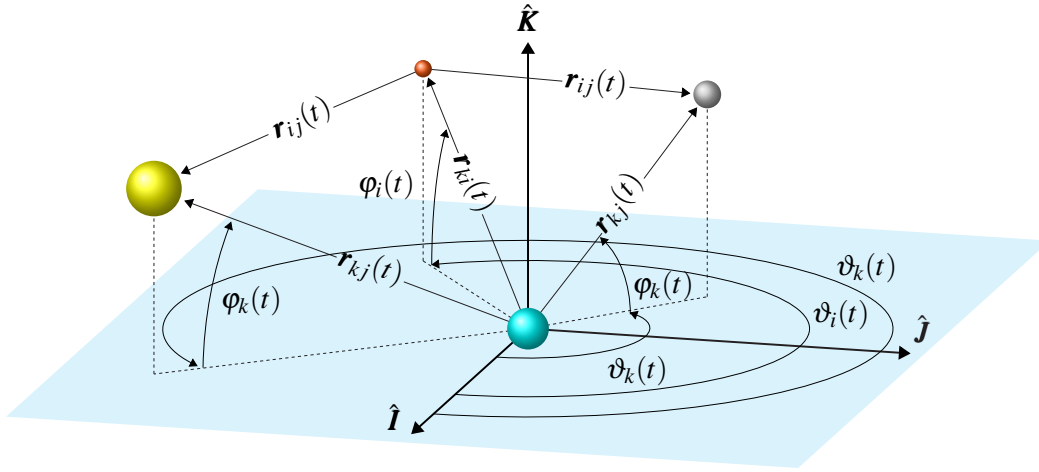


Fig. 2.5 N-Body Problem representation in EME2000 RF

As depicted in Figure 2.5, the central body is the  $k$ -th among the  $n$ , the subscript  $j$  refers to each gravitational body and  $i$  indicates the SC. Adopting a generic inertial RF one can express the SC acceleration as

$$\ddot{\mathbf{r}}_i = - \sum_{\substack{j=1 \\ j \neq i}}^n \frac{\mu_j}{r_{ji}^3} \mathbf{r}_{ji}, \quad (2.36)$$

but its formulation is more conveniently expressed if relative to the body chosen as central in the EME2000 RF, resulting in a set of second-order ODEs:

$$\ddot{\mathbf{r}}_{ki} = - \frac{(\mu_i + \mu_k)}{r_{ki}^3} \mathbf{r}_{ki} + \sum_{\substack{j=1 \\ j \neq i, k}}^n \mu_j \left( \frac{\mathbf{r}_{ij}}{r_{ij}^3} - \frac{\mathbf{r}_{kj}}{r_{kj}^3} \right). \quad (2.37)$$

It should be pointed out that all states in NBP are time-dependent, the notation  $(t)$  is omitted for clarity.

# Chapter 3

## Periodic Orbits

Chapter 3 focuses on the construction of families of Periodic Orbits (POs) within the CR3BP ultimately aiming to identify the LOP-G's Near-Rectilinear Halo Orbit (NRHO) which determines the initial conditions for the de-orbiting trajectories to be optimized, a process extensively described in the following chapters. As seen in Section 2.2, CR3BP dynamics is described by a time-invariant, autonomous system of epoch-independent equations that can be linearized to facilitate differential correction procedure, making it a very effective framework for generation of POs, which can be then converged in an N-body ephemeris model for higher-fidelity mission analyses.

Initially the methodologies employed for the construction and validation of Periodic Orbits (POs) within the CR3BP are described: through the implementation of a single-shooting method and the utilization of the State Transition Matrix (STM), the Differential Correction (DC) process enables the identification and construction of exact periodic motions across specific families of orbits. Specifically, the EML<sub>2</sub> Lyapunov Orbits (LOs) and then bifurcating Halo Orbits (HOs) families are obtained via continuation strategies.

How such POs families can be transitioned into Quasi-Periodic Orbits (QPOs) in the NBP is not a primary focus of this thesis and can be found in Mascolo's PhD dissertation [22].

### 3.1 An analytical approximation

To investigate the behavior of a spacecraft in proximity to LPs within the CR3BP domain, it is useful to linearize the equations of motion from equations (2.29) near these equilibrium points, by applying a Taylor series expansion to the right-hand side of each one:

$$\ddot{\xi} - 2\dot{\eta} = \mathcal{U}_{\xi\xi}|_{LP}\xi + \mathcal{U}_{\xi\eta}|_{LP}\eta + \mathcal{U}_{\xi\zeta}|_{LP}\zeta \quad (3.1a)$$

$$\dot{\eta} + 2\dot{\xi} = \mathcal{U}_{\eta\xi}|_{LP}\xi + \mathcal{U}_{\eta\eta}|_{LP}\eta + \mathcal{U}_{\eta\zeta}|_{LP}\zeta \quad (3.1b)$$

$$\ddot{\zeta} = \mathcal{U}_{\zeta\xi}|_{LP}\xi + \mathcal{U}_{\zeta\eta}|_{LP}\eta + \mathcal{U}_{\zeta\zeta}|_{LP}\zeta, \quad (3.1c)$$

where the generic second partial derivative is expressed as

$$\frac{\partial^2 \mathcal{U}}{\partial \bullet \partial \circ} \triangleq \mathcal{U}_{\bullet\circ}, \quad (3.2)$$

with the  $LP$  subscript meaning that is computed at the LPs, henceforth omitted for brevity. Since all the LPs lie in the  $\hat{\xi}_S - \hat{\eta}_S$  plane, as derived in Section 2.2.5, the mixed partial derivatives containing  $\zeta$  go to zero by definition:  $\mathcal{U}_{\xi\zeta} = \mathcal{U}_{\eta\zeta} = 0$ . This allows for the decoupling of the last equation (3.1c), which is essentially a harmonic in the  $\hat{\xi}_S$  direction

$$\ddot{\zeta} = \mathcal{U}_{\zeta\zeta}\zeta, \quad \zeta = A_\zeta \cos(\omega_\zeta \tau) + B_\zeta \sin(\omega_\zeta \tau), \quad (3.3)$$

with the acceleration  $\ddot{\zeta}$  producing an out-of-plane motion  $\zeta$  whose variation has a linear, negligible influence on the in-plane motion in the  $\xi$  and  $\eta$  directions [22]. The constants  $A_\zeta$  and  $B_\zeta$  depends on the initial condition, while the out-of-plane frequency is

$$\omega_\zeta^2 = -\mathcal{U}_{\zeta\zeta}. \quad (3.4)$$

On the other hand, the equations (3.1a) and (3.1b) are two coupled second-order ODEs, more conveniently transformed in a set of four first-order ODEs

$$\begin{Bmatrix} \dot{\xi} \\ \dot{\eta} \\ \dot{\xi} \\ \dot{\eta} \end{Bmatrix} = \begin{bmatrix} 0 & 0 & 1 & 0 \\ 0 & 0 & 0 & 1 \\ \mathcal{U}_{\xi\xi} & \mathcal{U}_{\xi\eta} & 0 & 2 \\ \mathcal{U}_{\eta\xi} & \mathcal{U}_{\eta\eta} & -2 & 0 \end{bmatrix} \begin{Bmatrix} \xi \\ \eta \\ \dot{\xi} \\ \dot{\eta} \end{Bmatrix}, \quad (3.5)$$

whose matricial form is

$$\dot{\tilde{\mathbf{X}}} = \tilde{\mathbf{A}}\tilde{\mathbf{X}}, \quad (3.6)$$

where  $\tilde{\mathbf{A}}$  is the non-dimensional Jacobian matrix and  $\tilde{\mathbf{X}}$  is the non-dimensional state vector of the SC (with  $\zeta$  and  $\dot{\zeta}$  missing, due to the planarity of motion). The complete form of the Jacobian matrix and the first and second partial derivatives can be retrieved in Appendix A.

Now, following the Szebehely's procedure [34], at the three collinear points for  $0 < \mu < 1/2$

$$\mathcal{U}_{\xi\eta} = 0, \quad \mathcal{U}_{\xi\xi} > 0, \quad \mathcal{U}_{\eta\eta} < 0,$$

therefore the characteristic polynomial of matrix  $\tilde{\mathbf{A}}$  is of the form

$$\Lambda^2 + 2\beta_1\Lambda - \beta_2^2 = 0, \quad (3.7)$$

where

$$\Lambda = \lambda^2 \quad (3.8a)$$

$$\beta_1 = 2 - \frac{\mathcal{U}_{\xi\xi} + \mathcal{U}_{\eta\eta}}{2} \quad (3.8b)$$

$$\beta_2^2 = -\mathcal{U}_{\xi\xi}\mathcal{U}_{\eta\eta}. \quad (3.8c)$$

Two pairs of eigenvalues can be derived, of which  $\lambda_1$  and  $\lambda_2$  are real while  $\lambda_3$  and  $\lambda_4$  are imaginary. In particular, the first imaginary solution provides the in-plane frequency of the linearized PO

$$\omega_3 = -i\lambda_3. \quad (3.9)$$

The solutions for  $\xi(\tau)$  and  $\eta(\tau)$  are coupled and include aperiodic exponential instabilities and aperiodic decays. However, through additional mathematical manipulation and by setting all aperiodic exponential instabilities to zero [35], a much

simpler set of equations of motion is derived, taking the form of

$$\xi(\tau) = A_\xi \cos(\omega_3 \tau + \phi) \quad (3.10a)$$

$$\eta(\tau) = -c_2 A_\xi \sin(\omega_3 \tau + \phi) \quad (3.10b)$$

$$\zeta(\tau) = A_\zeta \cos(\omega_\zeta \tau + \psi) \quad (3.10c)$$

$$\dot{\xi}(\tau) = -A_\xi \omega_3 \sin(\omega_3 \tau + \phi) \quad (3.10d)$$

$$\dot{\eta}(\tau) = -c_2 A_\xi \omega_3 \cos(\omega_3 \tau + \phi) \quad (3.10e)$$

$$\dot{\zeta}(\tau) = -A_\zeta \omega_\zeta \sin(\omega_\zeta \tau + \psi), \quad (3.10f)$$

in which one can simply specify an amplitude  $A_\xi$  in the  $\xi$  direction and consequently derive  $A_\eta = c_2 A_\xi$  in the  $\eta$  direction, which can be interpreted as semi-minor and semi-major axes, respectively.

Trajectories derived from the equations in (3.10) can serve as initial seeds for differential correction methods. Specifically, by using the initial state vector  $\tilde{\mathbf{X}}^a(\tau_0) = \{\xi_0, \eta_0, \zeta_0, \dot{\xi}_0, \dot{\eta}_0, \dot{\zeta}_0\}^T$  analytical propagation yields an indefinitely stable elliptical orbit. Instead, employing the same  $\tilde{\mathbf{X}}^a(\tau_0)$  as the initial state, non-linear integration of the CR3BP equations of motion may still lead to divergent behaviors. Complete and detailed analyses on how to predict the evolution and stability of such POs can be found in literature and are beyond the scope and the utility of this thesis [36–39].

## 3.2 Differential Correction

The strategy pursued to find a specified path involves adjusting an initial state,  $\tilde{\mathbf{X}}(\tau_0)$ , to achieve a desired final state  $\tilde{\mathbf{X}}(\tilde{\mathbf{X}}(\tau_0), \tau_f)$ , not blindly and randomly, but exploring the interdependency between initial and terminal conditions along the trajectory, falling within the classic framework of a Two-Point Boundary Value Problem (TP-BVP). Essentially, the goal of the Differential Correction (DC) procedure is to explore the sensitivity of initial and final conditions to changes in either, thereby assessing how modifications in one condition can influence the outcomes in the other.

The discrepancy, or perturbation state, i.e. the variation between the actual and desired final states, can be described as

$$\delta\tilde{\mathbf{X}}(\tau_f) = \tilde{\mathbf{X}}(\tilde{\mathbf{X}}(\tau_0), \tau_f) - \tilde{\mathbf{X}}^*(\tilde{\mathbf{X}}^*(\tau_0), \tau_f), \quad (3.11)$$

where the asterisk is referred to the desired state. The implemented here differential correction procedure is designed to eliminate the discrepancies between two states. If one assumes that a specific correction  $\delta\tilde{\mathbf{X}}(\tau_0)$  produces the desired initial state, namely

$$\tilde{\mathbf{X}}^*(\tau_0) = \tilde{\mathbf{X}}(\tau_0) + \delta\tilde{\mathbf{X}}(\tau_0), \quad (3.12)$$

then the equation (3.11) can be expanded and linearized as follows:

$$\begin{aligned} \delta\tilde{\mathbf{X}}(\tau_f) &= \tilde{\mathbf{X}}(\tilde{\mathbf{X}}(\tau_0), \tau_f) - \tilde{\mathbf{X}}^*(\tilde{\mathbf{X}}^*(\tau_0), \tau_f) \\ &= \tilde{\mathbf{X}}(\tilde{\mathbf{X}}(\tau_0), \tau_f) - \tilde{\mathbf{X}}^*(\tilde{\mathbf{X}}(\tau_0) + \delta\tilde{\mathbf{X}}(\tau_0), \tau_f) \\ &= \frac{\partial\tilde{\mathbf{X}}(\tau_f)}{\partial\tilde{\mathbf{X}}(\tau_0)} \delta\tilde{\mathbf{X}}(\tau_0), \\ \delta\tilde{\mathbf{X}}(\tau_f) &= \tilde{\Phi}(\tau_f, \tau_0) \delta\tilde{\mathbf{X}}(\tau_0). \end{aligned} \quad (3.13)$$

The symbol  $\tilde{\Phi}(\tau_f, \tau_0)$  in the right-hand side of eq. (3.13) denote the so-called State Transition Matrix (STM), representing the partial derivative of all state quantities at a specified final time,  $\tau_f$ , wrt the same state quantities computed at the initial time  $\tau_0$ . Such linear mapping, evaluated at a generic time  $\tau > \tau_0$ , can be written

explicitly in its general form as

$$\tilde{\Phi}(\tau, \tau_0) = \begin{bmatrix} \frac{\partial \xi}{\partial \xi_0} & \frac{\partial \xi}{\partial \eta_0} & \frac{\partial \xi}{\partial \zeta_0} & \frac{\partial \xi}{\partial \dot{\xi}_0} & \frac{\partial \xi}{\partial \dot{\eta}_0} & \frac{\partial \xi}{\partial \dot{\zeta}_0} \\ \frac{\partial \eta}{\partial \xi_0} & \frac{\partial \eta}{\partial \eta_0} & \frac{\partial \eta}{\partial \zeta_0} & \frac{\partial \eta}{\partial \dot{\xi}_0} & \frac{\partial \eta}{\partial \dot{\eta}_0} & \frac{\partial \eta}{\partial \dot{\zeta}_0} \\ \frac{\partial \zeta}{\partial \xi_0} & \frac{\partial \zeta}{\partial \eta_0} & \frac{\partial \zeta}{\partial \zeta_0} & \frac{\partial \zeta}{\partial \dot{\xi}_0} & \frac{\partial \zeta}{\partial \dot{\eta}_0} & \frac{\partial \zeta}{\partial \dot{\zeta}_0} \\ \frac{\partial \dot{\xi}}{\partial \xi_0} & \frac{\partial \dot{\xi}}{\partial \eta_0} & \frac{\partial \dot{\xi}}{\partial \zeta_0} & \frac{\partial \dot{\xi}}{\partial \dot{\xi}_0} & \frac{\partial \dot{\xi}}{\partial \dot{\eta}_0} & \frac{\partial \dot{\xi}}{\partial \dot{\zeta}_0} \\ \frac{\partial \dot{\eta}}{\partial \xi_0} & \frac{\partial \dot{\eta}}{\partial \eta_0} & \frac{\partial \dot{\eta}}{\partial \zeta_0} & \frac{\partial \dot{\eta}}{\partial \dot{\xi}_0} & \frac{\partial \dot{\eta}}{\partial \dot{\eta}_0} & \frac{\partial \dot{\eta}}{\partial \dot{\zeta}_0} \\ \frac{\partial \dot{\zeta}}{\partial \xi_0} & \frac{\partial \dot{\zeta}}{\partial \eta_0} & \frac{\partial \dot{\zeta}}{\partial \zeta_0} & \frac{\partial \dot{\zeta}}{\partial \dot{\xi}_0} & \frac{\partial \dot{\zeta}}{\partial \dot{\eta}_0} & \frac{\partial \dot{\zeta}}{\partial \dot{\zeta}_0} \end{bmatrix} = \left[ \begin{array}{c|c} \tilde{\Phi}_{\rho\rho} & \tilde{\Phi}_{\rho\nu} \\ \tilde{\Phi}_{\nu\rho} & \tilde{\Phi}_{\nu\nu} \end{array} \right], \quad (3.14)$$

where the subscript 0 stands for  $(\tau_0)$  and the generic  $\tau$  is omitted at the numerator to make the notation more legible. The above STM can be seen as formed by four  $3 \times 3$  submatrices of partial derivatives: the subscripts  $\rho$  and  $\nu$  are used to denote the variables in the numerator and the denominator of the partial derivatives, according to the order in which they appear. Specifically,  $\rho$  corresponds to the vector  $\boldsymbol{\rho}$  containing the positional quantities, on the other hand  $\nu$  denotes the vector of velocities  $\boldsymbol{\mathcal{V}}$ , encapsulating the velocity components. From now on, the following shortenings are adopted to simplify the notation of the equations:

$$\tilde{\mathbf{X}}_0 \triangleq \tilde{\mathbf{X}}(\tau_0), \quad (3.15a)$$

$$\tilde{\mathbf{X}} \triangleq \tilde{\mathbf{X}}(\tilde{\mathbf{X}}(\tau_0), \tau). \quad (3.15b)$$

The STM is frequently referred to as the *sensitivity matrix* because it quantifies the extent to which variations in the final state are affected by perturbations and modifications in the initial state. Consequently, the STM evolves alongside the trajectory it describes, following the same dynamic path. Accordingly, the evolution of the STM is governed by its own set of 36 ODEs. Hence,

$$\dot{\tilde{\Phi}}(\tau, \tau_0) = \frac{d}{d\tau} \tilde{\Phi} = \frac{d}{d\tau} \left( \frac{\partial \tilde{\mathbf{X}}}{\partial \tilde{\mathbf{X}}_0} \right) = \frac{\partial}{\partial \tilde{\mathbf{X}}_0} \left( \frac{d\tilde{\mathbf{X}}}{d\tau} \right) = \frac{\partial \dot{\tilde{\mathbf{X}}}}{\partial \tilde{\mathbf{X}}} \frac{\partial \tilde{\mathbf{X}}}{\partial \tilde{\mathbf{X}}_0}$$

$$\dot{\tilde{\Phi}}(\tau, \tau_0) = \tilde{\mathbf{A}}(\tau) \tilde{\Phi}(\tau, \tau_0), \quad (3.16)$$

in which appears, again, the non-dimensional Jacobian Matrix, essential for computing the evolution of the STM itself. Note that, considering the full CR3BP set of state equations (3.1),  $\tilde{\mathbf{A}}(\tau) \in \mathbb{R}^{6 \times 6}$  has its complete form, composed by for square  $3 \times 3$  submatrices

$$\tilde{\mathbf{A}}(\tau) = \left[ \begin{array}{c|c} \mathbf{0} & \mathbf{I} \\ \mathbf{U} & \mathbf{\Omega} \end{array} \right], \quad (3.17)$$

explicitly expressed as

$$\tilde{\mathbf{A}}(\tau) = \begin{bmatrix} 0 & 0 & 0 & 1 & 0 & 0 \\ 0 & 0 & 0 & 0 & 1 & 0 \\ 0 & 0 & 0 & 0 & 0 & 1 \\ \mathcal{U}_{\xi\xi} & \mathcal{U}_{\xi\eta} & \mathcal{U}_{\xi\zeta} & 0 & 2 & 0 \\ \mathcal{U}_{\eta\xi} & \mathcal{U}_{\eta\eta} & \mathcal{U}_{\eta\zeta} & -2 & 0 & 0 \\ \mathcal{U}_{\zeta\xi} & \mathcal{U}_{\zeta\eta} & \mathcal{U}_{\zeta\zeta} & 0 & 0 & 0 \end{bmatrix}. \quad (3.18)$$

The explicit form of the terms in submatrix  $\mathbf{U}$ , containing all the second partial derivatives of the pseudopotential, are presented in Appendix A.

### 3.3 Single-Shooting Method

In a single-shooting method, the problem is approached by guessing initial conditions and integrating the differential equations to see how closely the resulting trajectory meets the specified boundary conditions at the endpoint and eventually restarting with a new initial guess. The key to the here implemented single-shooting method lies in the adjustment of the initial conditions based on the discrepancies observed at the final boundary, via differential correction. This adjustment process typically involves the use of iterative techniques which refines the initial conditions at each  $r$ -th step by considering the sensitivity of the endpoint conditions to changes in the initial state. However, it should be considered that not all values of the initial state may be allowed to vary and, likewise, there could be final state values free to assume any value. Hence, let  $\tilde{\mathbf{X}}_0 \in \mathbb{R}^{n \times 1}$  be the free-variable vector

$$\tilde{\mathbf{X}}_0 = \{X_1, X_2, \dots, X_n\}^T, \quad (3.19)$$

it may contains positions, velocities and also integration times. On the other hand, the constraint vector  $\boldsymbol{\chi}(\tilde{\mathbf{X}}_0) \in \mathbb{R}^{m \times 1}$  must be defined,

$$\boldsymbol{\chi}(\tilde{\mathbf{X}}_0) = \{\chi_1, \chi_2, \dots, \chi_m\}^T, \quad (3.20)$$

targeting the desired final quantities. In the specific case of POs construction, the complete free-variable vector and constraint vector are written as

$$\tilde{\mathbf{X}}_0 = \begin{pmatrix} \xi \\ \eta \\ \zeta \\ \dot{\xi} \\ \dot{\eta} \\ \dot{\zeta} \\ \tau \end{pmatrix}, \quad \boldsymbol{\chi}(\tilde{\mathbf{X}}_0) = \begin{pmatrix} \xi - \xi^* \\ \eta - \eta^* \\ \zeta - \zeta^* \\ \dot{\xi} - \dot{\xi}^* \\ \dot{\eta} - \dot{\eta}^* \\ \dot{\zeta} - \dot{\zeta}^* \end{pmatrix}, \quad (3.21)$$

in which the integration time coincides with the period of the specific PO, namely  $\tau = \tau_f - \tau_0$ . The constraint vector instead contains the differences between actual and desired final state. It should be noted that including the time constraint in this vector is not needed, as it suffices to exclude it from the free-variable vector and directly specify the period of the PO when it is known.

Essentially, the method aims at searching the specific initial state  $\tilde{\mathbf{X}}_0^*$  that satisfies all the constraints, namely  $\boldsymbol{\chi}(\tilde{\mathbf{X}}_0^*) = \mathbf{0}$ . To quantify how variations in the free-variable vector influence the constraint vector, a first-order Taylor expansion is applied, indicating with  $\tilde{\mathbf{X}}$  a new generic initial free-variable vector:

$$\boldsymbol{\chi}(\tilde{\mathbf{X}}) = \boldsymbol{\chi}(\tilde{\mathbf{X}}_0) + \frac{\partial \boldsymbol{\chi}(\tilde{\mathbf{X}}_0)}{\partial \tilde{\mathbf{X}}} (\tilde{\mathbf{X}} - \tilde{\mathbf{X}}_0). \quad (3.22)$$

Again, the partial derivatives of the constraints wrt the forward-in-time free-variable vector quantities form a Jacobian matrix  $\tilde{\mathbf{J}}(\boldsymbol{\chi}(\tilde{\mathbf{X}}_0), \tilde{\mathbf{X}}) \in \mathbb{R}^{m \times n}$ :

$$\frac{\partial \boldsymbol{\chi}(\tilde{\mathbf{X}}_0)}{\partial \tilde{\mathbf{X}}} = \tilde{\mathbf{J}}(\boldsymbol{\chi}(\tilde{\mathbf{X}}_0), \tilde{\mathbf{X}}) = \begin{bmatrix} \frac{\partial \chi_1}{\partial \tilde{X}_1} & \frac{\partial \chi_1}{\partial \tilde{X}_2} & \cdots & \frac{\partial \chi_1}{\partial \tilde{X}_n} \\ \frac{\partial \chi_2}{\partial \tilde{X}_1} & \frac{\partial \chi_2}{\partial \tilde{X}_2} & \cdots & \frac{\partial \chi_2}{\partial \tilde{X}_n} \\ \vdots & \vdots & \ddots & \vdots \\ \frac{\partial \chi_m}{\partial \tilde{X}_1} & \frac{\partial \chi_m}{\partial \tilde{X}_2} & \cdots & \frac{\partial \chi_m}{\partial \tilde{X}_n} \end{bmatrix}. \quad (3.23)$$

Specifically for this analysis, in the most general case the Jacobian becomes a  $6 \times 7$  matrix:

$$\tilde{\mathbf{J}}(\boldsymbol{\chi}(\tilde{\mathbf{X}}_0), \tilde{\mathbf{X}}) = \begin{bmatrix} \frac{\partial \xi_f}{\partial \xi_0} & \frac{\partial \xi_f}{\partial \eta_0} & \frac{\partial \xi_f}{\partial \zeta_0} & \frac{\partial \xi_f}{\partial \dot{\xi}_0} & \frac{\partial \xi_f}{\partial \dot{\eta}_0} & \frac{\partial \xi_f}{\partial \dot{\zeta}_0} & \frac{\partial \xi_f}{\partial \tau} \\ \frac{\partial \eta_f}{\partial \xi_0} & \frac{\partial \eta_f}{\partial \eta_0} & \frac{\partial \eta_f}{\partial \zeta_0} & \frac{\partial \eta_f}{\partial \dot{\xi}_0} & \frac{\partial \eta_f}{\partial \dot{\eta}_0} & \frac{\partial \eta_f}{\partial \dot{\zeta}_0} & \frac{\partial \eta_f}{\partial \tau} \\ \frac{\partial \zeta_f}{\partial \xi_0} & \frac{\partial \zeta_f}{\partial \eta_0} & \frac{\partial \zeta_f}{\partial \zeta_0} & \frac{\partial \zeta_f}{\partial \dot{\xi}_0} & \frac{\partial \zeta_f}{\partial \dot{\eta}_0} & \frac{\partial \zeta_f}{\partial \dot{\zeta}_0} & \frac{\partial \zeta_f}{\partial \tau} \\ \frac{\partial \dot{\xi}_f}{\partial \xi_0} & \frac{\partial \dot{\xi}_f}{\partial \eta_0} & \frac{\partial \dot{\xi}_f}{\partial \zeta_0} & \frac{\partial \dot{\xi}_f}{\partial \dot{\xi}_0} & \frac{\partial \dot{\xi}_f}{\partial \dot{\eta}_0} & \frac{\partial \dot{\xi}_f}{\partial \dot{\zeta}_0} & \frac{\partial \dot{\xi}_f}{\partial \tau} \\ \frac{\partial \dot{\eta}_f}{\partial \xi_0} & \frac{\partial \dot{\eta}_f}{\partial \eta_0} & \frac{\partial \dot{\eta}_f}{\partial \zeta_0} & \frac{\partial \dot{\eta}_f}{\partial \dot{\xi}_0} & \frac{\partial \dot{\eta}_f}{\partial \dot{\eta}_0} & \frac{\partial \dot{\eta}_f}{\partial \dot{\zeta}_0} & \frac{\partial \dot{\eta}_f}{\partial \tau} \\ \frac{\partial \dot{\zeta}_f}{\partial \xi_0} & \frac{\partial \dot{\zeta}_f}{\partial \eta_0} & \frac{\partial \dot{\zeta}_f}{\partial \zeta_0} & \frac{\partial \dot{\zeta}_f}{\partial \dot{\xi}_0} & \frac{\partial \dot{\zeta}_f}{\partial \dot{\eta}_0} & \frac{\partial \dot{\zeta}_f}{\partial \dot{\zeta}_0} & \frac{\partial \dot{\zeta}_f}{\partial \tau} \end{bmatrix}, \quad (3.24)$$

coinciding with the definition of the STM in equation (3.14) with the addition of a further column comprising the derivative of the state quantities, namely velocities and accelerations. Denoting as  $\varphi_{ij}$  each element of the STM in equation (3.14), the

(3.24) is rewritten in a more compact form:

$$\tilde{\mathbf{J}}(\boldsymbol{\chi}(\tilde{\mathbf{X}}_0), \tilde{\mathbf{X}}) = \begin{bmatrix} \varphi_{11} & \varphi_{12} & \varphi_{13} & \varphi_{14} & \varphi_{15} & \varphi_{16} & \dot{\xi}_f \\ \varphi_{21} & \varphi_{22} & \varphi_{23} & \varphi_{24} & \varphi_{25} & \varphi_{26} & \dot{\eta}_f \\ \varphi_{31} & \varphi_{32} & \varphi_{33} & \varphi_{34} & \varphi_{35} & \varphi_{36} & \dot{\zeta}_f \\ \varphi_{41} & \varphi_{42} & \varphi_{43} & \varphi_{44} & \varphi_{45} & \varphi_{46} & \ddot{\xi}_f \\ \varphi_{51} & \varphi_{52} & \varphi_{53} & \varphi_{54} & \varphi_{55} & \varphi_{56} & \dot{\eta}_f \\ \varphi_{61} & \varphi_{62} & \varphi_{63} & \varphi_{64} & \varphi_{65} & \varphi_{66} & \ddot{\zeta}_f \end{bmatrix}. \quad (3.25)$$

Such a correction scheme is known as Variable-Time Differential Correction (VTDC) and evaluates the influence of the integration time on the final state; otherwise, if the integration time is not a free-variable quantity, then the Jacobian matrix fully coincides with the STM and the correction method employed is referred to as Fixed-Time Differential Correction (FTDC).

Now, in order to obtain an iterative form, the Taylor expansion in eq. (3.22) is written by relating the subsequent step  $r + 1$  to the previous  $r$ -th, obtaining

$$\boldsymbol{\chi}(\tilde{\mathbf{X}}_{r+1}) = \boldsymbol{\chi}(\tilde{\mathbf{X}}_r) + \frac{\partial \boldsymbol{\chi}(\tilde{\mathbf{X}}_r)}{\partial \tilde{\mathbf{X}}_{r+1}} (\tilde{\mathbf{X}}_{r+1} - \tilde{\mathbf{X}}_r). \quad (3.26)$$

For the sake of clarity, the following shortenings are introduced:

$$\boldsymbol{\chi}_r \triangleq \boldsymbol{\chi}(\tilde{\mathbf{X}}_r), \quad (3.27a)$$

$$\tilde{\mathbf{J}}(\boldsymbol{\chi}_r) \triangleq \tilde{\mathbf{J}}(\boldsymbol{\chi}(\tilde{\mathbf{X}}_r), \tilde{\mathbf{X}}_{r+1}). \quad (3.27b)$$

If a solution exists, then  $\boldsymbol{\chi}_{r+1} = \mathbf{0}$  and the iterative form in equation (3.26) becomes

$$\boldsymbol{\chi}_r + [\tilde{\mathbf{J}}(\boldsymbol{\chi}_r)] (\tilde{\mathbf{X}}_{r+1} - \tilde{\mathbf{X}}_r) = \mathbf{0}. \quad (3.28)$$

Therefore, at each iteration, the updated values of the constraint vector  $\boldsymbol{\chi}_r$  can be computed by integrating all the equations of motion from  $\tilde{\mathbf{X}}_r$ , allowing for the updating of the design vector at the subsequent iteration as follows:

$$\tilde{\mathbf{X}}_{r+1} = \tilde{\mathbf{X}}_r - [\tilde{\mathbf{J}}(\boldsymbol{\chi}_r)]^{-1} \boldsymbol{\chi}_r. \quad (3.29)$$

If the number of variables exceeds the number of constraints ( $n > m$ ), the minimum norm update equation is employed instead of equation (3.29):

$$\tilde{\mathbf{X}}_{r+1} = \tilde{\mathbf{X}}_r - [\tilde{\mathbf{J}}(\boldsymbol{\chi}_r)]^T \left[ \tilde{\mathbf{J}}(\boldsymbol{\chi}_r) \tilde{\mathbf{J}}(\boldsymbol{\chi}_r)^T \right]^{-1} \boldsymbol{\chi}_r, \quad (3.30)$$

minimizing deviations and guiding the next solution to be as close as possible to the initial guess  $\tilde{\mathbf{X}}_r$ . In addition, to help the convergence of the iterative process by smoothing the corrections to be performed, a relaxation parameter  $\kappa_R$  is introduced in equations (3.29) and (3.30), obtaining

$$\tilde{\mathbf{X}}_{r+1} = \tilde{\mathbf{X}}_r - \kappa_R [\tilde{\mathbf{J}}(\boldsymbol{\chi}_r)]^{-1} \boldsymbol{\chi}_r, \quad \text{if } n = m, \quad (3.31a)$$

$$\tilde{\mathbf{X}}_{r+1} = \tilde{\mathbf{X}}_r - \kappa_R [\tilde{\mathbf{J}}(\boldsymbol{\chi}_r)]^T \left[ \tilde{\mathbf{J}}(\boldsymbol{\chi}_r) \tilde{\mathbf{J}}(\boldsymbol{\chi}_r)^T \right]^{-1} \boldsymbol{\chi}_r, \quad \text{if } n > m. \quad (3.31b)$$

Typical values for planar orbits, such as LOs, are  $\kappa_R \approx 0.5$ . For three-dimensional and more complex orbits, it is advisable to use a lower value to limit potential numerical complications.

### 3.4 Lyapunov Orbits Computation

The algorithm in the previous Section is now used to obtain the family of Lyapunov orbits (LOs) in the vicinity of EML2. These orbits are named after the Russian mathematician Aleksandr Mikhailovich Lyapunov, who made significant contributions to the theory of stability [40]. Within the CR3BP framework, the LOs are a type of periodic solution that exists in the plane of motion of the primaries (i.e., has no out-of-plane component  $\zeta$  and  $\dot{\zeta}$ ), namely  $\hat{\boldsymbol{\xi}}_S - \hat{\boldsymbol{\eta}}_S$  plane, and show symmetric properties with respect to the  $\hat{\boldsymbol{\xi}}_S - \hat{\boldsymbol{\zeta}}_S$  one. Such considerations lead to the requirement that when the LO crosses the  $\hat{\boldsymbol{\xi}}_S - \hat{\boldsymbol{\zeta}}_S$  plane, it should not have velocities along the  $\hat{\boldsymbol{\xi}}_S$  direction, i.e.  $\dot{\boldsymbol{\xi}}_0 = \dot{\boldsymbol{\xi}}_{\tau_f/2} = 0$ . Therefore, the constraint vector is

$$\boldsymbol{\chi}(\tilde{\mathbf{X}}_0^*) = \left\{ \begin{array}{c} \eta_f \\ \dot{\xi}_f \end{array} \right\} = \mathbf{0}. \quad (3.32)$$

Regarding the free-variable vector, in this case, it contains the starting position along the  $\hat{\boldsymbol{\xi}}_S$  axis, the initial velocity along the  $-\hat{\boldsymbol{\eta}}_S$  direction (for initial positions

$\xi_0 > \xi_{L_2}$ ) and, eventually, the integration time:

$$\tilde{\mathbf{X}}_0 = \begin{Bmatrix} \xi_0 \\ \dot{\eta}_0 \\ \tau \end{Bmatrix}. \quad (3.33)$$

The specific Jacobian matrix, necessary for the iterative process, is obtained by extracting the appropriate rows and columns from the complete one in (3.25), becoming

$$\tilde{\mathbf{J}} = \begin{bmatrix} \varphi_{21} & \varphi_{25} & \dot{\eta}_f \\ \varphi_{41} & \varphi_{45} & \dot{\xi}_f \end{bmatrix}, \quad (3.34)$$

where rows  $\{2, 4\}$  indeed correspond to  $\{\eta_f, \xi_f\}$  while columns  $\{1, 5, 7\}$  to  $\{\xi_0, \dot{\eta}_0, \tau\}$ .

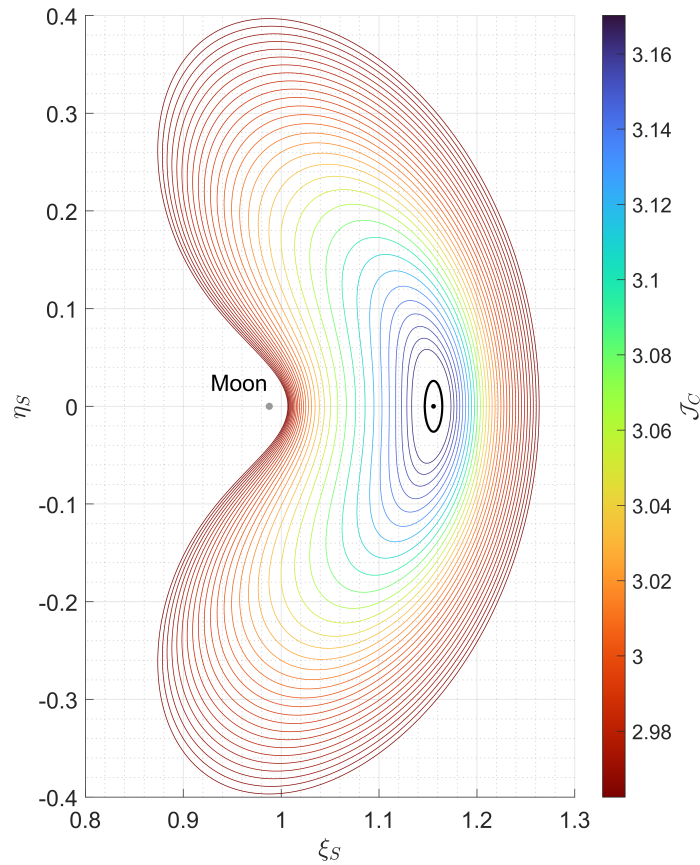


Fig. 3.1 Lyapunov Orbits family around EML<sub>2</sub>

Having all the ingredients available, a complete LOs family around EML<sub>2</sub> is computed by a continuation strategy: beginning with the computation of the analytical LO described by eqs. (3.10) with  $A_y = 1 \times 10^4$  km and represented in black in Figure 3.1, the initial position  $\xi_0$  is then incremented by a small finite step  $d\xi$  and is kept fixed throughout the DC process, permitting only variations in the initial velocity along the  $\hat{\eta}_S$  axis and the integration time  $\tau$ . The color bar located on the right in Figure 3.1 represents the values of the Jacobi Constant for the orbits depicted in the plot which exhibit decreasing values of the  $\mathcal{J}_C$  as they move further away from L2. This indicates that more energy is needed to navigate more complex trajectories, which increasingly take on more pronounced cashew-like shapes.

### 3.5 Near-Rectilinear Halo Orbits Computation

Halo Orbits (HOs) compose a family of three-dimensional periodic orbits that emerge from a pitchfork bifurcation of Lyapunov orbits in the CR3BP. As the amplitude of the planar Lyapunov orbits increases, a critical orbit is eventually reached, leading to a bifurcation. While the specific amplitude at which this bifurcation occurs cannot yet be predicted analytically, it can be identified by monitoring the eigenvalues of the monodromy matrix for each LO. These eigenvalues, or characteristic multipliers, are crucial for evaluating the stability of the solutions and identifying intersections with other families of orbits within the solution space [33, 41]. Such results derive from the analysis of periodic solutions of ODEs in Floquet theory, please refer to [42, 43] for a more comprehensive analysis.

The name *halo* refers to the shape and the way these orbits appear to hover or "halo" around the Lagrange points. Among the HOs, the Near-Rectilinear Halo Orbits (NRHOs) comprise a subset of the HOs family in the EM system, characterized by close lunar passages and possessing stability indices all within some small bound surrounding  $\pm 1$  and with no stability index that is significantly larger in magnitude than the others [44, 45]. The term *near-rectilinear* is due to their highly elongated, almost straight-line shape when viewed in a rotating RF.

The orbit chosen as the reference one for the de-orbiting trajectories to be optimized is the NRHO selected by NASA for the LOP-G, or more commonly known as Lunar Gateway. This specific orbit belongs to the southern family of the EML<sub>2</sub> NRHOs and presents a 9 : 2 lunar synodic resonance ( $S_R$ ). The ratio  $x : y$

reflects the number,  $x$ , of completed revolutions by a SC along its PO per  $y$  synodic cycles of the Moon, respectively. For example, the LOP-G in its 9 : 2 resonant NRHO will complete nine orbits over the span of two lunar months. The lunar  $S_R$  is an attractive characteristic for eclipse avoidance applications. By phasing the spacecraft within the NRHO such that perilune passages avoid alignment of the Sun and Earth, long eclipses by the Earth's shadow are avoided [44].

Being 3D orbits, the third dimension must be included both in design vector and in the constraint vector. Specifically, when the bifurcation occurs, the initial position acquires a positive or negative out-of-plane component  $\zeta_0$  for northern and southern HOs respectively; meanwhile, given that the orbit maintains its symmetry with respect to the  $\hat{\xi}_S - \hat{\zeta}_S$  plane, the out-of-plane velocity is constrained to be null. Hence, for the generic HO, the constraint vector is

$$\boldsymbol{\chi}(\tilde{\mathbf{X}}_0^*) = \begin{Bmatrix} \eta_f \\ \dot{\xi}_f \\ \dot{\zeta}_f \end{Bmatrix} = \mathbf{0}, \quad (3.35)$$

while the design vector becomes

$$\tilde{\mathbf{X}}_0 = \begin{Bmatrix} \xi_0 \\ \zeta_0 \\ \dot{\eta}_0 \\ \tau \end{Bmatrix}. \quad (3.36)$$

The case-specific Jacobian results a  $3 \times 4$  matrix, having added row 6 corresponding to  $\dot{\zeta}_f$  and column 3 corresponding to  $\zeta_0$  compared to LOs case in (3.34):

$$\tilde{\mathbf{J}} = \begin{bmatrix} \varphi_{21} & \varphi_{23} & \varphi_{25} & \dot{\eta} \\ \varphi_{41} & \varphi_{43} & \varphi_{45} & \dot{\xi} \\ \varphi_{61} & \varphi_{63} & \varphi_{65} & \dot{\zeta} \end{bmatrix}. \quad (3.37)$$

Starting from the initial LO that gives rise to the planar bifurcation [22, 33], to compute the southern EML<sub>2</sub> HOs family via continuation, in the initial phase where variations in  $-\hat{\zeta}_S$  direction prevail, the initial component  $\zeta_0$  is gradually incremented and kept fixed allowing the convergence with the other variables in the design vector. Then, in regions where  $\xi$  changes more rapidly than  $\zeta$ , it could be

more convenient to increase and fix  $\xi_0$  allowing the VTDC to find the corresponding other free variables.

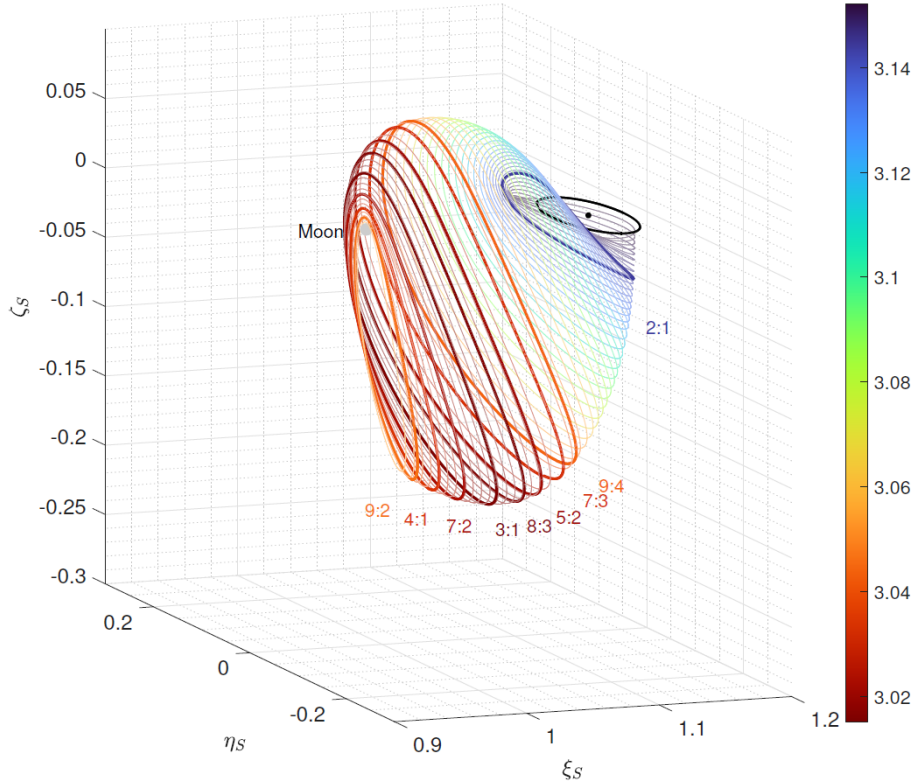


Fig. 3.2 Halo Orbits family around  $EML_2$  [22]

Some orbits with their lunar  $S_R$  values are highlighted in Figure 3.2. In this case, the Jacobi Constant no longer shows a monotonically decreasing trend, but decreases as the HOs evolve in their three-dimensional shape and reduce their perilune, reaching a minimum approximately at the NRHO with  $S_R = 3 : 1$  and then increases again.

As anticipated, the orbit of interest for this thesis work is the one with lunar synodic resonance of  $S_R = 9 : 2$ , depicted separately for clarity in Figure 3.3, whose initial state, coinciding with the apolune, results

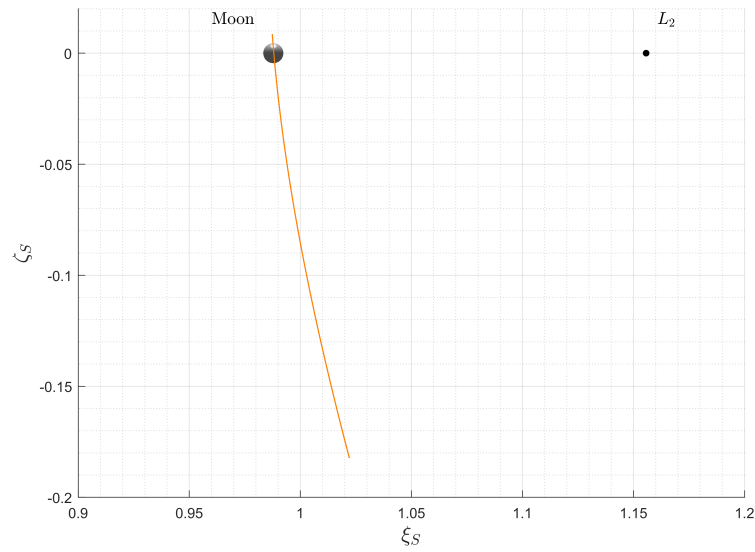
$$\tilde{\mathbf{X}}_0 = \{1.022028, 0.000000, -0.182101, 0.000000, -0.103271, 0.000000\}^T,$$

consistent with numerous references [13, 33, 46], with only minimal differences due to the non-dimensionalization process and numerical precision.

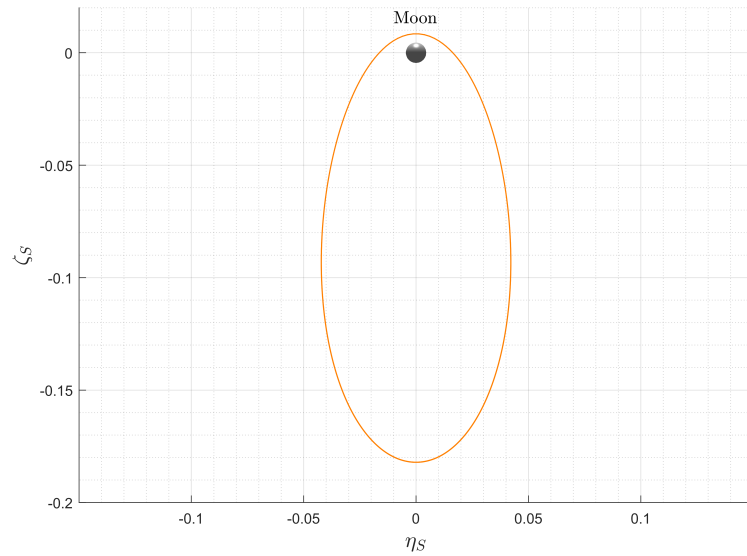
Given that the mean length of the Moon synodic month is  $\mathcal{T}_{syn} = 29.53059$  days [47], the orbit period in its dimensional and non-dimensional form is

$$\mathcal{T} = \frac{2}{9} \mathcal{T}_{syn} = 6.562353 \text{ days}, \quad \tau = \frac{\mathcal{T}}{\mathcal{T}^*} = 1.511199. \quad (3.38)$$

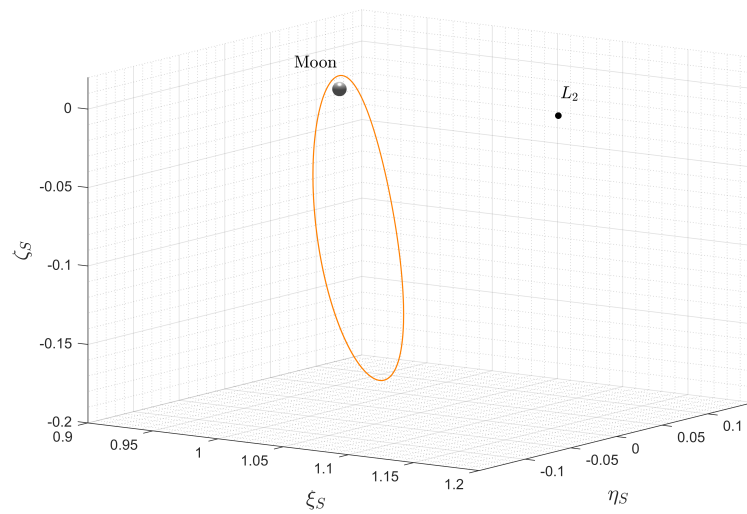
The 9 : 2 NRHO is the lowest-altitude one that demonstrates a useful resonance that accomplishes eclipse avoidance and is characterized by a perilune radius of about 3,300 km, and an apolune radius of approximately 70,000 km.



(a)  $\hat{\xi}_S - \hat{z}_S$  view



(b)  $\hat{\eta}_S - \hat{z}_S$  view



(c) 3D view

Fig. 3.3 Southern 9:2 synodic resonant EML<sub>2</sub> NRHO

It should be noted that if such trajectory is transitioned in a higher fidelity model, the concept of "periodicity" does not exist anymore, diverging from the expected behavior. Instead, such orbits are referred to as Quasi-Periodic Orbits (QPOs). However, as anticipated, the requirement for this thesis is to provide only the initial conditions of the injection points on the NRHO. Therefore, investigations into the long-term stability of the orbit and the transition to the NBP are not of interest and can be explored in the existing literature [22, 45, 48, 49].

# Chapter 4

## Optimal Control Theory

Optimal Control Theory (OCT) stands as a fundamental field within both engineering and mathematics, offering a rigorous framework for controlling complex systems in which infinite solutions are possible, given a desired task or behavior. At its core, OCT is concerned with finding a control law for a given system such that a certain optimality criterion is achieved. Whether it's minimizing the cost of transportation, reducing energy consumption, or optimizing the path of a spacecraft, OCT provides the tools to model and solve these problems with remarkable efficiency. Due to its versatility, this theory is applied across a wide spectrum of scenarios, from guiding aircraft via autopilot systems to shaping economic strategies with financial models, from chemistry to political science.

Its history is closely interlaced with the development of the *Calculus of Variations* (CoV), which itself began to take shape in the 17th century. The methods and principles of CoV are essential to understand and solve Optimal Control Problems (OCPs). The goal in the CoV is to find the function(s) that either minimize or maximize a given functional. This often involves determining the path, surface, or function that results in the least (or greatest) value of a certain integral. Pioneers like Johann Bernoulli, who posed the famous *Brachistochrone problem* in 1696, and Jakob Bernoulli, along with Euler and Lagrange in the 18th century, laid the foundational work [50]. While the CoV provides the mathematical bases for dealing with optimization problems involving functionals, OCT extends these concepts to dynamic systems where control over time is a central element. The formal development of OCT began in early 20th century, after Bellman's contribution to

Dynamic Programming and Pontryagin's Maximum Principle [51], another important optimality principle for control. The latter part of the 20th century and the early 21st century have seen OCT expand its reach thanks to computational advancements and increasing importance of computers.

In this thesis, the objective is to apply this theory in space trajectory optimization, a field that combines the elegance of mathematics with the real-world aspects of engineering, in order to showcase its ability to perform complex optimization problems. A foundational figure in this field is D. F. Lawden, who first approached a classical space engineering OCP with OCT in his pioneering work in 1963 [52], then extended by Lion and Handelsman [53].

Chapter 4 is therefore divided in six sections. The first section provides a swift overview of numerical methods for OCPs, focusing on direct and indirect approaches. The second and third sections introduce a general optimization problem and transform it into a Two-Point Boundary Value Problem (TPBVP) through Optimal Control Theory (OCT), outlining the pivotal results for the optimization process. In the fourth section, the problem is expanded into Multi-point Boundary Value Problems (MP-BVP) by introducing *arcs* and appropriately modifying the equations. The fifth section details the implementation of a BVP and illustrates the application of the single-shooting method for its iterative resolution. Finally, the last section applies OCT to the domain of spacecraft trajectory optimization within the CR3BP, which is the core subject of this thesis.

## 4.1 Numerical Methods for OCPs

At the heart of solving complex problems like OCPs lies the necessity for robust numerical methods capable of transforming the original infinite-dimensional optimization problem into one or more finite-dimensional sub-problems. Over the years, a broad array of methods has been developed to challenge the complex nature of OCPs, as documented in state of art literature [54–56]. The two types of numerical approach most widely used today are *direct* and *indirect* methods, stemming from two different philosophies.

On the one hand, the first class of direct methods is the most widely applied. It involves the discretization of the state and/or control of OCP, transcribing the prob-

lem to a *non-linear optimization problem*, or *non-linear programming problem* [54]. Therefore the trajectory is discretized, and state and control variables are typically approximated by piecewise constant parameterization or polynomial functions for each segment of trajectory. So the whole problem turns into a large-scale parameter optimization problem then solved by a non-linear software via Optimization Algorithms. The direct method's advantage lies in its ability to handle complex problems with non-linear dynamics and constraints, not requiring explicit derivation and construction of the necessary conditions, providing a powerful tool for designing efficient and optimal trajectories in various fields. However, the method's computational complexity can increase significantly with problem size, requiring careful selection of discretization strategies and optimization algorithms. Moreover, direct methods might encounter limitations in accuracy, and the numerical nature of the solution often does not provide theoretical insights into the actual optimality of the analytical approximation. Summing up in a few words, the direct approach is a "first discretize, then optimize" method [57].

On the other hand, through the application of OCT, indirect methods allows the transformation of an OCP into a BVP then discretized in time to obtain a numerical solution, thus solving the problem "indirectly". Hence, the optimal solution is determined by solving a system of differential equations that meets boundary and/or interior point conditions. Indirect methods differ from direct methods in handling the continuous forms of state and control variables. The primary unknowns are the initial costates, which must be determined to fulfill all specified boundary conditions and constraints (the process will be illustrated later). The appeal of the indirect approach lies in its small problem size, requiring fewer parameters to delineate a trajectory and generally demanding less computational time. As opposed to the first, this method is noted for its high precision and for providing theoretical hints steering users towards the optimal solution. However, it faces challenges with numerical stability because it is highly sensitive to the initial guess values. Additionally, managing potential discontinuities along the trajectory can present further complications, which can partly mitigated by splitting it in constrained and unconstrained sub-arcs. Hence, contrary to the former, the indirect approach is a "first optimize, then discretize" method [57].

The choice for the development of this thesis fell on an indirect method. Despite the challenges described earlier and further explored in Betts' work [54], this method demonstrates excellent potential in its application both in trajectory optimization

and beyond, as evidenced by the notable heritage represented by several articles and theses available in the literature [22, 31, 57–62].

## 4.2 General Statement

As previously mentioned, the objective of OCT is *to determine a control signals that will cause a process to satisfy the physical constraints and at the same time minimize (or maximize) some performance criterion* [63]. First, it is essential to model the dynamic problem (i.e. the trajectory) through a system of  $n$  Ordinary Differential Equations (ODEs) describing the evolution of  $n$  state variables over time. If  $\mathbf{x}(t) \in \mathbb{R}^n$  is the *state vector*, containing  $n$  state variables and  $\mathbf{u}(t) \in \mathbb{R}^m$  is the *control vector*, containing  $m$  control variables, i.e. inputs into a system that can be manipulated to influence the behavior of the state variables, then the ODE system can be generally formulated as

$$\dot{\mathbf{x}}(t) = \mathbf{f}(\mathbf{x}(t), \mathbf{u}(t), t), \quad (4.1)$$

being function of the state vector and the control vector over the interval from initial to final time. To determine the optimal trajectory, it must adhere to certain specific boundaries that can vary in nature; these might include constraints on the state variables at the external boundaries and, eventually, time constraints. To enable a more systematic incorporation of such Boundary Conditions (BCs) into the optimization process, it's worth to group them into a *constraint vector* and write them as a set of homogeneous (even non-linear) algebraic equations:

$$\boldsymbol{\chi}(\mathbf{x}_0, \mathbf{x}_f, t_0, t_f) = \mathbf{0}, \quad (4.2)$$

where  $\boldsymbol{\chi} : [\mathbb{R}^n, \mathbb{R}^n, \mathbb{R}, \mathbb{R}] \rightarrow \mathbb{R}^q$  collects the  $q$  imposed constraints. As will be detailed later, even the control vector  $\mathbf{u}$  can be subject to constraints as well (e.g. the limitation of thrust level at any time). Consequently, it must fall within the set of permissible controls denoted as  $\mathcal{U}$ .

Delving into the details of optimization, a merit index  $\mathcal{J}$  has to be extremized. In the *Bolza* form, it is defined as

$$\mathcal{J} = \varphi(\mathbf{x}_0, \mathbf{x}_f, t_0, t_f) + \int_{t_0}^{t_f} [\Phi(\mathbf{x}(t), \mathbf{u}(t), t)] dt. \quad (4.3)$$

The two terms that compose the equation (4.3) represent respectively the *terminal cost* and the *running cost* [64]. The first is a function evaluated at the extremal state and time of the process. This cost function is crucial when specific terminal conditions are desired. The second is a function that accumulates costs throughout the duration of the control process. It is usually expressed as an integral over time from the start to the end of the process. The function  $\Phi$  quantifies the "cost" of using a particular control  $\mathbf{u}(t)$  while in state  $\mathbf{x}(t)$  at time  $t$ . The decision to set either the running cost or the terminal cost to zero, along with the introduction of auxiliary variables, leads to two distinct formulations: the *Mayer formulation* and the *Lagrange formulation*. The first is often preferred for certain problems because of the simplicity it offers in both the problem formulation and the analytical derivation of the first order necessary conditions which, as can be seen later, are crucial for determining optimal controls.

### 4.3 Implementing the Indirect Method

The ongoing discussion shift towards the application of the IM's principles which OCT is based on. The derivation of the optimality condition begins by defining an augmented merit index,  $\mathcal{J}^*$ , which incorporates a measure of the adherence to constraints and state quantities in relation to the ODEs governing the dynamical model. It requires the introduction of further two mathematical tools: the *Lagrange multipliers*  $\boldsymbol{\mu} \in \mathbb{R}^m$  (related to boundary conditions) and the *adjoint vector*  $\boldsymbol{\lambda}(t) \in \mathbb{R}^n$ , containing the adjoint (or co-state) variables (linked to the state variables). Hence, the augmented merit index can be formulated as

$$\mathcal{J}^* = \varphi + \boldsymbol{\mu}^T \boldsymbol{\chi} + \int_{t_0}^{t_f} [\Phi + \boldsymbol{\lambda}^T (\mathbf{f} - \dot{\mathbf{x}})] dt, \quad (4.4)$$

that is, exactly like  $\mathcal{J}$ , function of  $t$ ,  $\mathbf{x}$ ,  $\dot{\mathbf{x}}$  and  $\mathbf{u}$ .

It's apparent that when both the BCs, specified as  $\boldsymbol{\chi} = \mathbf{0}$ , and the state equations, denoted by  $\dot{\mathbf{x}} = \mathbf{f}$ , are fulfilled, there's a direct equivalence between solving the problem with the functional  $\mathcal{J}$  or with its augmented counterpart  $\mathcal{J}^*$ . To eliminate the dependency on the time derivatives of the state variables, an integration by parts is performed on the term  $-\boldsymbol{\lambda}^T \dot{\mathbf{x}}$  at this point:

$$\int_{t_0}^{t_f} (-\boldsymbol{\lambda}^T \dot{\mathbf{x}}) dt = -(\boldsymbol{\lambda}_f^T \mathbf{x}_f) + (\boldsymbol{\lambda}_0^T \mathbf{x}_0) + \int_{t_0}^{t_f} (\dot{\boldsymbol{\lambda}}^T \mathbf{x}) dt. \quad (4.5)$$

Substituting the equation (4.5) into (4.4) the augmented merit index becomes:

$$\mathcal{J}^* = \varphi + \boldsymbol{\mu}^T \boldsymbol{\chi} + (\boldsymbol{\lambda}_0^T \mathbf{x}_0 - \boldsymbol{\lambda}_f^T \mathbf{x}_f) + \int_{t_0}^{t_f} (\Phi + \boldsymbol{\lambda}^T \mathbf{f} + \dot{\boldsymbol{\lambda}}^T \mathbf{x}) dt, \quad (4.6)$$

in which a key function appears, the system's *Hamiltonian*  $\mathcal{H}$ :

$$\mathcal{H} \triangleq \Phi + \boldsymbol{\lambda}^T \mathbf{f}. \quad (4.7)$$

The fundamental condition that guarantee the solution's optimality is the stationarity of  $\mathcal{J}^*$ . In other words, at the optimal solution, the augmented merit index reaches a stationary value, indicating that a local extremum (either a minimum or a maximum, depending on the problem formulation) has been achieved. This condition implies that its first order variation must be equal to zero, therefore equation (4.6) must be differentiate as follows:

$$\delta \mathcal{J}^* = \left( \frac{\partial \varphi}{\partial t_0} + \boldsymbol{\mu}^T \frac{\partial \boldsymbol{\chi}}{\partial t_0} - \mathcal{H}_0 \right) \delta t_0 + \quad (4.8a)$$

$$+ \left( \frac{\partial \varphi}{\partial t_f} + \boldsymbol{\mu}^T \frac{\partial \boldsymbol{\chi}}{\partial t_f} + \mathcal{H}_f \right) \delta t_f + \quad (4.8b)$$

$$+ \left( \frac{\partial \varphi}{\partial \mathbf{x}_0} + \boldsymbol{\mu}^T \frac{\partial \boldsymbol{\chi}}{\partial \mathbf{x}_0} + \boldsymbol{\lambda}_0^T \right) \delta \mathbf{x}_0 + \quad (4.8c)$$

$$+ \left( \frac{\partial \varphi}{\partial \mathbf{x}_f} + \boldsymbol{\mu}^T \frac{\partial \boldsymbol{\chi}}{\partial \mathbf{x}_f} - \boldsymbol{\lambda}_f^T \right) \delta \mathbf{x}_f + \quad (4.8d)$$

$$+ \int_{t_0}^{t_f} \left[ \left( \frac{\partial \mathcal{H}}{\partial \mathbf{x}} + \dot{\boldsymbol{\lambda}}^T \right) \delta \mathbf{x} + \frac{\partial \mathcal{H}}{\partial \mathbf{u}} \delta \mathbf{u} \right] dt. \quad (4.8e)$$

A proper selection of the adjoint variables  $\boldsymbol{\lambda}$  and Lagrange multipliers  $\boldsymbol{\mu}$  can effectively nullify  $\delta\mathcal{J}^*$  for any variation in  $\delta t_0$ ,  $\delta t_f$ ,  $\delta \mathbf{x}_0$ ,  $\delta \mathbf{x}_f$ ,  $\delta \mathbf{x}$  and  $\delta \mathbf{u}$ . This is achieved by ensuring that the coefficients multiplying these variations are themselves zero, thus satisfying the necessary condition for optimality by negating any potential change in the augmented functional. From this, different sets of conditions must be extrapolated, each linked to a specific term in the equations (4.8):

- *transversality conditions*: 2 algebraic equations (at  $t_0$  and  $t_f$ ) obtained from (4.8a) and (4.8b) by setting the two bracketed coefficients to zero;
- *optimality conditions*:  $2n$  algebraic equations provided by zeroing out the multiplying terms in (4.8c) and (4.8d), one per each state variable at both starting and ending boundaries;
- *Euler-Lagrange Equations*:  $n$  ODEs for the adjoint variables, retrieved by nullifying the coefficient of  $\delta \mathbf{x}$  in (4.8e);
- *equations for controls*:  $m$  algebraic equations for the control variables, retrieved by nullifying the coefficient of  $\delta \mathbf{u}$  in (4.8e).

### 4.3.1 Boundary Conditions for Optimality

The boundary conditions for optimality consist of a set of ODEs that govern how times and states should be configured at the boundaries of the optimal trajectory. Specifically, there are two transversality conditions for the times and  $2n$  optimality conditions for the states. As specified before, these conditions derive from nullifying the multiplying coefficients of variations, resulting

$$\frac{\partial \varphi}{\partial t_0} + \boldsymbol{\mu}^T \frac{\partial \boldsymbol{\chi}}{\partial t_0} - \mathcal{H}_0 = 0 \quad (4.9a)$$

$$\frac{\partial \varphi}{\partial t_f} + \boldsymbol{\mu}^T \frac{\partial \boldsymbol{\chi}}{\partial t_f} + \mathcal{H}_f = 0 \quad (4.9b)$$

$$\frac{\partial \varphi}{\partial \mathbf{x}_0} + \boldsymbol{\mu}^T \frac{\partial \boldsymbol{\chi}}{\partial \mathbf{x}_0} + \boldsymbol{\lambda}_0^T = \mathbf{0} \quad (4.9c)$$

$$\frac{\partial \varphi}{\partial \mathbf{x}_f} + \boldsymbol{\mu}^T \frac{\partial \boldsymbol{\chi}}{\partial \mathbf{x}_f} - \boldsymbol{\lambda}_f^T = \mathbf{0}. \quad (4.9d)$$

From the aforementioned equations arise some handy and pragmatic rules. Observing eqs. (4.9a) and (4.9b), it becomes apparent that if the initial time  $t_0$  (and/or final time  $t_f$ ) is not explicitly included in either the boundary conditions  $\boldsymbol{\chi}$  or the function  $\varphi$ , then the Hamiltonian is zero at the initial time (and/or at the final time) and the values for  $t_0$  and  $t_f$  depend on the optimization. Otherwise, if the time is constrained, i.e. appears in  $\boldsymbol{\chi}$ , then the corresponding Hamiltonian is free and depends on the optimization.

Analogously, as regards state variables and corresponding adjoint variables, eqs. (4.9c) and (4.9d) state that if the generic  $i$ -th  $x_i$  is neither constrained nor present in  $\varphi$ , as a result the matching  $\lambda_i$  is null at the same point. Vice versa, the  $i$ -th adjoint variable is free if the respective state variable is bound.

### 4.3.2 Euler-Lagrange and Control Variables Equations

The temporal evolution of the adjoint variables and controls can be derived by setting the coefficients preceding  $\delta\boldsymbol{x}$  and  $\delta\boldsymbol{u}$  in eq. (4.8e) to zero, obtaining respectively  $n$  Euler-Lagrange Equations

$$\frac{d\boldsymbol{\lambda}}{dt} = - \left( \frac{\partial \mathcal{H}}{\partial \boldsymbol{x}} \right)^T, \quad (4.10)$$

and  $m$  algebraic equations for the controls

$$\left( \frac{\partial \mathcal{H}}{\partial \boldsymbol{u}} \right)^T = 0. \quad (4.11)$$

As anticipated before, elements of control vector  $\boldsymbol{u}$  can be subject to constraints. When explicit admissibility constraints (e.g.  $\mathcal{U}_{min} \leq u \leq \mathcal{U}_{max}$ ) are involved, the eq. (4.11) might not yield the optimal controls. Searching for a solution that necessitates a control  $u$  beyond these constraints would be impractical. At this point it is useful to introduce the Pontryagin's Maximum Principle PMP (or Pontryagin's minimum Problem PmP if the problem requires a minimization), which states that the optimal control value in any point of the trajectory is the one that belongs to the admissibility domain and maximize (if  $\mathcal{J}$  has to be maximized) or minimize (in the opposite case) the Hamiltonian in that point. Hence:

- if eq. (4.11) gives  $u_j$  compliant with the admissible region, no control constraint is needed;

- if the resulting  $u_j$  is outside of the admissible region, the control is set to its extremal allowed value (i.e.  $u_j = \mathcal{U}_{j,max}$  or  $u_j = \mathcal{U}_{j,min}$ ).

A particular situation emerges when the Hamiltonian exhibits linear dependence within the bounded control. Under such conditions, one has

$$\frac{\partial \mathcal{H}}{\partial u_j} = k_{u_j}, \quad (4.12)$$

in which  $k_{u_j}$  is a constant. The fulfillment of eq. (4.11) is only conditional if the above constant is exactly zero, since the control disappears with the derivative. In the case of linear dependency between  $\mathcal{H}$  and  $u_j$ , the strategy implemented is known as *bang-bang* control, depending on the value assumed by the constant  $k_{u_j}$ :

- if  $k_{u_j} < 0 \implies u_j = \mathcal{U}_{j,min}$ . This means that  $\mathcal{H}$  is maximized if the control is set to its minimum admissible value;
- if  $k_{u_j} > 0 \implies u_j = \mathcal{U}_{j,max}$ . Giving the control its maximum admissible value, the maximization of  $\mathcal{H}$  is ensured.

In cases where  $k_{u_j} = 0$ , other strategies must be employed since this pertains to *singular arcs*, a situation that does not occur in the case study and therefore omitted.

## 4.4 Multi-Point Optimal Control Problem

What has been described so far relates to a Two-Point Boundary Value Problem (TPBVP), in which the trajectory is defined by initial and final conditions making the problem clearer to describe. However, the choice is often made to divide the trajectory into  $n_p$  sub-intervals (*phases* or *arcs*), thus transitioning to a Multi-Point Boundary Value Problem (MPBVP). By segmenting the problem, one can apply more tailored control strategies to each phase, potentially simplifying the computational process and enhancing the effectiveness of the overall control solution.

It is possible to outline the subdivision as follows:  $j$ -th arc begins just after the point  $t_{(j-1)+}$  and ends just before the point  $t_{j-}$ . Correspondingly, the state variable vectors at these points are represented as  $\mathbf{x}_{(j-1)+}$  and  $\mathbf{x}_{j-}$ . The subscripts - and + are used to indicate values assumed immediately before and after a specific point,

respectively. This schematization facilitates the handling of possible discontinuities in the state variables or in the timing and also accommodates internal constraints that may occur at the junction points between each contiguous arc, referred to as *internal* boundaries. The duration of each  $j$ -th arc,  $\Delta t_j$ , when unknown, is generally subject to optimization and can vary among the phases to adapt to different dynamic conditions and requirements. For this kind of problem, the constraint vector seen in (4.2) becomes

$$\boldsymbol{\chi}(\mathbf{x}_{(j-1)+}, \mathbf{x}_{j-}, t_{(j-1)+}, t_{j-}) = \mathbf{0}, \quad j = 1, \dots, n_p, \quad (4.13)$$

involving BCs at both internal and external boundaries.

In the same way, the generic form of the merit index introduced in eq. (4.3) can be written as:

$$\mathcal{J} = \varphi(\mathbf{x}_{(j-1)+}, \mathbf{x}_{j-}, t_{(j-1)+}, t_{j-}) + \sum_{j=1}^{n_p} \int_{t_{(j-1)+}}^{t_{j-}} [\Phi(\mathbf{x}(t), \mathbf{u}(t), t)] dt. \quad (4.14)$$

This time,  $\varphi$  depends on the values of variables and times at every boundary for each arc,  $\Phi$  serves the same task as before but taking into account how the solution progresses through the arcs.

The generic form of the augmented merit index has the form

$$\mathcal{J}^* = \varphi + \boldsymbol{\mu}^T \boldsymbol{\chi} + \sum_{j=1}^{n_p} \int_{t_{(j-1)+}}^{t_{j-}} [\Phi + \boldsymbol{\lambda}^T (\mathbf{f} - \dot{\mathbf{x}})] dt. \quad (4.15)$$

Following the same mathematical steps previously, i.e. integrating by parts and substituting, one obtains

$$\mathcal{J}^* = \varphi + \boldsymbol{\mu}^T \boldsymbol{\chi} + \sum_{j=1}^{n_p} [\boldsymbol{\lambda}_{(j-1)+}^T \mathbf{x}_{(j-1)+} - \boldsymbol{\lambda}_{j-}^T \mathbf{x}_{j-}] + \sum_{j=1}^{n_p} \int_{t_{(j-1)+}}^{t_{j-}} [\Phi + \boldsymbol{\lambda}^T \mathbf{f} + \dot{\boldsymbol{\lambda}}^T \mathbf{x}] dt. \quad (4.16)$$

By differentiating the eq. (4.16),  $\delta\mathcal{J}^*$  per each arc results

$$\delta\mathcal{J}^* = \left( \frac{\partial\varphi}{\partial t_{(j-1)_+}} + \boldsymbol{\mu}^T \frac{\partial\boldsymbol{\chi}}{\partial t_{(j-1)_+}} - \mathcal{H}_{(j-1)_+} \right) \delta t_{(j-1)_+} + \quad (4.17a)$$

$$+ \left( \frac{\partial\varphi}{\partial t_{j_-}} + \boldsymbol{\mu}^T \frac{\partial\boldsymbol{\chi}}{\partial t_{j_-}} + \mathcal{H}_{j_-} \right) \delta t_{j_-} + \quad (4.17b)$$

$$+ \left( \frac{\partial\varphi}{\partial \mathbf{x}_{(j-1)_+}} + \boldsymbol{\mu}^T \frac{\partial\boldsymbol{\chi}}{\partial \mathbf{x}_{(j-1)_+}} + \boldsymbol{\lambda}_{(j-1)_+}^T \right) \delta \mathbf{x}_{(j-1)_+} + \quad (4.17c)$$

$$+ \left( \frac{\partial\varphi}{\partial \mathbf{x}_{j_-}} + \boldsymbol{\mu}^T \frac{\partial\boldsymbol{\chi}}{\partial \mathbf{x}_{j_-}} - \boldsymbol{\lambda}_{j_-}^T \right) \delta \mathbf{x}_{j_-} + \quad (4.17d)$$

$$+ \sum_{j=1}^{n_p} \int_{t_{(j-1)_+}}^{t_{j_-}} \left[ \left( \frac{\partial\mathcal{H}}{\partial \mathbf{x}} + \dot{\boldsymbol{\lambda}}^T \right) \delta \mathbf{x} + \frac{\partial\mathcal{H}}{\partial \mathbf{u}} \delta \mathbf{u} \right] dt, \quad j = 1, \dots, n_p \quad (4.17e)$$

Considering a MPBVP, the aforementioned optimality and transversality conditions are more effectively expressed in relation to the  $j$ -th boundary itself. Hence, introducing subscripts  $j_-$  and  $j_+$  (standing for positions immediately before and after the  $j$ -th, respectively), the equations retrieved in Section 4.3.1 can be written as

$$\frac{\partial\varphi}{\partial t_{j_+}} + \boldsymbol{\mu}^T \frac{\partial\boldsymbol{\chi}}{\partial t_{j_+}} - \mathcal{H}_{j_+} = 0, \quad j = 0, \dots, n_p - 1 \quad (4.18a)$$

$$\frac{\partial\varphi}{\partial t_{j_-}} + \boldsymbol{\mu}^T \frac{\partial\boldsymbol{\chi}}{\partial t_{j_-}} + \mathcal{H}_{j_-} = 0, \quad j = 1, \dots, n_p \quad (4.18b)$$

$$\frac{\partial\varphi}{\partial \mathbf{x}_{j_+}} + \boldsymbol{\mu}^T \frac{\partial\boldsymbol{\chi}}{\partial \mathbf{x}_{j_+}} + \boldsymbol{\lambda}_{j_+}^T = \mathbf{0}, \quad j = 0, \dots, n_p - 1 \quad (4.18c)$$

$$\frac{\partial\varphi}{\partial \mathbf{x}_{j_-}} + \boldsymbol{\mu}^T \frac{\partial\boldsymbol{\chi}}{\partial \mathbf{x}_{j_-}} - \boldsymbol{\lambda}_{j_-}^T = \mathbf{0}, \quad j = 1, \dots, n_p. \quad (4.18d)$$

Meanwhile, the points discussed in Section 4.3.2 still hold for a MPBVP.

## 4.5 Boundary Value Problem Implementation

This section delves into the methods and challenges involved in implementing a Boundary Value Problem (BVP), highlighting the adjustments required to address the complexities introduced by OCT. Its application to dynamic systems typically results in the formulation of a TPBVP (or MPBVP if there is subdivision in arcs).

This transformation is a fundamental aspect of OCT, where the original BVP is converted into an augmented version with new potential unknowns, resulting in a more dimensionally complex problem. However, this approach allows for the imposition of the conditions previously derived that ensure the optimality of the solution.

Let  $\mathbf{y}(t)$  be the vector composed by state and adjoint variables, function of time:

$$\mathbf{y}(t) = \{\mathbf{x}(t)^T, \boldsymbol{\lambda}(t)^T\}^T. \quad (4.19)$$

The main purpose is to find the optimal initial state vector  $\mathbf{y}_0^* = \{\mathbf{x}_0^{*T}, \boldsymbol{\lambda}_0^{*T}\}^T$  which, fulfilling all imposed and optimality BCs, leads to the desired final state  $\mathbf{y}_f^*$ . A single-shooting numerical method via Differential Correction (DC) is chosen, capable of updating initial state at each step depending on the final condition reached, with the aim to limit undesired terminal deviation (refer to Section 3.3).

An exploration of the shooting method for the solution of a TPBVP is undertaken with reference to a generic system

$$\dot{\mathbf{y}} = \mathbf{f}(\mathbf{y}(t), t). \quad (4.20)$$

Since this type of problem may also depend on some constant value, gathered in the vector  $\mathbf{c}$ , it is appropriate to define a new vector  $\mathbf{z}(t) = \{\mathbf{y}(t)^T, \mathbf{c}^T\}^T$ . Therefore, the set of ODEs in its general form is

$$\dot{\mathbf{z}} = \frac{d\mathbf{z}}{dt} = \mathbf{f}(\mathbf{z}(t), t), \quad (4.21)$$

being

$$\dot{\mathbf{c}} = \frac{d\mathbf{c}}{dt} = \mathbf{0}, \quad (4.22)$$

while the set of BCs and BCs for optimality can be written as

$$\boldsymbol{\chi}(\mathbf{z}) = \mathbf{0}. \quad (4.23)$$

Note that the notation  $(t)$  is omitted henceforth.

In analogy to the approach taken for orbit construction in Chapter 3, the objective now is to implement the single-shooting method combined with the DC procedure to

find the optimal initial state  $\mathbf{z}_0^*$  that leads to the desired final state while satisfying BCs  $\boldsymbol{\chi}(\mathbf{z}) = \mathbf{0}$ .

Assuming none of the initial values is known, the first iteration is started by integrating the set of equations (4.20) with a guess initial vector  $\mathbf{q}_r = \mathbf{z}_0$  and then the process is carried on iteratively. This results at each  $r$ -th iteration in the computation of the error on BCs. With a first order Taylor expansion, one can express the BCs at the  $(r+1)$ -th iteration as a function of the BCs and the state vector at the previous  $r$ -th one:

$$\boldsymbol{\chi}(\mathbf{q}_{r+1}) = \boldsymbol{\chi}(\mathbf{q}_r) + \frac{\partial \boldsymbol{\chi}(\mathbf{q}_r)}{\partial \mathbf{q}_{r+1}} (\mathbf{q}_{r+1} - \mathbf{q}_r). \quad (4.24)$$

The term containing the partial derivatives represents the Jacobian matrix  $\mathbf{J}$ , which provides both quantitative and qualitative insights into how small changes in  $\mathbf{q}_r$  impact on the problem.

To simplify the notation two abbreviations are introduced:

$$\boldsymbol{\chi}_r \triangleq \boldsymbol{\chi}(\mathbf{q}_r), \quad (4.25a)$$

$$\mathbf{J}(\boldsymbol{\chi}_r) \triangleq \mathbf{J}(\boldsymbol{\chi}(\mathbf{q}_r), \mathbf{q}_{r+1}). \quad (4.25b)$$

As it is defined, if a solution exists, leads to  $\boldsymbol{\chi}_{r+1} = \mathbf{0}$  and consequently to the following iterative solution form:

$$\boldsymbol{\chi}_r + [\mathbf{J}(\boldsymbol{\chi}_r)] (\mathbf{q}_{r+1} - \mathbf{q}_r) = \mathbf{0}. \quad (4.26)$$

Therefore, from the above equation, the state of the updated design vector can be computed, at each iteration, as follows:

$$\mathbf{q}_{r+1} = \mathbf{q}_r - [\mathbf{J}(\boldsymbol{\chi}_r)]^{-1} \boldsymbol{\chi}_r \quad (4.27)$$

and used for the following iteration, allowing the updating of values of the constraint vector until the wanted precision on the error norm is reached.

In the present work, the calculation of the Jacobian is approximated by means of forward finite-differences method. Perturbing each variable element of  $\mathbf{q}_r$  by a certain  $\Delta$ ,

$$q_{i_r}^p = q_{i_r} + \Delta, \quad (4.28)$$

and integrating with the perturbed initial condition, the Jacobian matrix is obtained as

$$\mathbf{J}(\boldsymbol{\chi}_r) = \frac{\boldsymbol{\chi}_r^p - \boldsymbol{\chi}_r}{\mathbf{q}_r^p - \mathbf{q}_r} = \frac{\boldsymbol{\chi}_r^p - \boldsymbol{\chi}_r}{\Delta}, \quad (4.29)$$

where the superscript  $p$  stands for *perturbed* and  $\boldsymbol{\chi}_r^p \triangleq \boldsymbol{\chi}(\mathbf{q}_r^p)$ .

Even though it involves an approximate calculation, this choice is made with the aim of considering analyses with different constraints and BCs, thereby making the code much faster and more versatile. Indeed, the Jacobian matrix should be exactly computed with respect to the examined problem, introducing a new STM matrix for linear mapping whose evolution would need to be tracked by an additional set of ODEs, making the calculation process more cumbersome.

Finally, all the tools are available to solve the TPBVP introduced so far, governed by the set of ODEs

$$\dot{\mathbf{z}} = \mathbf{f}(\mathbf{z}(t), t), \quad (4.30)$$

to be integrated iteratively in order to find the optimal initial state  $\mathbf{z}_0^*$  which allows the trajectory to lead to the desired final state  $\mathbf{z}_f^*$  while respecting the imposed constraints  $\chi$ . Such integration is performed in Python environment via the LSODA function pre-compiled in C++ [65], implementing an implicit multistep numerical method based on the Adams-Moulton formulations with variable step size and order [66]. Using a Python integrator precompiled in C++ offers significant advantages such as improved performance and computational efficiency, due to C++'s faster execution for intensive numerical operations due to machine-level compilation, while still maintaining Python's highly flexible and simple working environment.

The Jacobian computation within the iterative Differential Correction (DC) process may introduce inaccuracies that potentially threaten the method's convergence, leading to divergences. To refine the process certain strategies are incorporated. One such strategy is the application of a correction factor during the update step of the iterative process:

$$\mathbf{z}_{r+1} = \mathbf{z}_r - \kappa_1 \cdot [\mathbf{J}(\boldsymbol{\chi}_r)]^{-1} \boldsymbol{\chi}_r, \quad (4.31)$$

where appropriate values of the relaxation factor  $\kappa_1 = 1 \times 10^{-3} \div 1 \times 10^{-5}$  are beneficial to guarantee the convergence. In the initial stages of the iterative process, when the unknown values are being approximated with rough guesses, it is prudent to use lower values for  $k_1$ . As the solution begins to approach the vicinity of the optimal

value, higher values of can be employed depending on how sensitive the problem is. Another strategy involves the control on the subsequent error with respect to the error indicated by  $\boldsymbol{\chi}$  at the previous step:

$$E_{max,r+1} < \kappa_2 E_{max,r}, \quad (4.32)$$

where  $E_{max} = \max(\chi_i)$  and a value of  $\kappa_2 = 2 \div 3$  proves to be effective in supporting the initial phase of the iterative process. This approach can encourage convergence despite a possible initial increase in the maximum error, as it helps to establish the appropriate direction towards optimality within the search space. If the equation (4.32) is not satisfied,  $k_1$  is subject to a bisection method, which may be applied up to five iterations to refine the solution.

## 4.6 OCT in CR3BP Trajectory Optimization

In light of the dynamic model employed, the spacecraft dynamics equations in non-dimensional form, considering low-thrust propulsion, are more conveniently described by the following set of ODEs [67, 68]:

$$\frac{d\boldsymbol{\rho}}{dt} = \boldsymbol{\nu} \quad (4.33a)$$

$$\frac{d\boldsymbol{\nu}}{dt} = \boldsymbol{g}(\boldsymbol{\rho}) + \boldsymbol{h}(\boldsymbol{\nu}) + \frac{\boldsymbol{T}}{m} \quad (4.33b)$$

$$\frac{dm}{dt} = -\frac{T}{c}, \quad (4.33c)$$

where

$$\boldsymbol{\rho} = \{\xi, \eta, \zeta\}^T, \quad \boldsymbol{\nu} = \{\dot{\xi}, \dot{\eta}, \dot{\zeta}\}^T,$$

while the equation (4.33c) represents the mass consumption of the propulsion system, depending on the effective exhaust velocity  $c = I_{sp}g_0$ . The functions  $\boldsymbol{g}(\boldsymbol{\rho})$  and  $\boldsymbol{h}(\boldsymbol{\nu})$

are introduced to compact the equations (2.24) and are defined respectively as

$$\mathbf{g}(\boldsymbol{\rho}) = \begin{Bmatrix} \xi - \frac{1-\mu}{\rho_{13}^3}(\xi + \mu) - \frac{\mu}{\rho_{23}^3}[\xi - (1-\mu)] \\ \eta - \frac{1-\mu}{\rho_{13}^3}\eta - \frac{\mu}{\rho_{23}^3}\eta \\ -\frac{1-\mu}{\rho_{13}^3}\zeta - \frac{\mu}{\rho_{23}^3}\zeta \end{Bmatrix},$$

$$\mathbf{h}(\mathcal{V}) = \begin{Bmatrix} 2\dot{\eta} \\ -2\dot{\xi} \\ 0 \end{Bmatrix}. \quad (4.34)$$

Note that the spacecraft mass  $m$  and the thrust magnitude  $T$  are non-dimensionalized by using the initial spacecraft mass  $m_0$ .

The application of the OCT to the above system aims at finding the optimal control law, specifically the thrust vector  $\mathbf{T}$ , that maximize the final mass of the SC at the end of the trajectory. The state vector  $\mathbf{x}(t) \in \mathbb{R}^n$  has the form

$$\mathbf{x} = \left\{ \xi, \eta, \zeta, \dot{\xi}, \dot{\eta}, \dot{\zeta}, m \right\}^T \quad (4.35)$$

and introducing for each variable the corresponding adjoint one, the augmented state vector  $\mathbf{y}(t) \in \mathbb{R}^{2n}$  is obtained:

$$\mathbf{y} = \left\{ \xi, \eta, \zeta, \dot{\xi}, \dot{\eta}, \dot{\zeta}, m, \lambda_\xi, \lambda_\eta, \lambda_\zeta, \lambda_{\dot{\xi}}, \lambda_{\dot{\eta}}, \lambda_{\dot{\zeta}}, \lambda_m \right\}^T. \quad (4.36)$$

For this type of problem, the Mayer formulation is preferred. Being  $\Phi = 0$ , the merit index  $\mathcal{J}$  to be maximized coincide with the value of SC mass at the end of the trajectory:

$$\mathcal{J} = \varphi = m_f. \quad (4.37)$$

By expressing positions and velocities component by component and explaining  $\mathbf{g}(\boldsymbol{\rho})$  and  $\mathbf{h}(\mathbf{V})$ , the system of ODEs in eqs. (4.33) becomes

$$\frac{d\xi}{dt} = \dot{\xi} \quad (4.38a)$$

$$\frac{d\eta}{dt} = \dot{\eta} \quad (4.38b)$$

$$\frac{d\zeta}{dt} = \dot{\zeta} \quad (4.38c)$$

$$\frac{d\dot{\xi}}{dt} = 2\dot{\eta} + \xi - \frac{1-\mu}{\rho_{13}^3}(\xi + \mu) - \frac{\mu}{\rho_{23}^3}[\xi - (1-\mu)] + \frac{T_\xi}{m} \quad (4.38d)$$

$$\frac{d\dot{\eta}}{dt} = -2\dot{\xi} + \eta - \frac{1-\mu}{\rho_{13}^3}\eta - \frac{\mu}{\rho_{23}^3}\eta + \frac{T_\eta}{m} \quad (4.38e)$$

$$\frac{d\dot{\zeta}}{dt} = -\frac{1-\mu}{\rho_{13}^3}\zeta - \frac{\mu}{\rho_{23}^3}\zeta + \frac{T_\zeta}{m} \quad (4.38f)$$

$$\frac{dm}{dt} = -\frac{T}{c}. \quad (4.38g)$$

Therefore, the Hamiltonian defined in eq. (4.7) turns into

$$\begin{aligned} \mathcal{H} = \boldsymbol{\lambda}^T \mathbf{f} &= \sum_{i=1}^{2n} \lambda_i f_i = \lambda_\xi \dot{\xi} + \lambda_\eta \dot{\eta} + \lambda_\zeta \dot{\zeta} + \\ &+ \lambda_\xi \left[ 2\dot{\eta} + \xi - \frac{1-\mu}{\rho_{13}^3}(\xi + \mu) - \frac{\mu}{\rho_{23}^3}(\xi - 1 + \mu) + \frac{T_\xi}{m} \right] + \\ &+ \lambda_\eta \left[ -2\dot{\xi} + \eta - \frac{1-\mu}{\rho_{13}^3}\eta - \frac{\mu}{\rho_{23}^3}\eta + \frac{T_\eta}{m} \right] + \\ &+ \lambda_\zeta \left[ -\frac{1-\mu}{\rho_{13}^3}\zeta - \frac{\mu}{\rho_{23}^3}\zeta + \frac{T_\zeta}{m} \right] + \\ &- \lambda_m \frac{T}{c}, \end{aligned} \quad (4.39)$$

or in compact form

$$\mathcal{H} = \boldsymbol{\lambda}_\rho^T \boldsymbol{\nu} + \boldsymbol{\lambda}_V^T \left[ \mathbf{g}(\boldsymbol{\rho}) + \mathbf{h}(\mathbf{V}) + \frac{\mathbf{T}}{m} \right] - \lambda_m \frac{T}{c}, \quad (4.40)$$

where:

- the vector  $\boldsymbol{\lambda}_\rho$  includes the three adjoint variables of the three synodic coordinates, namely

$$\boldsymbol{\lambda}_\rho = \begin{Bmatrix} \lambda_\xi \\ \lambda_\eta \\ \lambda_\zeta \end{Bmatrix}; \quad (4.41)$$

- the adjoint velocity vector, or *primer vector*, is defined as

$$\boldsymbol{\lambda}_\mathcal{V} = \begin{Bmatrix} \lambda_{\dot{\xi}} \\ \lambda_{\dot{\eta}} \\ \lambda_{\dot{\zeta}} \end{Bmatrix}. \quad (4.42)$$

The equation (4.40) can be reformulated as follows, by collecting all terms that multiply the thrust into the coefficient  $\mathcal{S}_\mathcal{F}$ , named *switching function*:

$$\mathcal{H} = \boldsymbol{\lambda}_\rho^T \boldsymbol{\mathcal{V}} + \boldsymbol{\lambda}_\mathcal{V}^T [\boldsymbol{g}(\boldsymbol{\rho}) + \boldsymbol{h}(\boldsymbol{\mathcal{V}})] + T \mathcal{S}_\mathcal{F}, \quad (4.43)$$

in which

$$\mathcal{S}_\mathcal{F} = \frac{\boldsymbol{\lambda}_\mathcal{V}^T \boldsymbol{T}}{m} - \frac{\lambda_m}{c}. \quad (4.44)$$

In accordance with PMP introduced earlier, the optimal control is the one that maximize the Hamiltonian in equation (4.43) and as a consequence the merit index for the trajectory. Being the control vector  $\boldsymbol{u}(t)$  composed by the thrust vector  $\boldsymbol{T}$  (defined by magnitude and direction), it turns out that  $\mathcal{H}$  is linear with respect to the control itself. Therefore, as evidenced in Section 4.3.2, the necessity of a bang-bang control arises:

- when  $\mathcal{S}_\mathcal{F} > 0 \implies T = T_{max}$ ;
- when  $\mathcal{S}_\mathcal{F} < 0 \implies T = 0$ .

Now, thrust direction must be determined. The thrust vector  $\boldsymbol{T}$  can be expressed in synodic components by means of two angles,  $\alpha_T$  and  $\beta_T$ , shown in the Figure 4.1.

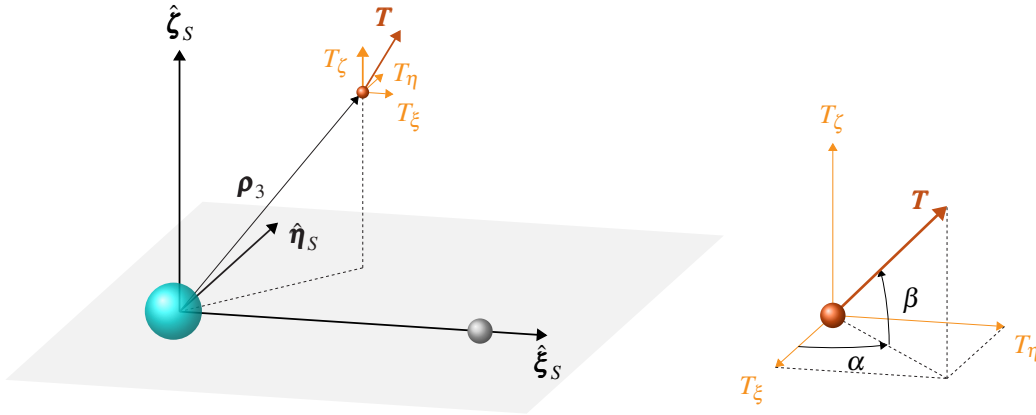


Fig. 4.1 Thrust angles and components in the synodic RS

Hence,

$$\mathbf{T} = \begin{Bmatrix} T_\xi \\ T_\eta \\ T_\zeta \end{Bmatrix} = T \begin{Bmatrix} \cos \beta_T \cos \alpha_T \\ \cos \beta_T \sin \alpha_T \\ \sin \beta_T \end{Bmatrix}, \quad (4.45)$$

with  $T = \|\mathbf{T}\|$ . The optimal thrust direction, in order to maximize  $\mathcal{S}_{\mathcal{F}}$  and consequently  $\mathcal{H}$ , is parallel to the primer vector  $\lambda_{\mathcal{V}}$  [52]. Indeed, the optimal values of  $\alpha_T$  and  $\beta_T$  can be retrieved by the derivatives of  $\mathcal{H}$  in eq. (4.39) with respect to the same angles, resulting in

$$\frac{\partial \mathcal{H}}{\partial \alpha_T} = -\lambda_{\xi} \sin \alpha_T + \lambda_{\eta} \cos \alpha_T = 0 \quad (4.46a)$$

$$\frac{\partial \mathcal{H}}{\partial \beta_T} = \lambda_{\zeta} \cos \beta_T - (\lambda_{\xi} \cos \alpha_T + \lambda_{\eta} \sin \alpha_T) \sin \beta_T = 0. \quad (4.46b)$$

By appropriately manipulating the two above equations, one obtains the optimal directions

$$\cos \beta_T \cos \alpha_T = \frac{\lambda_{\xi}}{\lambda_{\mathcal{V}}} \quad (4.47a)$$

$$\cos \beta_T \sin \alpha_T = \frac{\lambda_{\eta}}{\lambda_{\mathcal{V}}} \quad (4.47b)$$

$$\sin \beta_T = \frac{\lambda_{\zeta}}{\lambda_{\mathcal{V}}} \quad (4.47c)$$

$$(4.47d)$$

which coincide with the cosine directors of the primer vector itself and incidentally match the components of the thrust vector in equation (4.45). Note that  $\lambda_\gamma = \|\boldsymbol{\lambda}_\gamma\|$ .

Therefore, equation (4.44) can be rewritten in its scalar form

$$\mathcal{S}_{\mathcal{F}} = \frac{\lambda_\gamma}{m} - \frac{\lambda_m}{c}, \quad (4.48)$$

For what concerns the adjoint values, they can be found integrating the Euler-Lagrange equations, obtained in turn by deriving the Hamiltonian with respect to the corresponding state variables, as seen in eq. (4.10) and computed in Appendix B, allowing the problem to be completely defined.

However, as anticipated at the beginning of this chapter, indirect methods may face challenges with numerical stability, especially in the handling of thrust discontinuity. In fact, it may happen that the switching function, which is crucial in the bang-bang control of thrust, takes on fluctuating values around zero, causing numerical issues in the evaluation of gradients, compromising the convergence of the process. In such cases a pre-defined sequence of thrust and coast arcs could be adopted, therefore specifying a switching function "a priori", transforming the TPBVP into a MPBVP.

In this thesis, the latter procedure was not necessary. However, it could prove to be very useful when introducing perturbations which increase the fidelity of the dynamic model, enhancing numerical accuracy, convergence speed, and overall robustness of the code.

## Chapter 5

# Computation of Optimal De-Orbiting Trajectories

Established the mathematical foundations of the problem, this chapter provides a detailed description of all necessary elements to fully define and solve the case study: the optimization of low-thrust de-orbiting trajectories from the southern Earth-Moon Lagrangian Point  $L_2$  (EML<sub>2</sub>) Near-Rectilinear Halo Orbit (NRHO) with a 9 : 2 synodic resonance with the Moon's orbit around Earth. The primary objective is to reach the lunar north pole, selected as the graveyard region for decommissioned spacecrafts, with the lowest propellant consumption. The dynamic model, extensively described in Chapter 2, considers the gravitational effects of both the Moon and the Earth. The trajectory of the two primaries with respect to the center of mass of the binary system is assumed to be circular, placing this study within the framework of the Circular Restricted Three-Body Problem (CR3BP), offering a sufficiently precise basis for preliminary analysis applicable to real-world scenarios.

First, the physical and propulsion characteristics of the spacecraft used in the analysis must be specified and are summarized in Table 5.1, essential for evaluating the propellant consumption using equation (4.33c). The reference values indicated for the thruster pertain to a xenon Hall-effect currently undergoing testing [69].

Quantity	Unit	Value
Initial mass	$m_0$ [kg]	600
Thrust	$T$ [N]	0.6
Specific Impulse	$I_{sp}$ [s]	2800

Table 5.1 SC characteristic values

Once the optimal trajectory is determined,  $m_f$  is obtained immediately, and consequently,  $m_p$  can be calculated as

$$m_p = m_0 - m_f. \quad (5.1)$$

Subsequently, the  $\Delta V$  required to de-orbit the satellite can be derived using the Tsiolkovsky equation:

$$\Delta V = -I_{sp} g_0 \ln \left( \frac{m_f}{m_0} \right) \quad (5.2)$$

The fundamental physical values used in the analyses to non-dimensionalize the equations can be found in Table 5.2.

Physical constant	Unit	Value
Mass parameter $\mu$		0.012150587
Length unit	[km]	384400
Time unit	[day]	4.342479846
Mass unit	[kg]	600

Table 5.2 Non-dimensionalizing values

The fixed-time analyses are conducted by varying the starting point from the NRHO, thereby determining the propellant consumption of the optimal trajectories obtained by solving the TPBVP resulting from the application of OCT to the problem by a single-shooting method via DC with appropriate boundary conditions.

## 5.1 Boundary Conditions

### 5.1.1 Terminal Conditions

The final position target for the de-orbiting trajectories is a designated graveyard region on the lunar surface at the lunar north pole identified by the synodic coordinates  $\boldsymbol{\rho}_f = \{1 - \mu, 0, 4.51873 \times 10^{-3}\}^T$ . In terms of velocities, as this is an End-of-Life (EOL) disposal strategy, a soft landing is not required. Therefore, the  $\dot{\xi}_f$  and  $\dot{\eta}_f$  velocities are not targeted; instead, an indicative  $\dot{\zeta}_f = -0.05$  is imposed to guide optimization towards trajectories reaching the north pole from above and not intersecting the Moon's body.

As a consequence of transversality and optimality conditions (refer to Section 4.3.1), the adjoint variables  $\lambda_{\xi_f}$ ,  $\lambda_{\eta_f}$ ,  $\lambda_{\zeta_f}$ ,  $\lambda_{\dot{\zeta}_f}$  and both  $\mathcal{H}_0$  and  $\mathcal{H}_f$  are free,  $\lambda_{\xi_f}$  and  $\lambda_{\eta_f}$  at the final time must be null (since the corresponding variables are free) while  $\lambda_{m_f}$  is set to 1, as  $m_f$  is the subject of maximization. In a concise form, the reduced set of terminal boundary conditions  $\boldsymbol{\chi}_f = \{\xi_f, \eta_f, \zeta_f, \dot{\zeta}_f, \lambda_{\xi_f}, \lambda_{\eta_f}, \lambda_{m_f}, \tau_f\}^T$  is

$$\boldsymbol{\chi}_f = \{9.87849 \times 10^{-1}, 0, 4.51873 \times 10^{-3}, -5 \times 10^{-2}, 0, 0, 1, \tau_f\}^T. \quad (5.3)$$

The iterative procedure described in Section 4.5 is stopped when the norm of the errors on the final boundary conditions reaches a certain tolerance. In this case, a tolerance of  $1 \times 10^{-7}$  has been set for errors on all BCs except for  $\xi_f$  and  $\eta_f$ , whose tolerance is increased to  $1 \times 10^{-4}$  by characterizing a region around the north pole.

As anticipated, since in the implemented dynamic model the Hamiltonian is extremely sensitive to differential corrections, fixed-time analyses have been opted for, modifying  $\tau_f$  for each analysis according to the starting point in order to accommodate mission times, spacing in a dimensional range of  $5.475 \text{ days} \div 9.740 \text{ days}$ . Since a time constraint can lead to finding sub-optimal solutions (being optimal solutions for that specific time, but not in general), an attempt was made to perform a sensitivity analysis on time, by appropriately varying the final time of first convergence per each point and analyzing the behavior of  $\delta_{\mathcal{J}}$  and consequently  $m_p$ .

### 5.1.2 Initial Conditions

As previously mentioned, the analysis is conducted by optimizing various de-orbiting trajectories that originate from different points of the selected NRHO. The initial positions and velocities of the spacecraft have been calculated through the integration performed in Section 3. Specifically, considering the reference starting point as the furthest from the Moon, i.e., the apolune, the preceding and subsequent points of the orbit are indicated in terms of the percentage of orbital period elapsed, with 0% corresponding to the apolune. Negative and positive values indicate positions before or after the apolune in the orbit, respectively. The analysis considers 28 starting points, ranging from -35% to 32.5%, equally distributed in time along the NRHO.

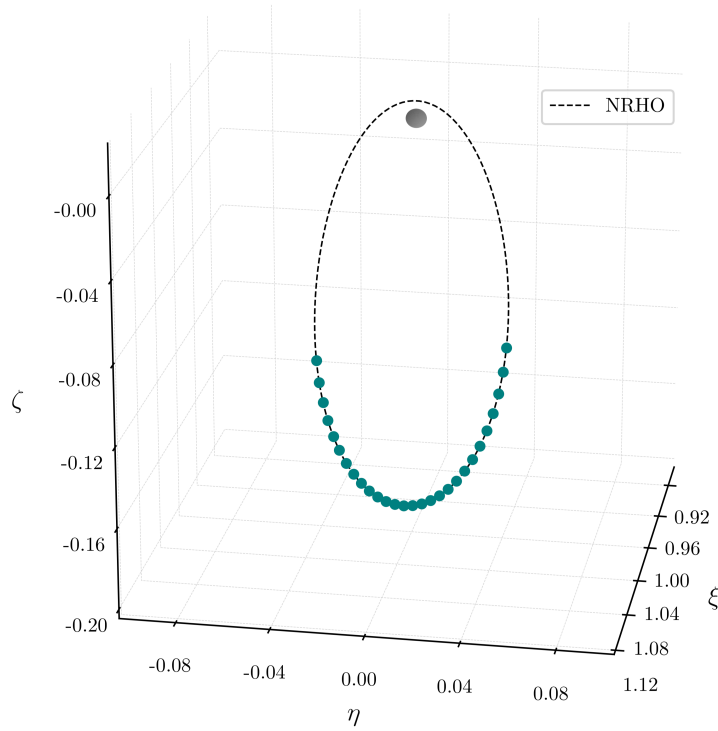


Fig. 5.1 Equal time distribution of starting point near apolune

As shown in Figure 5.1, the points tend to cluster near apolune due to the SC's low velocity in that region.

The initial mass of the SC is set to 600 kg, corresponding to 1 mass unit, while for each trajectory  $\tau_0$  is set to 0. Having thus assigned all positions, velocities, and the

initial mass in the initial state vector, it follows that the initial guesses needed to start the iterative procedure refer to all the corresponding adjoint variables, encapsulated in the adjoint vector

$$\boldsymbol{\lambda}_0 = \left\{ \lambda_{\xi_0}, \lambda_{\eta_0}, \lambda_{\zeta_0}, \lambda_{\dot{\xi}_0}, \lambda_{\dot{\eta}_0}, \lambda_{\dot{\zeta}_0}, \lambda_{m_0} \right\}^T. \quad (5.4)$$

To start the optimization procedure, reasonable initial guesses are essential. One of the disadvantages of indirect methods is that adjoint variables lack direct physical meaning, therefore their evolutions and influences could be more or less predictable. Consequently, inappropriate initial guesses of adjoint variables can lead to convergence issues because the problem is highly sensitive to these initial guesses. This sensitivity makes it crucial to provide well-considered initial values to ensure the optimization procedure converges effectively. For example, an interpretation of the velocity adjoint variables is linked to the importance of the primer vector, which dictates the optimal thrust direction. Indeed, the larger the adjoint in a velocity direction, the more thrust will be emphasized in that direction. If the adjoint is positive, the thrust will align with it; if negative, the thrust will oppose it. This interpretation highlights how the magnitude and sign of velocity adjoints guide the spacecraft's acceleration and deceleration to achieve the desired trajectory. Less intuitive, however, are the adjoints related to the synodic coordinates.

## 5.2 Results

Based on the procedure outlined in the previous sections, the single shooting method via DC allowed for the computation of the various trajectories, each with its specific initial conditions, and proceeding through continuity. The first convergence of the iterative procedure led to the optimal de-orbiting trajectory starting from the apolune of the NRHO. As already noted, to limit the risk of encountering sub-optimal trajectories, the final time around the value of first convergence was varied delicately, thus analyzing its influence on the shape and position of the switching function. Figure 5.2 shows, for the first point analyzed, a lowering of  $\mathcal{S}_{\mathcal{F}}$  as  $\tau_f$  increases. This results in a reduction of propellant consumption considering the shape of  $\mathcal{S}_{\mathcal{F}}$ , which, when lowering, tends to enlarge the coasting arc.

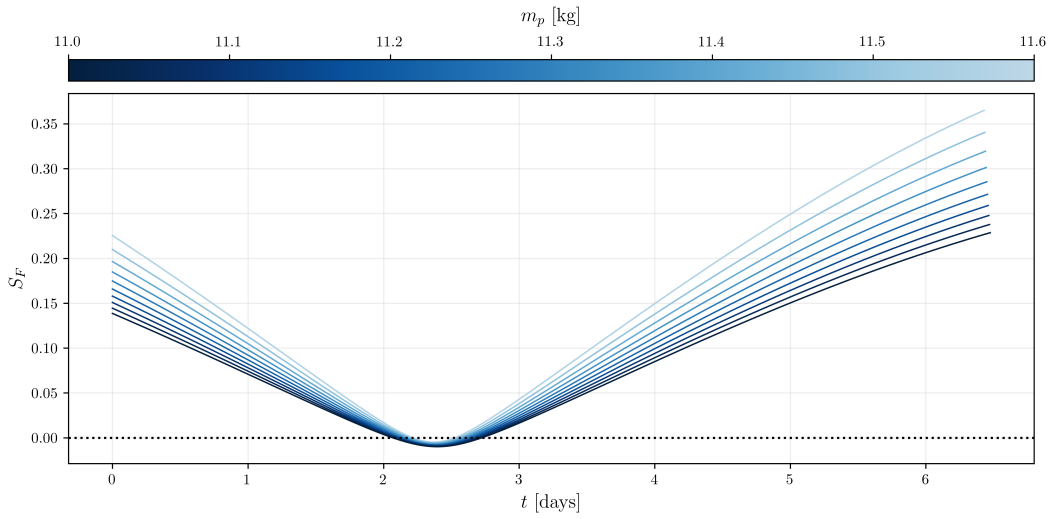


Fig. 5.2  $\tau_f$  influence on  $S_f$

This type of investigation was conducted for each point chosen on the NRHO, where permitted by the numerical sensitivity of the problem.

Thus, based on the results obtained from the first point, an exploration was carried out on trajectories departing both before and after apolune position, resulting in the set of trajectories depicted in Figure 5.3. It should be noted how the injection point for the transfer has a considerable impact on the disposal cost in terms of propellant, as indicated by the color map of  $m_p$ . For clarity, Figure 5.4 represents only the injection points on the NRHO, colored according to the propellant consumption of the associated trajectory.

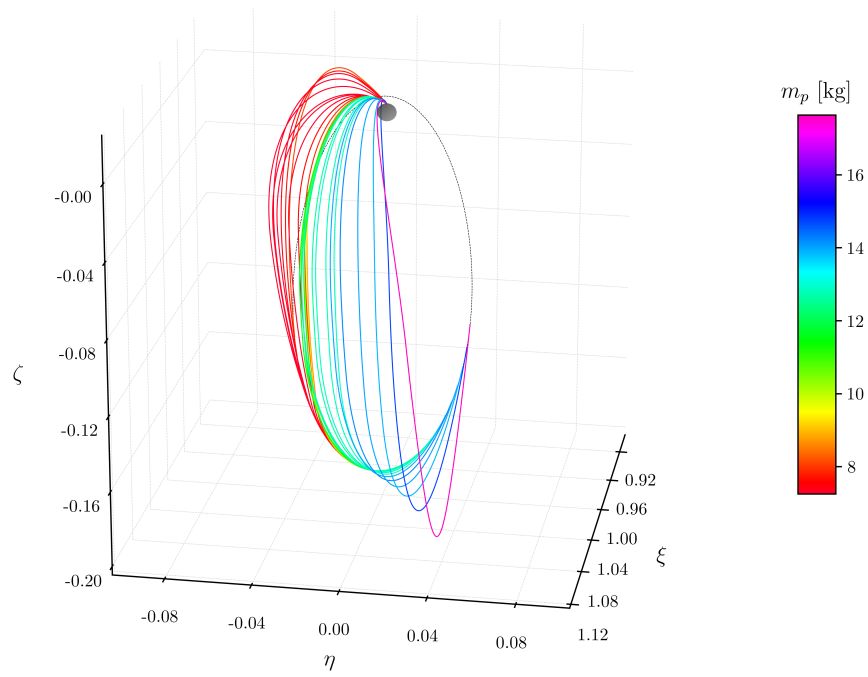


Fig. 5.3 Optimal de-orbiting trajectories

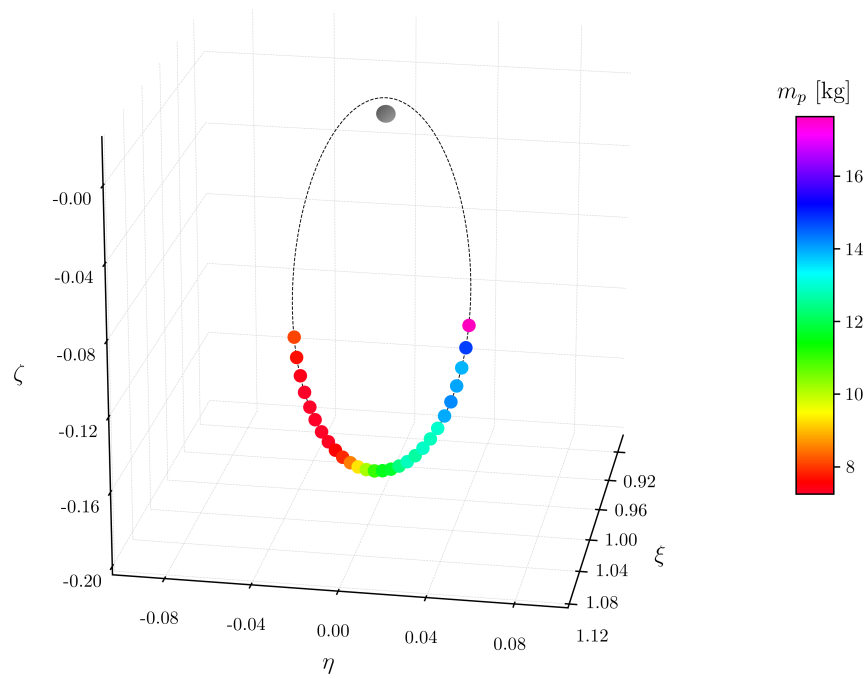


Fig. 5.4 Optimal de-orbiting trajectories - Injection points

Figure 5.5 shows the trend of the final time of each trajectory in days, demonstrating a natural decreasing trend as one progresses along the NRHO and starting from points that "facilitate" the trajectory for the disposal of the satellite into the desired area, not necessitating major directional deviations to reach the graveyard region.

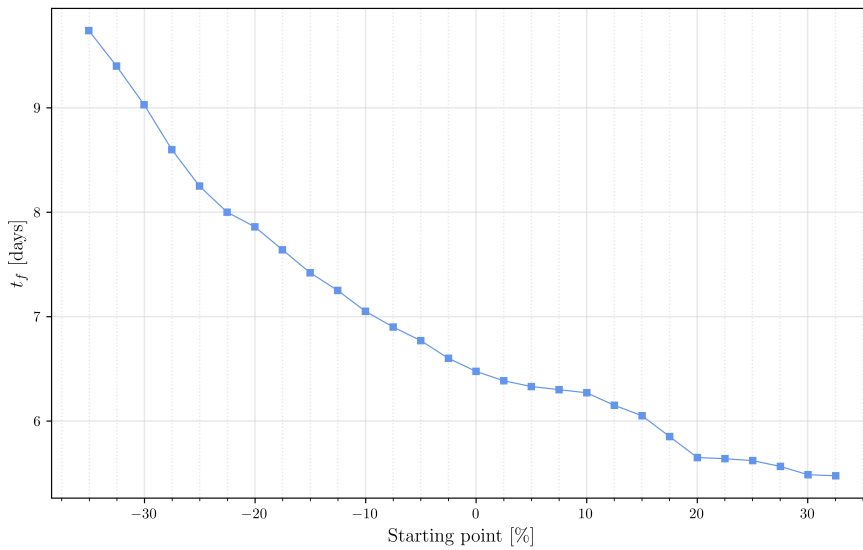


Fig. 5.5 Fixed  $\Delta T$  - Injection point position

Figure 5.6 presents the trend of propellant mass consumption and therefore required  $\Delta V$  as a function of the injection point. Trajectories starting from points before the -35% of the orbit were not investigated due to their low interest given the increasing trend in consumption. Conversely, points beyond 32.5% of the orbit, given the satellite mass and thrust under consideration, do not allow for direct de-orbiting trajectories and thus cannot be compared with those previously determined. Of all the optimal de-orbiting trajectories obtained, those requiring the minimum propellant consumption (in nuances of red in Figs. 5.3 and 5.4) depart from the portion of the orbit immediately following the apolune, clearly identifying a minimum near the point corresponding to 22.5% of the orbit, as can be seen in Figure 5.6.

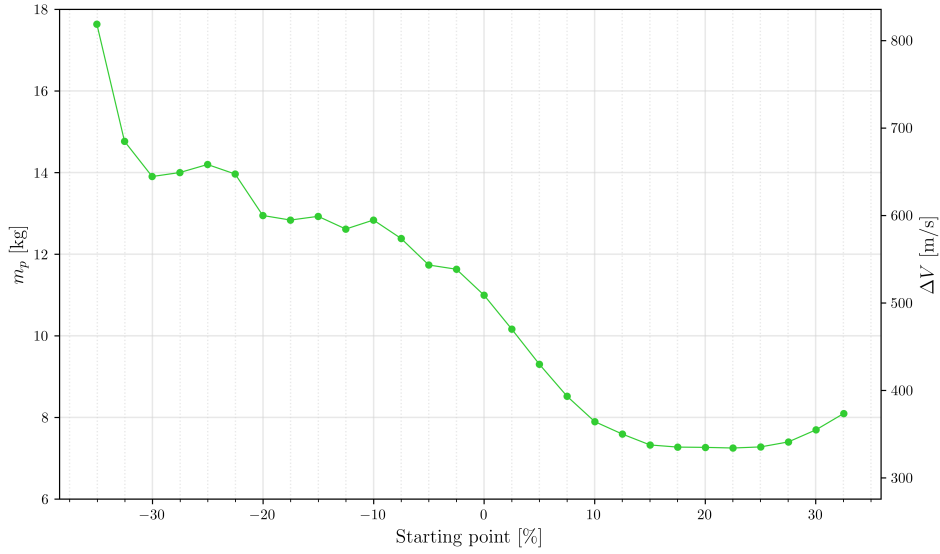


Fig. 5.6 Propellant consumption and required  $\Delta V$  - Injection point position

The optimal minimum-propellant de-orbiting trajectory is depicted in Figure 5.7, where red and green colours indicate thrust and coasting arcs respectively. Its initial conditions and the value of  $\lambda_0^*$  that allows solving of TPBVP are summarized in Table 5.3. The final time that showed the best results within the convergence limits of the code is  $t_f = 5.6385$  days. Figure 5.8 shows the time evolution of each position and velocity component during such trajectory observing how the boundary conditions imposed on  $\xi$ ,  $\eta$ ,  $\zeta$  and  $\dot{\zeta}$  are met at  $t_f$ . Notice how slope variations correspond to specific moments in the trajectory when the thruster is activated or deactivated.

Figure 5.9 presents the switching function and mass profile for the entire minimum-propellant trajectory. The bang-bang control, derived from Pontryagin's Maximum Principle (PMP), dictates that the thrust is activated whenever  $\delta_{\mathcal{F}}$  is positive, thus defining the thrust arcs of the trajectory. The percentage of time during which the switching function assumes negative values, effectively constituting the coasting phases, amounts to 32% of  $t_f$ . In such time intervals the SC mass remains constant. On the contrary, as expected from equation 4.33c, during the the time intervals when the switching function is positive, depicted in red in Figure 5.7, there is a reduction in mass because propellant is being consumed. The final mass of the SC turns out to be  $m_f = 592.7496$  kg, which corresponds to  $m_p = 7.2504$  kg and  $\Delta V = 333.5484$

m/s. This reduction in propellant required for de-orbiting of up to 60% allows the mission to allocate more fuel for earlier operational phases, effectively extending the mission’s operational lifespan.

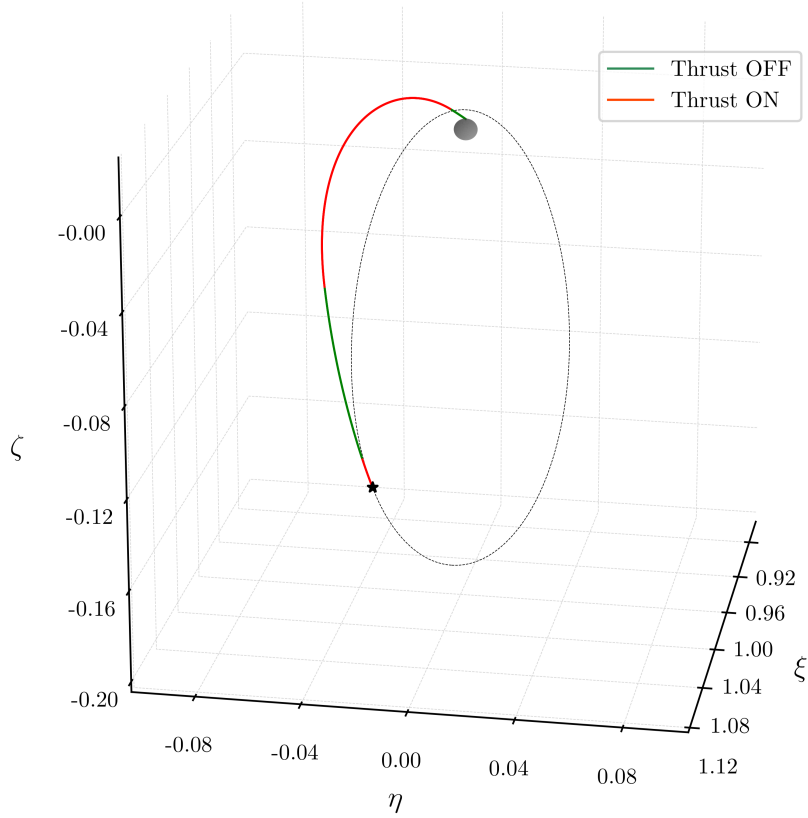
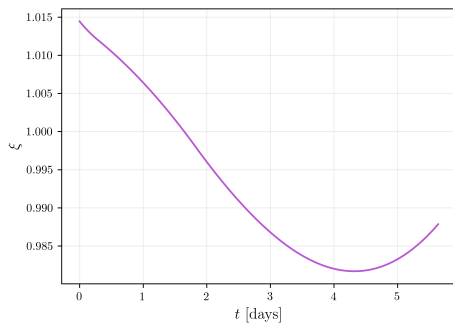


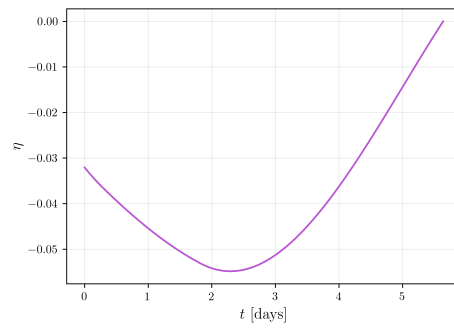
Fig. 5.7 Minimum-propellant optimal de-orbiting trajectory

Parameter	Value
$\boldsymbol{\rho}_0$	$\{1.014447, -0.032061, -0.152135\}^T$
$\boldsymbol{\mathcal{V}}_0$	$\{-0.044099, -0.074989, 0.181507\}^T$
$m_0$	1
$\boldsymbol{\lambda}_{\rho_0}^*$	$\{0.020814, 0.027155, 0.030372\}^T$
$\boldsymbol{\lambda}_{\mathcal{V}_0}^*$	$\{0.030307, 0.015413, -0.016221\}^T$
$\lambda_{m_0}^*$	0.987661

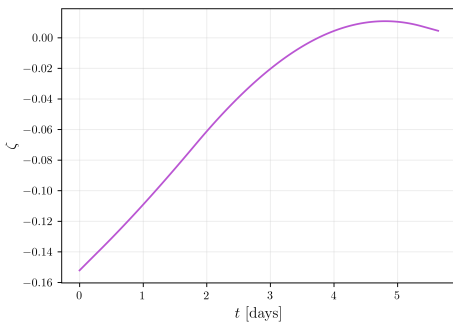
Table 5.3 Initial state and costate for the minimum-propellant solution



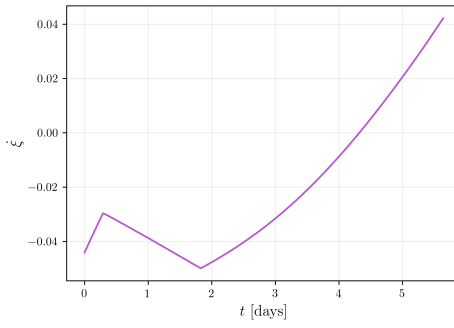
(a)  $\xi$  vs  $\tau$



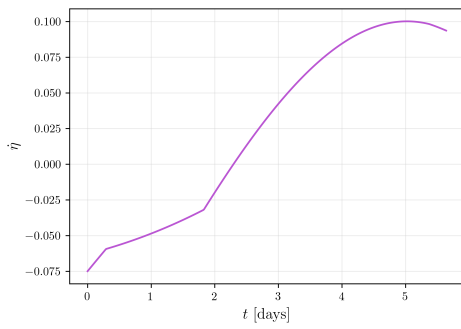
(b)  $\eta$  vs  $\tau$



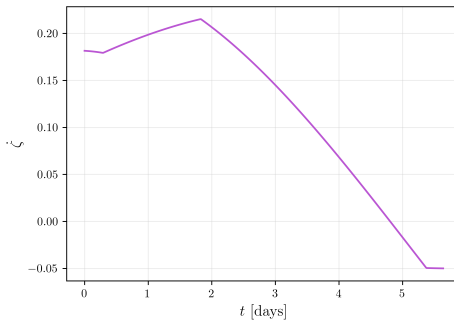
(c)  $\zeta$  vs  $\tau$



(d)  $\dot{\xi}$  vs  $\tau$



(e)  $\dot{\eta}$  vs  $\tau$



(f)  $\dot{\zeta}$  vs  $\tau$

Fig. 5.8 Evolution in time of synodic positions and velocities

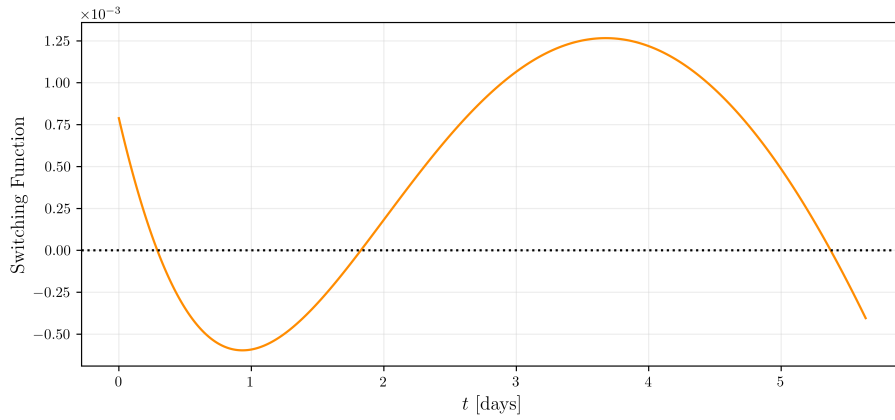
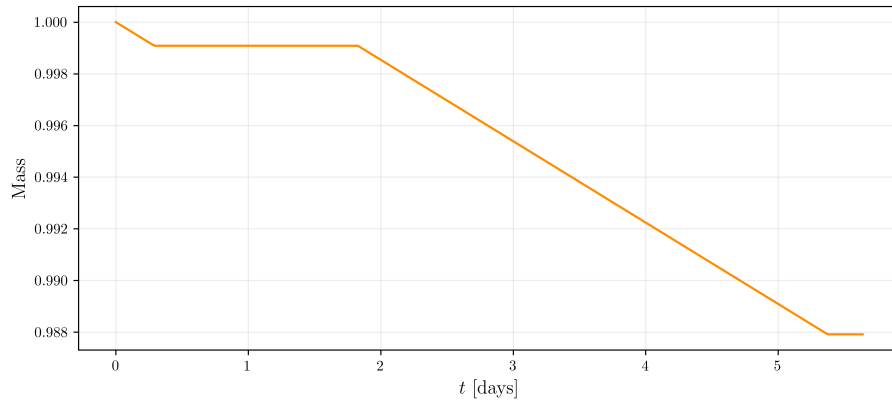

 (a)  $S_{\mathcal{G}}$  vs  $\tau$ 

 (b)  $m$  vs  $\tau$ 

Fig. 5.9 Evolution in time of switching function and mass

To interpret what happens from a dynamic perspective, it is useful to observe the trends of  $\alpha_T$  and  $\beta_T$ , which are the angles in the  $\hat{\xi}_S - \hat{\eta}_S$  plane and out of the plane (refer to Fig. 4.1) respectively. From Figure 5.10a, it can be observed that  $\alpha_T$  starts from a positive value of about  $25^\circ$  and increases monotonically. Initial values are indicative of a deviation from the dotted NRHO in the first red arc in which the thrust has a dominant braking effect on the negative  $\dot{\xi}$ , as outlined by the positive  $\lambda_{\xi_0}$  value, greater than the other adjoint velocity variables. Then, in the second thrust arc an increasingly predominant thrust in the positive  $\hat{\eta}_S$  and negative  $\hat{\xi}_S$  directions is observed, which causes the trajectory to close to curve and reach the designated point. Indeed, as shown in Figure 5.10b,  $\beta_T$  starts from a negative value of  $-25^\circ$  and decreases monotonically, indicating a braking action against the positive  $\dot{\xi}$ , reaching

values of  $-80^\circ \div -85^\circ$  in the second thrust arc, contributing to the curvature of the trajectory and its subsequent closure towards the lunar north pole.

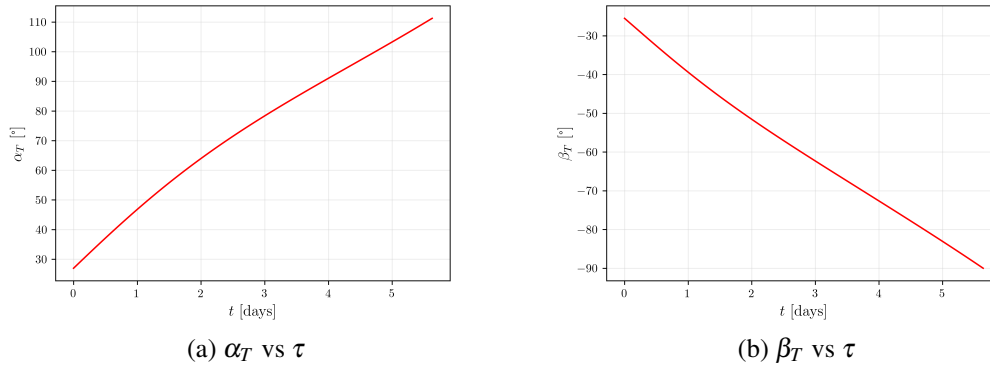
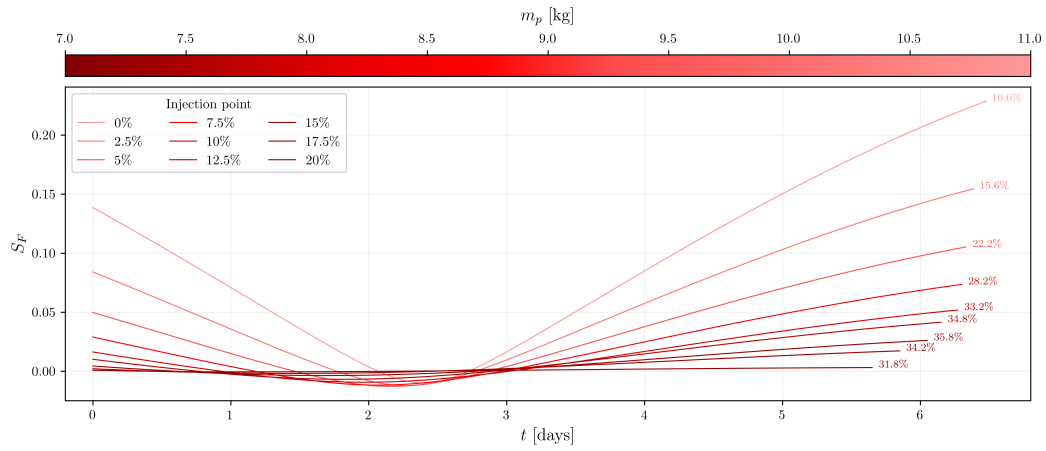


Fig. 5.10 Evolution in time of thrust angles

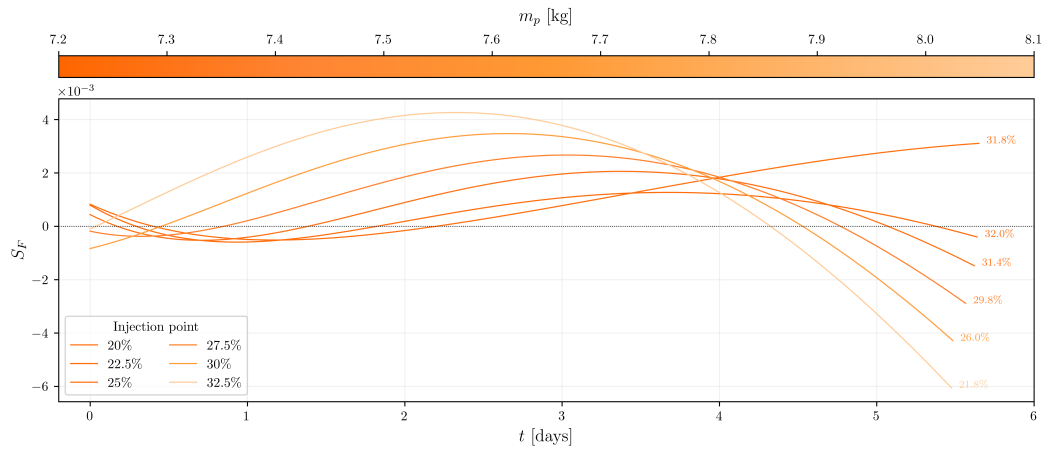
An interesting result is shown in Figure 5.11, which displays the behaviors of the different switching functions. These functions pertain to each optimal trajectories departing from points with relative positions to apolune in the range of 0% to 32.5%. For clarity, the ranges are divided into 0% to 20% and 20% to 32.5%. These intervals correspond to the orbital arc that demonstrates clear advantages in terms of propellant burned (refer to Fig. 5.6). At the last point of each curve, the duration of the coasting phase is indicated as a percentage of the total trajectory duration.

Figure 5.11a focuses on the first range, corresponding to the descending phase of the  $m_p$  trend. The switching functions belong to the same family (thrust-coast-thrust, or T-C-T phases) but tend to decrease their slope at the initial and final segments, flattening along the zero ordinate as the injection point progresses along the NRHO. Consequently, this tends to extend the coasting phase, thereby progressively reducing the  $m_p$ . Note that a higher coasting percentage does not necessarily imply lower propellant consumption, as the duration of each trajectory varies, still potentially resulting in a longer phase with the thruster active, and vice versa. In Figure 5.11b, a transition is observed from switching functions of the T-C-T type to T-C-T-C (like the minimum consumption one shown in Fig. 5.7) and C-T-C types, with a slight increasing trend in  $m_p$ , due to longer durations of thrust arcs. Indeed, the switching functions tend to bulge towards positive values, activating the thrust for a longer duration.

## Computation of Optimal De-Orbiting Trajectories



(a) Focus on  $S_F$  of 0% ÷ 20% departing point trajectories



(b) Focus on  $S_F$  of 20% ÷ 32.5% departing point trajectories

Fig. 5.11 Behavior of  $S_F$  under different analysis conditions

# Chapter 6

## Conclusion

In this thesis, the formulation of low-thrust minimum-propellant trajectories in the Circular Restricted Three-Body Problem using indirect optimal control is discussed, with applications to de-orbiting trajectories from a Earth-Moon Near-Rectilinear Halo Orbit about  $L_2$  into a graveyard region around the lunar north pole.

The choice of this scenario aligns with the growing interest in cislunar space in recent years, as evidenced by the increasing number of space missions focusing on periodic and quasi-periodic orbits around the Earth-Moon Lagrangian points. Additionally, with the advancement of the Artemis program, these specific orbits may become prime staging areas for efforts to colonize the Moon and the near-Earth space. The chosen representative orbit for this case study is the Near-Rectilinear Halo Orbit where the construction of the Lunar Orbital Platform-Gateway is planned. This orbiting station will play a crucial role in humanity's return to the Moon, with the ultimate goal of exploring Mars. Within the CR3BP framework, its periodic motion around  $L_2$  has been computed by means of single shooting and differential correction strategies.

The NASA-led ambitious program, along with many other planned space missions, will increasingly attract stakeholder interest in cislunar space. Consequently, there will be a growing need to implement appropriate end-of-life strategies to reduce space debris. This proactive approach is essential for ensuring sustainable and safe operations in the cislunar environment, as the number of missions and activities in this region is expected to rise significantly. As a result, it has become interesting

to explore a direct disposal strategy involving the de-orbiting of a satellite into a designated graveyard region near the lunar north pole.

As the central core of this thesis, the problem has been formulated as an Optimal Control Problem. The optimization was carried out using an indirect approach based on Optimal Control Theory, that transformed the OCP into a Two-Point Boundary Value Problem, solved employing a single-shooting method via Differential Correction. Different initial conditions on the NRHO were considered, conducting a parametric study of the propellant mass consumed relative to the injection point. Necessary and optimality conditions were derived and the bang-bang control was defined in accordance with the Pontryagin's Maximum Principle. The implemented indirect method has proven to be very precise and suitable for complex optimization problems, with dynamics that are far from simple and straightforward. Despite typical numerical issues of non-convergence, these were mitigated by specific strategies aimed at strengthening the code.

Results showed a strong influence of the position of the injection point on the propellant consumption, identifying a specific post-apolune orbital arc on the NRHO deemed ideal for de-orbiting the satellite, enabling significant propellant savings which can be utilized for earlier operational phases, thereby extending the satellite's operational life. Finally, a focus on the two-burn optimal minimum-propellant trajectory was provided, showing how all the BCs are met with high accuracy.

## 6.1 Future Research

Although the dynamic model used in this work, the Circular Restricted Three-Body Problem, contains some simplifications and does not accurately reflect the complexities of the solar system, it serves as a robust foundation for future developments. Furthermore, the strong numerical sensitivity of the Hamiltonian did not allow for variable time analyses, which constitutes a limitation of this work, although it is significantly mitigated by the analyses performed on different final times.

Several future developments and improvements can be considered, including but not limited to:

- implementing strategies to dampen the numerical behavior of the Hamiltonian in order to perform variable time analyses;

- employing the N-Body Problem as dynamic model with the use of JPL's ephemerides for precise planetary positional data;
- including perturbations such as Solar Radiation Pressure or Moon and/or Earth asphericity;
- transforming the Two-Point Boundary Value Problem into a Multi-Point Boundary Value Problem by the adoption of predefined sequences of thrust and coast arcs that simplify the computational process and enhance the robustness of the code;
- implementing of a multiple-shooting strategy in order to better guide the iterative process;
- imposing inequality constraints on final velocities;
- investigating multi-revolution de-orbiting trajectories.

# References

- [1] Joseph-Louis Lagrange. Essai sur le problème des trois corps, 1772.
- [2] Sean O’Keefe. The vision for space exploration. *National Aeronautics and Space Administration*, pages 1–38, 2004.
- [3] Pietro Giordano, Antoine Grenier, Paolo Zoccarato, Lorenzo Bucci, Alexander Cropp, Richard Swinden, David Otero, Wael El-Dali, William Carey, Ludovic Duvet, Bernhard Hufenbach, Fabrice Joly, and Javier Ventura-Traveset. Moonlight navigation service-how to land on peaks of eternal light. In *Proceedings of the 72nd International Astronautical Congress (IAC), Dubai, United Arab Emirates*, pages 25–29, 2021.
- [4] David Folta and Frank Vaughn. A survey of earth-moon libration orbits: stationkeeping strategies and intra-orbit transfers. In *AIAA/AAS Astrodynamics Specialist Conference and Exhibit*, page 4741, 2004.
- [5] Mark Woodward, David Folta, and Dennis Woodfork. Artemis: The first mission to the lunar libration orbits. In *International Symposium on Space Flight Dynamics*, 2009.
- [6] National Aeronautics and Space Administration. ARTEMIS (THEMIS). <https://science.nasa.gov/mission/themis-artemis/>, 2007.
- [7] Lin Xu, Yongliao Zou, and Yingzhuo Jia. China’s planning for deep space exploration and lunar exploration before 2030. *Space Sci*, 38(5):591–592, 2018.
- [8] Kenta Oshima, Stefano Campagnola, Chit Hong Yam, Yuki Kayama, Yasuhiro Kawakatsu, Naoya Ozaki, Quentin Verspieren, Kota Kakihara, Kenshiro Oguri, and Ryu Funase. Equuleus mission analysis: design of the transfer phase. In *International Symposium on Space Technology and Science, ISTS-2017-d-159, Ehime, Japan*, pages 3–9, 2017.
- [9] National Aeronautics and Space Administration. Artemis. <https://www.nasa.gov/humans-in-space/artemis/>, 2024.
- [10] National Aeronautics and Space Administration. NASA’s Lunar Exploration Overview. 2020.

- 
- [11] National Aeronautics and Space Administration. [cislunar autonomous positioning system technology operations and navigation experiment (capstone)]. <https://www.nasa.gov/mission/capstone/>, 2022.
- [12] Dylan Connell and Briana R. Zamora. A lunar orbit that’s just right for the international gateway. *National Aeronautics and Space Administration*, 2020.
- [13] David E. Lee. White paper: Gateway destination orbit model: A continuous 15 year nrho reference trajectory. Technical report, 2019.
- [14] Melissa L. McGuire, Steven L. McCarty, and Laura M. Burke. Power and propulsion element (PPE) spacecraft reference trajectory document. Technical report, 2020.
- [15] Carolin Frueh, Kathleen Howell, Kyle J DeMars, and Surabhi Bhadauria. Cislunar space situational awareness. In *31st AIAA/AAS Space Flight Mechanics Meeting*, pages 6–7, 2021.
- [16] Paolo Guardabasso, Stéphanie Lizy-Destrez, and Marie Ansart. Lunar orbital debris mitigation: Characterisation of the environment and identification of disposal strategies. In *8th European Conference on Space Debris*, volume 8, 2021.
- [17] Paolo Guardabasso, Despoina K. Skoulidou, Lorenzo Bucci, Francesca Letizia, Stijn Lemmens, and Stéphanie LizyDestrez. Cislunar debris mitigation: Development of a methodology to assess the sustainability of lunar missions. In *72nd International Astronautical Congress (IAC)*, 2021.
- [18] Carmela Marika Accettura. Debris mitigation and atmospheric deorbiting analysis for lunar L2 NRHO departing spacecraft. Master’s thesis, Politecnico di Torino, 2023.
- [19] Daria Andrievskaia, Ignacio Cáceres Ballesteros, Paolo Guardabasso, and Stéphanie Lizy-Destrez. Analysis of lunar impacts for orbital debris mitigation. In *73rd International Astronautical Congress (IAC), Paris, France: International Astronautical Federation*, 2022.
- [20] National Aeronautics and Space Administration. Gravity Recovery And Interior Laboratory (GRAIL). <https://science.nasa.gov/mission/grail/>, 2011.
- [21] National Aeronautics and Space Administration. Lunar Atmosphere and Dust Environment Explorer (LADEE). <https://science.nasa.gov/mission/ladee/>, 2013.
- [22] Luigi Mascolo. *Low-Thrust Optimal Escape Trajectories from Lagrangian Points and Quasi-Periodic Orbits in a High-Fidelity Model*. PhD thesis, Politecnico di Torino, 2023.
- [23] John E. Prussing and Bruce A. Conway. *Orbital Mechanics*. Oxford University Press, 1993.

- 
- [24] Hanspeter Schaub and John L. Junkins. *Analytical mechanics of space systems*. Aiaa, 2003.
- [25] Roger R. Bate, Donald D. Mueller, Jerry E. White, and William W. Saylor. *Fundamentals of astrodynamics*. Courier Dover Publications, 2020.
- [26] Ivan I. Mueller. Reference coordinate systems and frames: Concepts and realization. *Journal of Geodesy*, 59:181–188, 1985.
- [27] U.S. Naval Observatory. International Celestial Reference System (ICRS). [https://aa.usno.navy.mil/faq/ICRS\\_doc](https://aa.usno.navy.mil/faq/ICRS_doc).
- [28] Jet Propulsion Laboratory Solar System Dynamics. JPL Planetary and Lunar Ephemerides: Export Information. [https://ssd.jpl.nasa.gov/planets/eph\\_export.html](https://ssd.jpl.nasa.gov/planets/eph_export.html), 2020.
- [29] National Aeronautics and Space Administration. Report concerning space data system standards - navigation data - definitions and conventions. Informational Report CCSDS 500.0-G-D, National Aeronautics and Space Administration, 2019. Green Book.
- [30] David J. Westpfahl. Orbital mechanics course notes. *New Mexico Institute of Mining and Technology, Lecture Notes, March*, 2011.
- [31] Alessandro Zavoli. Indirect optimization of bang-bang control problems and applications to formation flying missions, 2013.
- [32] Bruce A. Conway. *Spacecraft trajectory optimization*, volume 29. Cambridge University Press, 2010.
- [33] Daniel J. Grebow. Generating periodic orbits in the circular restricted three-body problem with applications to lunar south pole coverage. Master’s thesis, Purdue University, West Lafayette, Indiana, 2006.
- [34] Victor Szebehely. Theory of Orbits - The Restricted Problem of Three Bodies. *Academic Press*, page 364, 1967.
- [35] David L. Richardson. Periodic and quasi periodic halo orbits in the earth-sun/earth-moon systems. Technical report, Technical report, 2010. FDSS Contract# NNG10CP02C, Subtask 1 of Task Order 31: Advanced Mission Design, 2010.
- [36] David Lujan and Daniel J. Scheeres. Earth-moon l2 quasi-halo orbit family: Characteristics and manifold applications. *Journal of Guidance, Control, and Dynamics*, 45(11):2029–2045, 2022.
- [37] C.L. Goudas. Three-dimensional periodic orbits and their stability. *Icarus*, 2:1–18, 1963.
- [38] John D. Hadjidemetriou. The stability of periodic orbits in the three-body problem. *Celestial mechanics*, 12(3):255–276, 1975.

- 
- [39] Davide Guzzetti, Emily M. Zimovan, Kathleen C. Howell, and Diane C. Davis. Stationkeeping analysis for spacecraft in lunar near rectilinear halo orbits. In *27th AAS/AIAA Space Flight Mechanics Meeting*, volume 160, pages 3199–3218. American Astronautical Society, 2017.
- [40] Aleksandr Mikhailovich Lyapunov. The general problem of the stability of motion. *International Journal of Control*, 55(3):531–534, 1992.
- [41] Kathleen C. Howell. Families of orbits in the vicinity of the collinear libration points. *The Journal of the astronautical sciences*, 49:107–125, 2001.
- [42] B. Malcolm Brown, Michael S.P. Eastham, Karl Michael Schmidt, B. Malcolm Brown, Michael S.P. Eastham, and Karl Michael Schmidt. Floquet theory. *Periodic differential operators*, pages 1–29, 2013.
- [43] S.R. Barone, M.A. Narcowich, and F.J. Narcowich. Floquet theory and applications. *Physical Review A*, 15(3):1109, 1977.
- [44] Ryan J. Whitley, Diane C. Davis, Laura M. Burke, Brian P. McCarthy, Rolfe J. Power, Melissa L. McGuire, and Kathleen C. Howell. Earth-moon near rectilinear halo and butterfly orbits for lunar surface exploration. In *AAS/AIAA Astrodynamics Specialists Conference, Snowbird, Utah*, 2018.
- [45] Emily M. Zimovan, Kathleen C. Howell, and Diane C. Davis. Near rectilinear halo orbits and their application in cis-lunar space. In *3rd IAA Conference on Dynamics and Control of Space Systems, Moscow, Russia*, volume 20, page 40, 2017.
- [46] JPL Solar System Dynamics Group. Periodic Orbits: Orbits in the Circular Restricted Three-Body Problem, 2024.
- [47] NASA Eclipse Web Site. The Moon’s Orbit, 2024.
- [48] Brian McCarthy and Kathleen Howell. Quasi-periodic orbits in the sun-earth-moon bicircular restricted four-body problem. In *31st AAS/AIAA Space Flight Mechanics Meeting, virtual*, 2021.
- [49] Brian P. McCarthy and Kathleen C. Howell. Trajectory design using quasi-periodic orbits in the multi-body problem. In *Proceedings of the 29th AAS/AIAA space flight mechanics meeting*, page 20, 2019.
- [50] Joaquim RRA Martins and Andrew Ning. *Engineering design optimization*. Cambridge University Press, 2021.
- [51] L.S. Pontryagin, V.G. Boltyanskii, R.V. Gamkrelidze, and E.F. Mishchenko. The mathematical theory of optimal processes. *Interscience, NY*, 1962.
- [52] D.F. Lawden. *Optimal Trajectories for Space Navigation*. Butterworths mathematical texts. Butterworths, 1963.

- 
- [53] Paul M. Lion and Morris Handelsman. Primer vector on fixed-time impulsive trajectories. *Aiaa Journal*, 6(1), 1968.
- [54] J.T. Betts. *Practical Methods for Optimal Control and Estimation Using Nonlinear Programming: Second Edition*. Advances in Design and Control. Society for Industrial and Applied Mathematics, 2010.
- [55] J.T. Betts. Survey of numerical methods for trajectory optimization. *Journal of guidance, control, and dynamics*, 21(2):193–207, 1998.
- [56] Anil Rao. A survey of numerical methods for optimal control. *Advances in the Astronautical Sciences*, 135, 2010.
- [57] Marco Grammatico. Fuel-optimal lander trajectory for lunar soft-precision landing. Master’s thesis, Politecnico di Torino, 2021.
- [58] Lorenzo Casalino, Guido Colasurdo, and Dario Pastrone. Indirect approach for minimum-fuel aeroassisted transfers. In *Astrodynamics Conference*, 1996.
- [59] Guido Colasurdo. Optimal finite-thrust spacecraft trajectories. In *Astrodynamics Conference*, 1992.
- [60] Guido Colasurdo and Dario Pastrone. Indirect optimization method for impulsive transfers. In *Astrodynamics Conference*, page 3762, 1994.
- [61] Lorenzo Casalino, Guido Colasurdo, and Dario Pastrone. Optimization of delta v earth-gravity-assist trajectories. *Journal of Guidance, Control, and Dynamics*, 21(6), 1998.
- [62] Yang Wang and Francesco Topputo. Indirect optimization of fuel-optimal many-revolution low-thrust transfers with eclipses. *IEEE Transactions on Aerospace and Electronic Systems*, 59(1):39–51, 2022.
- [63] Donald E. Kirk. *Optimal control theory: an introduction*. Courier Corporation, 2004.
- [64] Daniel Liberzon. *Calculus of variations and optimal control theory: a concise introduction*. Princeton university press, 2011.
- [65] Lsoda - scipy v1.10.1 manual. <https://docs.scipy.org/doc/scipy/reference/generated/scipy.integrate.LSODA.html>.
- [66] Lawrence F. Shampine. Computer solution of ordinary differential equations. *The initial value problem*, 1975.
- [67] Chen Zhang, Francesco Topputo, Franco Bernelli-Zazzera, and Yu-Shan Zhao. Low-thrust minimum-fuel optimization in the circular restricted three-body problem. *Journal of Guidance, Control, and Dynamics*, 38(8):1501–1510, 2015.

- [68] Kenta Oshima, Stefano Campagnola, and Tomohiro Yanao. Global search for low-thrust transfers to the moon in the planar circular restricted three-body problem. *Celestial Mechanics and Dynamical Astronomy*, 128:303–322, 2017.
- [69] Aerojet Rocketdyne. Advanced electric propulsion system (aeps), 2023.

## Appendix A

### Jacobian Matrix in the CR3BP

$$\tilde{A} = \begin{bmatrix} 0 & 0 & 0 & 1 & 0 & 0 \\ 0 & 0 & 0 & 0 & 1 & 0 \\ 0 & 0 & 0 & 0 & 0 & 1 \\ \mathcal{U}_{\xi\xi} & \mathcal{U}_{\xi\eta} & \mathcal{U}_{\xi\zeta} & 0 & 2 & 0 \\ \mathcal{U}_{\eta\xi} & \mathcal{U}_{\eta\eta} & \mathcal{U}_{\eta\zeta} & -2 & 0 & 0 \\ \mathcal{U}_{\zeta\xi} & \mathcal{U}_{\zeta\eta} & \mathcal{U}_{\zeta\zeta} & 0 & 0 & 0 \end{bmatrix} \quad (\text{A.1})$$

$$\begin{aligned} \frac{\partial \mathcal{U}}{\partial \xi} &= \frac{\partial}{\partial \xi} \left\{ \frac{1}{2}(\xi^2 + \eta^2) + \frac{1-\mu}{\left[ (\xi + \mu)^2 + \eta^2 + \zeta^2 \right]^{\frac{1}{2}}} + \frac{\mu}{\left[ (\xi - 1 + \mu)^2 + \eta^2 + \zeta^2 \right]^{\frac{1}{2}}} \right\} \\ &= \xi - \frac{(1-\mu)(\xi + \mu)}{\left[ (\xi + \mu)^2 + \eta^2 + \zeta^2 \right]^{\frac{3}{2}}} - \frac{\mu(\xi - 1 + \mu)}{\left[ (\xi - 1 + \mu)^2 + \eta^2 + \zeta^2 \right]^{\frac{3}{2}}} \\ &= \xi - (1-\mu) \frac{(\xi + \mu)}{\rho_{13}^3} - \mu \frac{(\xi - 1 + \mu)}{\rho_{23}^3} \\ \frac{\partial \mathcal{U}}{\partial \eta} &= \eta - (1-\mu) \frac{\eta}{\rho_{13}^3} - \mu \frac{\eta}{\rho_{23}^3} \\ \frac{\partial \mathcal{U}}{\partial \zeta} &= -(1-\mu) \frac{\zeta}{\rho_{13}^3} - \mu \frac{\zeta}{\rho_{23}^3} \end{aligned} \quad (\text{A.2})$$

$$\mathcal{W}_{\xi\xi} = 1 - \frac{(1-\mu)}{\rho_{13}^5} [\rho_{13}^2 - 3(\xi + \mu)^2] - \frac{\mu}{\rho_{23}^5} [\rho_{23}^2 - 3(\xi - 1 + \mu)^2] \quad (\text{A.3a})$$

$$\mathcal{W}_{\xi\eta} = 3\eta \left[ \frac{(1-\mu)}{\rho_{13}^5} (\xi + \mu) + \frac{\mu}{\rho_{23}^5} (\xi - 1 + \mu) \right] \quad (\text{A.3b})$$

$$\mathcal{W}_{\xi\zeta} = 3\zeta \left[ \frac{(1-\mu)}{\rho_{13}^5} (\xi + \mu) + \frac{\mu}{\rho_{23}^5} (\xi - 1 + \mu) \right] \quad (\text{A.3c})$$

$$\mathcal{W}_{\eta\xi} = \mathcal{W}_{\xi\eta} \quad (\text{A.3d})$$

$$\mathcal{W}_{\eta\eta} = 1 - \frac{(1-\mu)}{\rho_{13}^5} (\rho_{13}^2 - 3\eta^2) - \frac{\mu}{\rho_{23}^5} (\rho_{23}^2 - 3\eta^2) \quad (\text{A.3e})$$

$$\mathcal{W}_{\eta\zeta} = 3\eta\zeta \left[ \frac{(1-\mu)}{\rho_{13}^5} + \frac{\mu}{\rho_{23}^5} \right] \quad (\text{A.3f})$$

$$\mathcal{W}_{\zeta\xi} = \mathcal{W}_{\xi\zeta} \quad (\text{A.3g})$$

$$\mathcal{W}_{\zeta\eta} = \mathcal{W}_{\eta\zeta} \quad (\text{A.3h})$$

$$\mathcal{W}_{\zeta\zeta} = -\frac{(1-\mu)}{\rho_{13}^5} (\rho_{13}^2 - 3\zeta^2) - \frac{\mu}{\rho_{23}^5} (\rho_{23}^2 - 3\zeta^2) \quad (\text{A.3i})$$

## Appendix B

### Euler-Lagrange Equations

$$\dot{\lambda} = -\frac{\partial \mathcal{H}}{\partial x} \quad (\text{B.1})$$

$$\begin{aligned} \dot{\lambda}_\xi = & -\lambda_\xi \left[ 1 - \frac{1-\mu}{\rho_{13}^3} + \frac{3(1-\mu)(\xi+\mu)^2}{\rho_{13}^5} - \frac{\mu}{\rho_{23}^3} + \frac{3\mu(\xi-1+\mu)^2}{\rho_{23}^5} \right] + \\ & -\lambda_\eta \left[ \frac{3(1-\mu)(\xi+\mu)\eta}{\rho_{13}^5} + \frac{3\mu(\xi-1+\mu)\eta}{\rho_{23}^5} \right] + \\ & -\lambda_\zeta \left[ \frac{3(1-\mu)(\xi+\mu)\zeta}{\rho_{13}^5} + \frac{3\mu(\xi-1+\mu)\zeta}{\rho_{23}^5} \right] \end{aligned} \quad (\text{B.2a})$$

$$\begin{aligned} \dot{\lambda}_\eta = & -\lambda_\xi \left[ \frac{3(1-\mu)(\xi+\mu)\eta}{\rho_{13}^5} + \frac{3\mu(\xi-1+\mu)\eta}{\rho_{23}^5} \right] + \\ & -\lambda_\eta \left[ 1 - \frac{1-\mu}{\rho_{13}^3} + \frac{3(1-\mu)\eta^2}{\rho_{13}^5} - \frac{\mu}{\rho_{23}^3} + \frac{3\mu\eta^2}{\rho_{23}^5} \right] + \\ & -\lambda_\zeta \left[ \frac{3(1-\mu)\eta\zeta}{\rho_{13}^5} + \frac{3\mu\eta\zeta}{\rho_{23}^5} \right] \end{aligned} \quad (\text{B.2b})$$

$$\begin{aligned}
 \dot{\lambda}_\zeta = & -\lambda_\xi \left[ \frac{3(1-\mu)(\xi+\mu)\zeta}{\rho_{13}^5} + \frac{3\mu(\xi-1+\mu)\zeta}{\rho_{23}^5} \right] + \\
 & -\lambda_\eta \left[ \frac{3(1-\mu)\eta\zeta}{\rho_{13}^5} + \frac{3\mu\eta\zeta}{\rho_{23}^5} \right] + \\
 & -\lambda_\zeta \left[ -\frac{1-\mu}{\rho_{13}^3} + \frac{3(1-\mu)\zeta^2}{\rho_{13}^5} - \frac{\mu}{\rho_{23}^3} + \frac{3\mu\zeta^2}{\rho_{23}^5} \right]
 \end{aligned} \tag{B.2c}$$

$$\dot{\lambda}_\xi = -\lambda_\xi - 2\lambda_\eta \tag{B.2d}$$

$$\dot{\lambda}_\eta = -\lambda_\eta + 2\lambda_\xi \tag{B.2e}$$

$$\dot{\lambda}_\zeta = -\lambda_\zeta \tag{B.2f}$$

$$\dot{\lambda}_m = \frac{T}{m^2} \lambda_\nu \tag{B.2g}$$